Ministero dell'Università e
della Ricerca

Dipartimento di Scienze
Fisiche ed Astronomiche

Università degli Studi
di Palermo

DIPARTIMENTO DI SCIENZE FISICHE ED ASTRONOMICHE

DOTTORATO DI RICERCA IN FISICA - XIX CICLO

OPTICAL AND X-RAY EMISSION FROM PROTOSTELLAR JETS: MODEL PREDICTIONS AND COMPARISON WITH OBSERVATIONS

S.S.D FIS/05

ROSARIA BONITO

Palermo, febbraio 2008

Supervisore: prof. Giovanni Peres

Coordinatore: prof. Natale Robba

Abstract

In this thesis I report on the investigation of the physical mechanisms leading to the X-ray and optical emission detected from protostellar jets. To this end, I follow both an experimental and a theoretical approach.

The theoretical analysis is accomplished by performing a detailed modeling of the interaction between a supersonic jet originating from a young stellar object and the ambient medium. I performed an extensive exploration of the parameter space for the main parameters influencing the jet/ambient medium interaction, i.e. for various values of density contrast, ν, between the ambient density and the jet, and of jet Mach number, $\mathcal{M}$. Aims include: 1) to constrain the jet/ambient medium interaction regimes leading to the X-ray emission observed in Herbig-Haro objects in terms of the emission by a shock forming at the interaction front between a continuous supersonic jet and the surrounding medium; 2) to derive detailed predictions to be compared with optical and X-ray observations of protostellar jets; 3) to get insight into the jet's physical conditions. I performed a set of two-dimensional hydrodynamic numerical simulations, assuming axial symmetry, modeling supersonic jets ramming into an uniform ambient medium. The model takes into account the most relevant physical effects, namely thermal conduction and radiative losses. My model explains the observed X-ray emission from protostellar jets in a natural way. In particular, I find that a protostellar jet that is less dense than the ambient medium well reproduces the observations of the nearest Herbig-Haro object, HH 154, and allows us to make detailed predictions of a possible X-ray source proper motion ($v_{\rm sh} \approx 500$ km s^{-1}) detectable with *Chandra*. Furthermore, our results suggest that the simulated protostellar jets which best reproduce the X-rays observations cannot drive molecular outflows. These results are presented in Bonito et al. (2004, 2007).

As for the analysis of the observations, I study both the X-ray emission detected at the basis of the nearest jet (HH 154) and the optical emission from the knots within the jet itself.

The mechanism responsible for the X-ray emission is still not clear. Self-shocking in jets, shocks where the jet hits the surrounding medium, reflected or scattered stellar X-ray emission have all been invoked as possible explanations. One key diagnostic discriminating among physical emission mechanisms is the

motion of the X-ray source: hydrodynamical numerical models of continuous protostellar jets plowing through a uniform medium show an X-ray emitting shock front moving at several hundreds km/s. In the nearest X-ray emitting protostellar jet, HH 154, this is detectable, with the spatial resolution of the Chandra X-ray observatory, over a few years baseline, allowing a robust discrimination among different mechanisms. We have performed, in October 2005, a deep Chandra X-ray observation of HH 154. Comparison with the previous (2001) Chandra observation allows to detect proper motion down to the level predicted by models of X-ray emitting shocks in the jet. The 2005 Chandra observation of HH 154 shows unexpected morphological changes of the X-ray emission in comparison with the 2001 data. Two components are present: a stronger, point-like component with no detectable motion and a weaker component which has expanded in size by approximately 300 AU over the 4 years time base of the two observations. This expansion corresponds to approximately 500 km/s, very close to the velocity of the X-ray emitting shock in the simple theoretical models. The 2005 data show a more complex system than initially thought (and modeled), with multiple components with different properties. The observed morphology is possibly indicating a pulsed jet propagating through a non-homogeneous medium, likely with medium density decreasing with distance from the driving source. Detailed theoretical modeling and deeper X-ray observations will be needed to understand the physics of this fascinating class of sources. The main results concerning the analysis of the X-ray emission from the HH 154 protostellar jet are discussed in Favata, Bonito et al. (2006).

The primary aim of the optical observation of the HH 154 protostellar jet, performed with the Hubble Space Telescope, is to study the time evolution of the jet, by measuring the proper motions of knots and features, observed within the jet itself, as they progress outwards from the originating source. The data are then related to other data covering the spectrum from the optical to X-rays in order to understand the energetics of low mass star jets in general and this jet in particular.

The nebulosities associated with the jet(s) originating at the protostellar binary L1551 IRS5 have been imaged in a number of spectral bands using the Hubble Space Telescope. This allows the proper motions to be measured, and to make a simple characterization of the physical conditions in different features. To this end we developed a reproducible method of data analysis by which it is possible to define the position and shape of each substructure observed within the protostellar jet. Using this definition, we derive the proper motion of the knots in the jet as well as their flux variability and shock emission. The time base over which HST observations have been carried out is now over 10 years. The sub-structures within the jet undergo significant morphological variations and collision between different knots, ejected at different epochs and maybe with

different speed, can occur. From the analysis of the terminal and internal working surfaces within the jet, we derive that the more likely scenario for the HH 154 jet is that of a jet traveling through a denser ambient medium (a "light jet"). The velocities along the jet vary between $\sim$ 100 km/s and over 400 km/s, with the highest speed corresponding to the knots at the basis of the jet. There are indications that the HH 154 jet have been active relatively recently. In particular there is strong evidence that the knots at the basis of the northern jet corresponds to the location where the highest velocity and the highest excitation component along the jet are measured. More important, this is the location where the X-ray source has been discovered. The results derived from the optical analysis of the HH 154 jet are discussed in Bonito et al. (2008).

Contents

Chapter 1

Introduction

1.1 Young Stellar Objects and protostellar jets

Young Stellar Objects (YSOs) are very complex systems, formed by many components which play important roles and interact with each other: the very active coronae of the protostar, the protostellar magnetic field, high speed plasma flows, the disk, as well as the circumstellar inhomogeneous medium. The early stages of the star birth are characterized by a variety of mass ejection phenomena, including collimated jets. These plasma jets can travel through the interstellar medium at supersonic speed, with shock fronts forming at the interaction front between the jet and the unperturbed ambient medium.

Protostellar jets (Fig. 1.1) appear to be associated with all evolutionary stages leading to star formation, whenever accretion on the star is a process that is still at work, from deeply embedded protostellar objects to visible young stars.

Fig. 1.2 shows the classification of the various phases of the YSOs: class 0 and class I refer to still deeply embedded sources when the accretion is due to the gravitational collapse of the environment on the central star; young stars where a circumstellar disk accretes material on the central star are called class II stars, also known as Classical T Tauri stars (CTTs); class III consists of those sources where no evidence of the presence of a disk nor of any kind of accreting process are present.

The relation between the accretion from a circumstellar disk on the star and the opposite phenomenon of the mass ejection from YSOs, although being a strong experimental evidence, has not yet been explained in details. Mass ejection from protostars are observed only in class 0, I and II YSOs. In class III YSOs, the so-called Weak Line T Tauri (WLTT) stars, in which the circumstellar accretion disk has disappeared, there is no evidence of the presence of jets.

Jets are a very common feature in astrophysical contexts, being found on spatial and energy scales spanning many orders of magnitudes. While the large

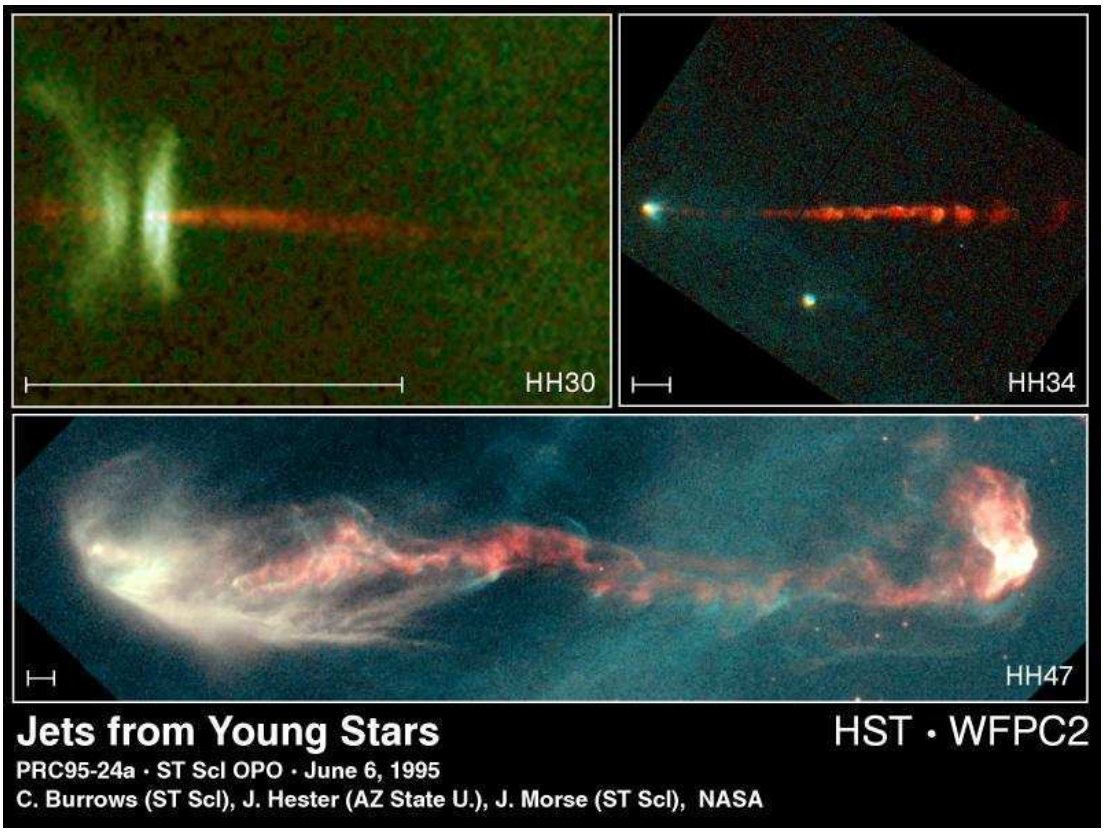

Figure 1.1: HST images of three protostellar jet: HH 30, HH 34, HH 47. The scale in the bottom left corner of each picture represents 1000 AU. All images were taken with the Wide Field Planetary Camera 2 in visible light. The HH designation stands for "Herbig-Haro" object, the name for bright patches of nebulosity which appear to be moving away from associated protostars.

jets in active galaxies are detected in the radio band on scales of megaparsec, a very similar process can be observed on much smaller spatial scales (of hundreds of AU[1]) in jets originating in YSOs. Even if the scales and many other features are very different, the basic characteristics of the processes are very likely to be the same, with the jet originating from the environment of an accretion disk, with magnetic fields playing an essential role in both cases. Nearby protostellar jets offer a unique opportunity to understand physical processes leading to the jet's acceleration and collimation as they can be studied down to spatial scales of tens of AUs, observing the processes very close to the acceleration site. Their study has been a fruitful field of research, and they are among the favorite Hubble Space Telescope (HST) targets.

[1] 1 AU = 1.5×10^{13} cm.

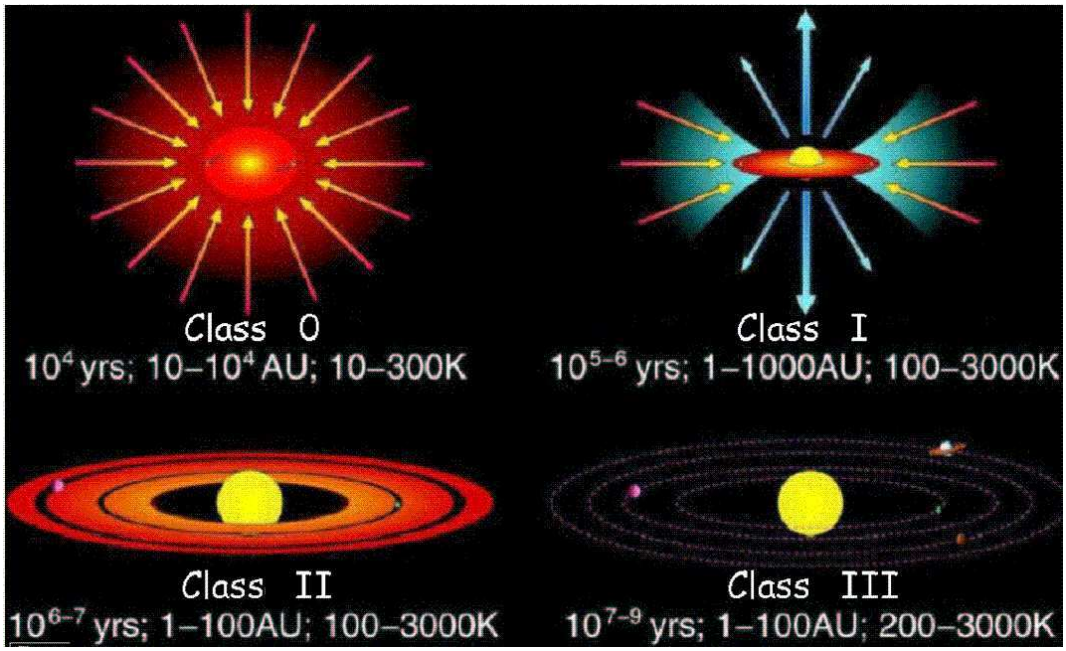

Figure 1.2: Young Stellar Objects classification. The Class 0 and Class I YSO are characterized by a deeply embedded objects accreted from an almost spherical envelope surrounding the young protostellar object. The Class II, also known as Classical T Tauri (CTT) stars refers to young stars accreted by a circumstellar disk. The so-called Weak-line T Tauri (WLTT) stars, corresponding to Class III, show no evidence of accretion onto the star any longer.

1.2 Herbig-Haro (HH) objects

Herbig-Haro (HH) objects are nebulae observed in optical band showing a characteristic emission line spectrum (mainly H_α and [SII] emission) and found in star-forming regions. These objects are now recognized as associated to the outflow activity from YSOs. In fact protostellar jets ejected by YSOs travel supersonically through the ambient medium leading to the formation of a knotty structure due to shocks at the interaction front between the jet and the ambient medium, identified with the HH objects.

Detailed studies of these objects in the radio, infrared and optical bands have been carried in the last 50 years, i.e. since HH objects were discovered (Herbig 1950; Haro 1952; see also Reipurth & Bally 2001).

Fig. 1.3 shows, as an example, a protostellar jet characterized by a chain of several knots well visible within the jet itself.

The physics of the shocks forming within the jet are well described by Landau & Lifshitz (1959). In a reference frame where the infinitesimal width discontinuity defining the shock front is at rest, the conservation equation of mass, momentum and energy, known as Rankine−Hugoniot equations, are

$$[\rho v_x] = 0 \tag{1.1}$$

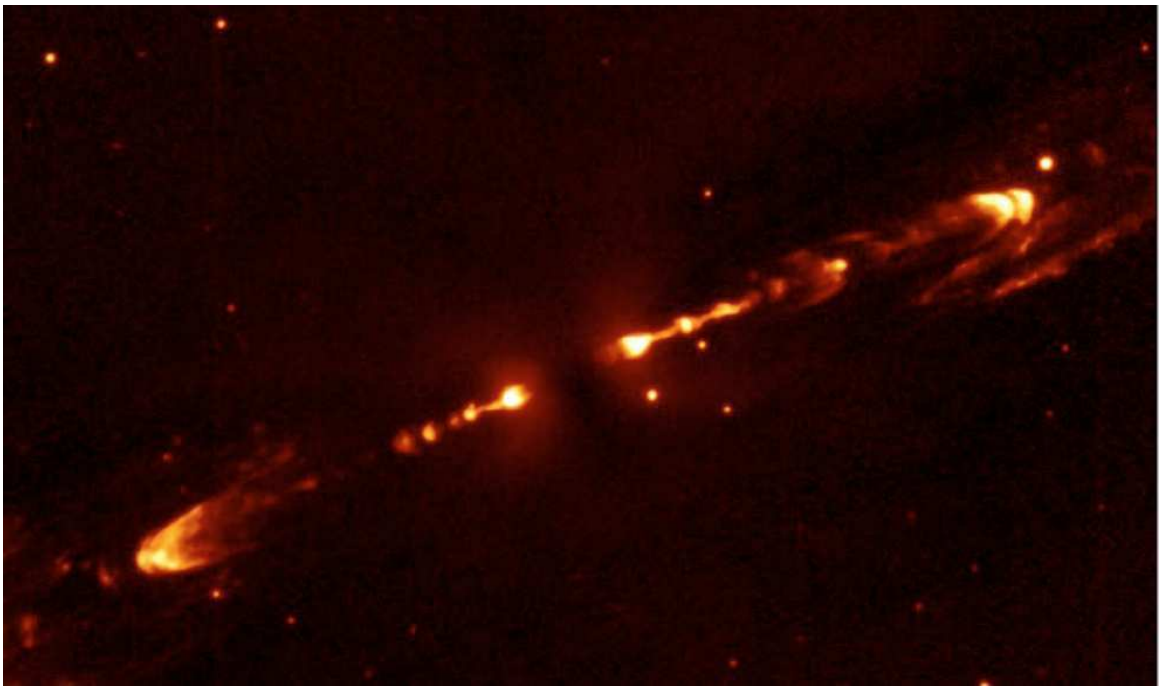

Figure 1.3: HH 212 as observed with the Very Large Telescope (McCaughrean et al. 2002). The knotty morphology is well visible within the object.

$$[P + \rho v_x^2] = [\rho v_x v_y] = [\rho v_x v_z] = 0 \tag{1.2}$$

$$[\rho v_x (1/2 v^2 + h)] = 0 \tag{1.3}$$

where v_x, v_y and v_z are the components of the bulk velocity of the gas, v, ρ and P are its density and pressure, and h is the enthalpy per unit volume, while the square brackets indicate the differences between the pre-shock and post-shock values.

The ratio between the flow speed and the sound speed defines the Mach number, $\mathcal{M} = v/c_\mathrm{a}$, which quantifies the intensity of the shock. In the case of a strong adiabatic shock, corresponding to $\mathcal{M} >> 1$, in a perfect gas, it is possible to derive the relations between the pre-shock and post-shock quantities in the form

$$\frac{\rho_1}{\rho_0} = \frac{\gamma + 1}{\gamma - 1} \tag{1.4}$$

$$\frac{P_1}{P_0} = \frac{2\gamma \mathcal{M}^2}{(\gamma + 1) - \frac{\gamma - 1}{\gamma + 1}} \tag{1.5}$$

$$\frac{T_1}{T_0} = \frac{(\gamma - 1) P_1}{(\gamma + 1) P_0} \tag{1.6}$$

where T is the temperature, $\gamma = C_P/C_V$ is the specific heats ratio, and 1 and 0 indicate the post- and pre-shock values, respectively. In the case of a monoatomic gas ($\gamma = 5/3$) the strong shock case leads to a limit for the density ratio corresponding to $\rho_1/\rho_0 = 4$. On the other hand, the temperature and pressure discontinuities in a strong shock can increase arbitrarily, as the factor $\mathcal{M}^2$ increases.

1.2.1 The working surface

The complex region where the jet-ambient interaction takes place is called Working Surface (WS). The WS can be either terminal or internal (IWS). The terminal WS is formed when the jet rams on the initially unperturbed ambient medium, the IWS, otherwise, is probably due to the auto-interaction of flows ejected recurrently in different epochs from the protostar (pulsed jets, Raga et al. 1990). In both cases (terminal or internal), the WS consists of two shocks and the region of space between these two surfaces (Hartigan 1989). The two shocks consists of a leading shock, called bow-shock for its characteristic curved shape, which accelerates the ambient material, and a reverse shock (Mach disk), which decelerates the supersonic flow. Fig. 1.4 shows the structure of a WS in protostellar jets.

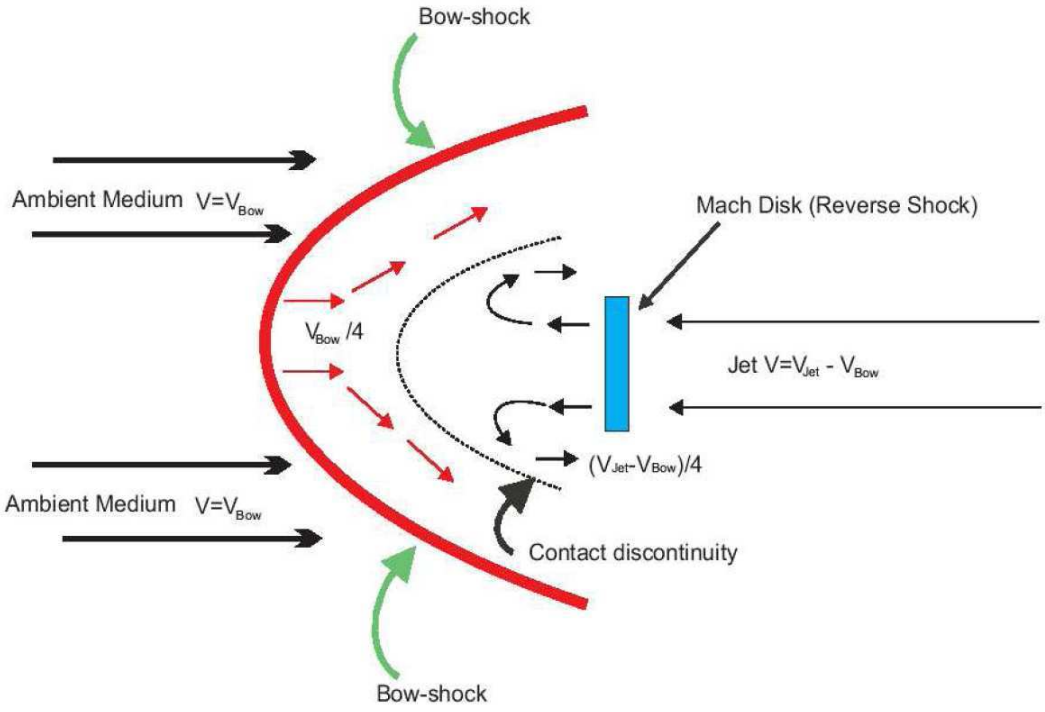

Figure 1.4: A schematic illustration of the working surface in a protostellar jet. The two main shocks are indicated in the figure as the bow shock (red), i. e. the leading shock, and the Mach disk (blue), i. e. the reverse shock. The velocities are in the frame of reference where the shock front is at rest. (E. Whelan)

1.2.2 Proper motion of the HH objects

Typical values of the protostellar jets velocity are of several hundreds of km/s. This speed is lower and lower at greater distances from the protostar from which the jet originates. The proper motion (i. e. the component of the velocity in the plane of the sky) of the HH objects can be derived by comparing images of the same object taken in different epochs. However measuring proper motion of the HH objects requires high resolution images. As an example, the nearest HH objects (at a distance of about 140 pc from the Earth)[2] move at $\sim$ 100 km/s and show angular displacements of the order of a fraction of an arcsecond in few years. Due to the low resolution achievable with ground-based observations, it is necessary a too long time-baseline between consecutive observations in order to measure displacements of the HH objects with speed of several hundreds of km/s. Furthermore these time scales are comparable to the post-shock cooling time of the flux, thus leading to substantial evolution of the jet, for instance the formation of new knots within the jet or even to the fading of some structures.

1.3 Optical emission from protostellar jets

The HH objects described in Sect. 1.2 are the main sources of the optical emission observed from protostellar jets. In more details, the emission spectrum in the optical band appears to be associated with the cooling post-shock region. The region heated by the moving shock, cools down due to the radiative losses. The radiative shocks consist of a thin filament corresponding to the shock front and of a more extended cooling region behind the shock front. Most of the emission observed as HH objects originates from the latter. This zone emits mainly forbidden lines of metals ([SII], [OIII], and so on), while a Balmer filament corresponds to the position of the shock front. Fig. 1.5 schematically shows how emission of different species dominates at different distances from the shock front.

A very powerful diagnostics of HH objects, based on narrow band filters images, is the morphology of the H_α emission and its spatial distance with respect to forbidden lines, as [SII] emission. Chevalier & Raymond (1978) show that H_α emission (Balmer filaments) can be observed where the shock front forms, due to the incident neutral Hydrogen which is collisionally excited before being totally ionized. This process is valid for forbidden lines too, but, due to the very low abundances of metals with respect to Hydrogen, the emission due to forbidden lines in the shock front site is not observable. Since forbidden lines (like [SII]), are detectable in the post-shock region (where the shocked material cools down), comparing the positions of the H_α and [SII] emission it is possible to discriminate between the shock front and the cooling zone. Fig. 1.6 shows, as an example,

[2] 1 pc $\approx 3.09 \times 10^{18}$ cm

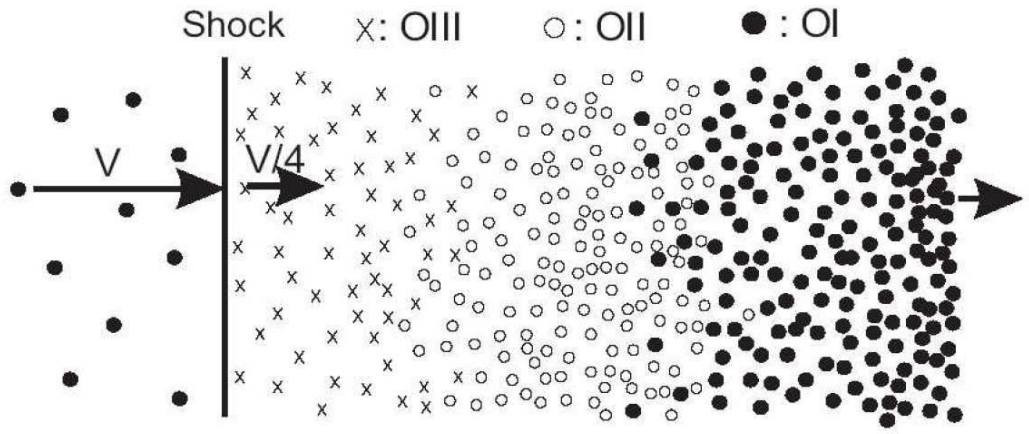

Figure 1.5: Stratification of the emission of the cooling zone behind the shock front (Hartigan et al. 2000). The velocities are relative to the shock front. As the distance from the shock front increases, the emission from ion corresponding to lower and lower temperatures is detected.

the stratification of the H_α and [SII] emission in the working surface of the HH 47 object. It is clear that the H_α emission (white in the difference image, panel d) originates mainly from the two main shocks, bow shock and Mach disk, and that the [SII] emission (black in the difference image, panel d) marks the cooling zone between the two shocks.

One of the main parameters describing the jet-ambient system is the ambient-to-jet density contrast, $\nu = n_a/n_j$, where n_a and n_j are the ambient and jet density, respectively. Following Hartigan (1989), it is possible to derive the value of ν by simply analyzing the emission associated to the forward and reverse shock in HH objects. In this way, it is possible to answer one of the most debated question concerning the existence of "light jets", i. e. jets which propagate through denser surrounding media. Hartigan (1989) derives a relation between the ratio of the Mach disk and the bow shock luminosity as a function of the ambient-to-jet density contrast, ν. In more details, if the H_α emission at the bow shock is greater than that originating from the Mach disk, the jet is over-dense with respect to the ambient medium. If, otherwise, the Mach disk is brighter that the bow shock, then the jet is less dense than the surrounding medium, i. e. the "light jet" case. Fig. 1.7 shows that the light jet scenario is invoked when the Mach disk emission is expected to be dominant with respect to the bow shock emission.

1.4 X-ray emission from protostellar jets

Pravdo et al. (2001) predicted that the most energetic HH objects could be significant sources of X-ray emission. Following Zel'Dovich & Raizer (1967), one can derive useful relations between the physical parameters of interest in the

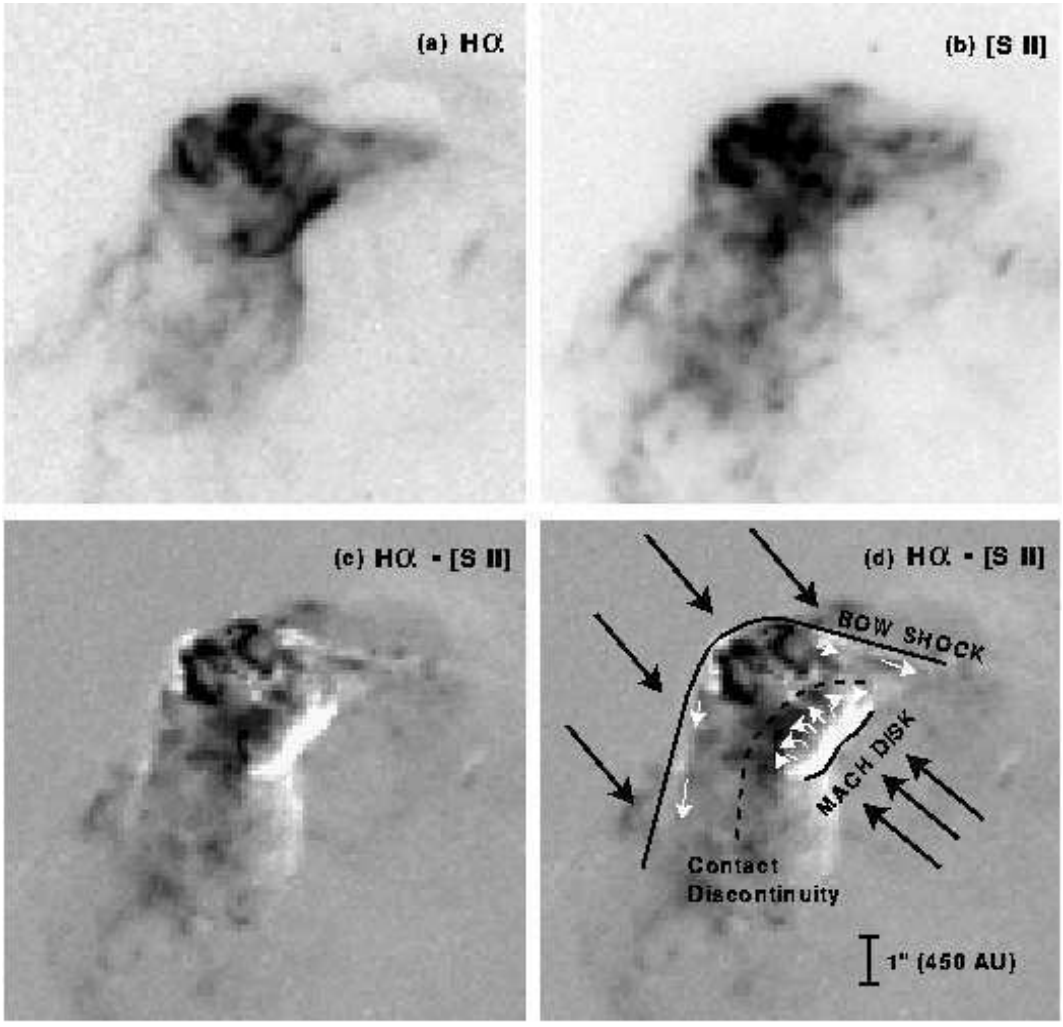

Figure 1.6: An enlargement of the HH 47A working surface: (a) H_α; (b) [S II]; (c) $H_\alpha -$ [S II]; and (d) a sketch showing the postulated positions of the bow shock and the Mach disk and the velocity of the gas as seen in the rest frame of the working surface (Hartigan et al. 1999).

post-shock region (such as the plasma temperature and the shock velocity), viz.,

$$T_{\rm psh} = \frac{\gamma - 1}{(\gamma + 1)^2} \left(\frac{m v_{\rm sh}^2}{k_{\rm B}} \right) , \tag{1.7}$$

where $T_{\rm psh}$ is the post-shock temperature, γ is the ratio of specific heats, $v_{\rm sh}$ is the shock front speed, m is the mean particle mass and $k_{\rm B}$ is the Boltzmann constant. Assuming that the typical velocity, $v_{\rm sh} \approx 500$ km s^{-1} (i. e. the proper motion of HH 154, see Fridlund et al. 2005) is referred to the reference frame of the pre-shock medium, the expected post-shock temperature is a few million degrees, thus leading to X-ray emission.

Recently, X-ray emission from HH objects has been detected with both the XMM-*Newton* and *Chandra* satellites: the low mass YSO HH 2 in Orion (Pravdo et al. 2001) and HH 154 in Taurus (Favata et al. 2002; Bally et al. 2003), the

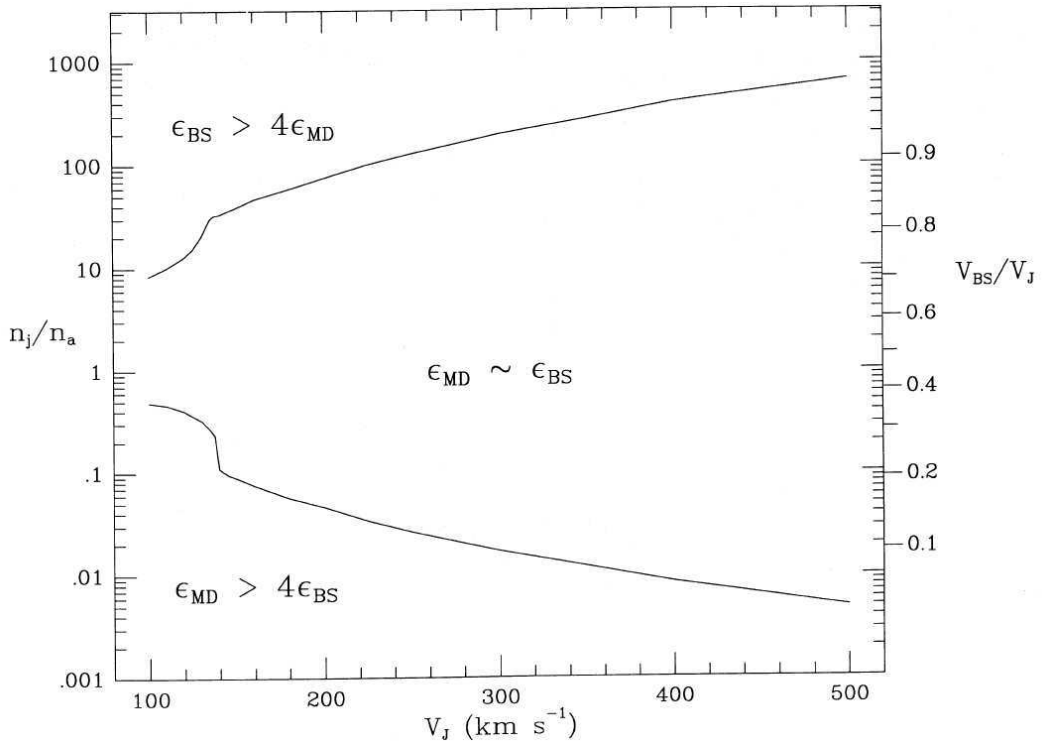

Figure 1.7: Parameters space where the bow shock and the Mach disk are expected to dominate the emission from the working surface of a protostellar jet (Hartigan 1989). The Mach disk emission dominates over the bow shock emission when the jet is less dense than the ambient medium, the scenario of a "light jet".

high mass YSO objects HH 80/81 in Sagittarius (Pravdo et al. 2004) and HH 168 in Cepheus A (Pravdo & Tsuboi 2005), and HH 210 in Orion (Grosso et al. 2006). Indications of X-ray emission from protostellar jets are also discussed by Tsujimoto et al. (2004) and Güdel et al. (2005). A summary of the relevant physical quantities derived for these objects is presented in Table 1.1 (Bonito et al. 2007).

In addition to the interest in the physics of protostellar jets, understanding the X-ray emission from protostellar jets is important in the context of the physics of star and planet formation. X-rays (and ionizing radiation in general) may affect the environment of young stellar objects and, in particular, the physics and chemistry of the accretion disk and its planet-forming environment. The ionization state of the accretion disk around young stellar objects will determine its coupling to the ambient and protostellar magnetic field, and thus, for example, influence its turbulent transport. In turn, this will affect the accretion rate and the formation of structures in the disk and, therefore, the formation of planets. X-rays can also act as catalysts of chemical reactions in the disk's ice and dust grains, thereby significantly affecting its chemistry and mineralogy.

Table 1.1: Relevant physical parameters observed in confirmed X-ray emitting HH objects. $L_{\rm X}$ is the reported X-ray luminosity, kT and $N_{\rm H}$ are respectively the best fit parameters derived from spectral analysis for the temperature (in keV) and for the interstellar absorption column density, v is the proper motion derived from optical observations, D is the distance of the object observed and $L_{\rm bol}$ is the bolometric luminosity of the jet driving source (Pravdo et al. 2001; Favata et al. 2002; Bally et al. 2003; Pravdo et al. 2004; Pravdo & Tsuboi 2005; Grosso et al. 2006). $L_\odot$ is the solar bolometric luminosity. (Bonito et al. 2007)

object	$L_{\rm X}$ $[10^{29}$ erg s$^{-1}]$	kT [keV]	$N_{\rm H}$ $[10^{22}$ cm$^{-2}]$	v [km s^{-1}]	D [pc]	$L_{\rm bol}/L_\odot$	$L_{\rm X}/L_{\rm bol}$
HH 2	5.2	0.23	≤ 0.09	230	480	81^a	1.7×10^{-6}
HH 154	3.0	0.34	1.40	500	140	40^b	9.7×10^{-7}
HH 80/81	450	0.13	0.44	700	1700	2×10^{4c}	1.5×10^{-4}
HH 168	1.1	0.5	0.40	500	730	2.5×10^{4c}	3.6×10^{-7}
HH 210	10	$0.07 - 0.33$	0.80	130	450	–	–

[a] Chini et al. (2001)

[b] Liseau et al. (2005)

[c] Curiel et al. (2006)

While all young stellar objects are strong X-ray sources, they will irradiate the disk from its center, so that stellar X-rays will illuminate the inner part of the disk and the disk itself in grazing incidence, concentrating their effects in the central regions of the disk; it is worth noting that this irradiation process depends critically on the disk geometry, so that, for example, in flared disks more extended regions can be affected by ionizing radiation. Since protostellar jets are located above the disk, they will illuminate the disk in near normal incidence, maximizing their irradiation effects even in the outer disk regions normally shielded from the stellar X-rays (see Fig. 1.8).

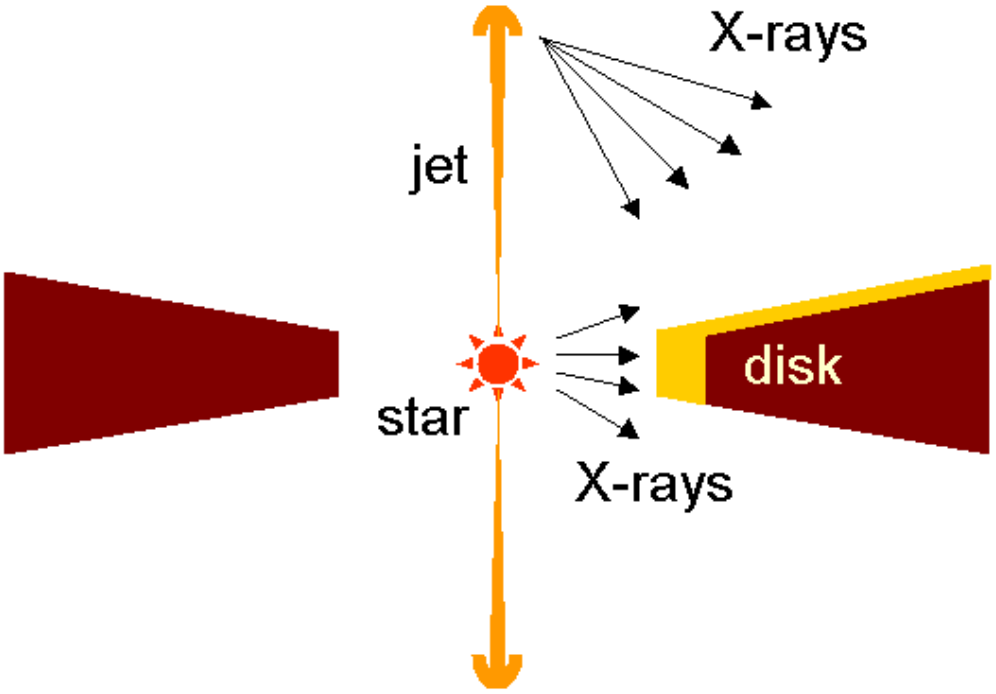

Figure 1.8: Schematic view of the system composed by the YSO, its disk, the bipolar jet and the X-ray emission. The protostar illuminates the inner portion of the disk, while the X-ray emission from the jet can irradiate even the outer disk region (Orlando & Favata 2007).

X-ray emission is now known to be an ubiquitous process in protostars, from the Class 0 phase (protostars still accreting spherically, although the evidence here is still fragmentary) to the Class I phase (where accretion disks have formed but envelopes are still present) through the Classical T Tauri phase (where only accretion disks are left around the stars).

The number of known and detected protostellar jet X-ray sources is limited (compared e.g. with the number of young stellar X-ray sources), also because their detection requires a number of favorable conditions. The X-ray luminosity

from the known jets is lower than the typical stellar X-ray luminosity of YSOs (whether Class I or classical T Tauri stars [CTTs]), so that, given the small spatial scale of the jets (few arcsec in the case of HH 154), even with the very sharp Chandra Point Spread Function (PSF, see Appendix B) their X-ray emission will in general be difficult to disentangle from that of the parent star. HH 154 offers in this respect an unique laboratory, as the parent star (IRS 5) is hidden behind a very large absorbing column density ($A_V \approx 150$ mag), from which the jet emerges with limited absorption, allowing us to study the X-ray emission (and more in general the jet itself in a range of wavelengths) very close to the acceleration site, without being blinded from stellar light. Furthermore, by being closer to Earth than most other known HH X-ray sources, the morphology and thus the physics of HH 154 can be studied to a high level of spatial detail impossible elsewhere.

The detection of X-ray emission from protostellar jets is a very recent result, since the first convincing evidence of X-rays from HH objects has been discovered just few years ago (Pravdo et al. 2001). The mechanisms leading to X-ray emission from protostellar jets are not clearly understood so far.

1.5 Models

Since most of the physical processes related to the HH jets are still unclear, several models have been developed concerning these interesting objects, since the first numerical simulations of Norman et al. (1982).

Most of these numerical models refer to the study of the launching mechanisms and the collimation of the protostellar jets traveling through the ambient medium. It is likely that the acceleration of an outflow and its collimation occur at different locations. In fact while most flows are probably launched at radii of at most a few astronomical units, there is strong evidence that the collimation observed in many protostellar jets occurs at larger distances from the source than the launch region.

Outflows can in principle originate in three kind of locations near the source: (a) as a stellar wind launched from the star itself; (b) as an "X-wind" launched from the stellar magnetosphere at a distance ranging from a few to tens of stellar radii, where it interacts with the inner edge of the accretion disk; and (c) as a magneto-centrifugal "disk wind" launched from the accretion disk at distances of 0.1 AU or more from the young star.

Magnetic fields have been invoked in order to explain the collimation observed in protostellar jets (Mellema & Frank 1997; Lery et al. 1998). Evidence for strong magnetic fields at hundreds of AU from a protostar is provided by circular polarization of the radio continuum emission from the vicinity of T-Tau (Ray et al. 1997).

The X-ray emission has been discovered in the last few years prompting to the development of numerical models which investigate the physical mechanisms which can explain the X-ray emission observed. Several models have been proposed to explain the X-ray emission from protostellar jets, but the emission mechanism is still unclear. Bally et al. (2003), in particular, suggested various models, not based on simulations, for the X-ray emission associated to HH 154: these include X-ray emission from IRS 5 reflected by a dense medium, X-ray emission produced when the stellar wind shocks against the wind from the companion star, or produced in shocks within the jet.

A simple analytic model which allows to derive the X-ray luminosity of a bow shock using the initial physical parameters of the outflow, as the dimension of the source, the speed of the shock, the pre-shock density, has been developed by Raga et al. (2002). In particular, they assume that the X-ray source is coincident with the head of the protostellar jet, with gas temperature and density of the order of the post-shock parameters on the jet axis. In the limit case of a strong shock, they derive the X-ray luminosity of the bow shock as

$$L_X = min[L_r, L_{nr}] \tag{1.8}$$

where

$$L_r = 4.1 \times 10^{-6} L_\odot \frac{n_0}{100 cm^{-3}} \left(\frac{r_b}{10^{16} cm}\right)^2 \left(\frac{v_{bs}}{100 kms^{-1}}\right)^{5.5} \tag{1.9}$$

$$L_{nr} = 4.5 \times 10^{-5} L_\odot \left(\frac{n_0}{100 cm^{-3}}\right)^2 \left(\frac{r_b}{10^{16} cm}\right)^3 \frac{v_{bs}}{100 kms^{-1}} \tag{1.10}$$

Raga et al. (2002) verified the predictions of their analytical model by performing a set of numerical simulations and by comparing the X-ray luminosity derived from their model with the observed values obtained from the HH 2 and HH 154 jets, the first protostellar jets from which X-ray emission has been discovered. The results of the model of Raga et al. (2002) are consistent with observations. However this simple model does not take into account the absorption due to the presence of the interstellar medium (ISM) and there is also the ad hoc assumption, not rigorously demonstrated, that the X-ray emission originates from the head of the jet.

1.6 Contents of the thesis

The study of the protostellar jets, in general, and of their emission, both in the optical and X-ray bands, is an interesting field of research in the more complex scenario of the star forming region paradigm. Most of the questions concerning these objects are however still unclear. The aim of my work, and the main

content of this thesis, is the investigation of the physical mechanisms leading to the observed optical and X-ray emission from protostellar jets, through a multi-wavelength analysis of the nearest X-ray emitting HH jet, HH 154, located in the star forming region L1551.

1.6.1 The star forming region L1551

The L1551 star-forming region (Fig. 1.9) is located in the Taurus molecular complex and, thus, is one of the closest (about 150 pc) to us (Kenyon et al. 1994). It demonstrates essentially all signs of low mass star formation taking place in the recent past and/or ongoing. Several molecular outflows and jets, the most remarkable being the one centered on the binary Young Stellar Object IRS5, are found as well as a number of T-Tauri stars, X-ray sources, Herbig-Haro objects, protostellar disks and embedded sources. A T association is apparently being formed, and its proximity and the orientation of several of the sources allow the study of faint and small structures. The outflow centered on IRS5 is one of the most studied and was the first identified (Snell et al. 1980). It may actually be the key to explain many important factors in the process by which low mass stars and associated planetary systems form (e.g. Fridlund et al. 1989, 2002). IRS 5 is a deeply embedded double source (Bieging & Cohen 1985; Rodriguez et al. 1986; Looney et al. 1997, Rodríguez et al. 1998), obscured by about 150 mag of visual extinction with masses of approximately $0.8M_{\odot}$ and $0.3M_{\odot}$ respectively (Liseau et al. 2005). Each of the components is surrounded by a small (about 10 AU) disk (Rodríguez et al. 1998) and the complex is enveloped in a larger (about 5000 AU) dense flattened and rotating structure (Fridlund et al. 2002). From each of the stellar components an optical jet with Herbig-Haro characteristics (HH 154) originates (Fridlund & Liseau 1998; Rodríguez et al. 2003a); the jets came from behind the ≈ 150 magnitudes of visual extinction that surrounds the binary, the first knot being at about 0.5" from the star.

Of course the proximity of HH 154 makes the associated protostellar jet probably the best laboratory to study the evolution of the complex X-ray morphology in HH objects.

HH 154

HH 154 (Fig. 1.10) is one of the nearest and best studied Herbig-Haro objects, and it is composed of several knots aligned along an optically visible jet leading away from the IRS 5 protostar.

HH 154 is an unique laboratory for the study of jet physics, as the parent star (L1551 IRS5) is hidden behind a very large absorbing column density ($A_V \approx 150$ mag), from which the jet emerges with limited absorption ($A_V \approx 7$ mag), allowing us to study the X-ray emission (and more in general the jet itself in a range of

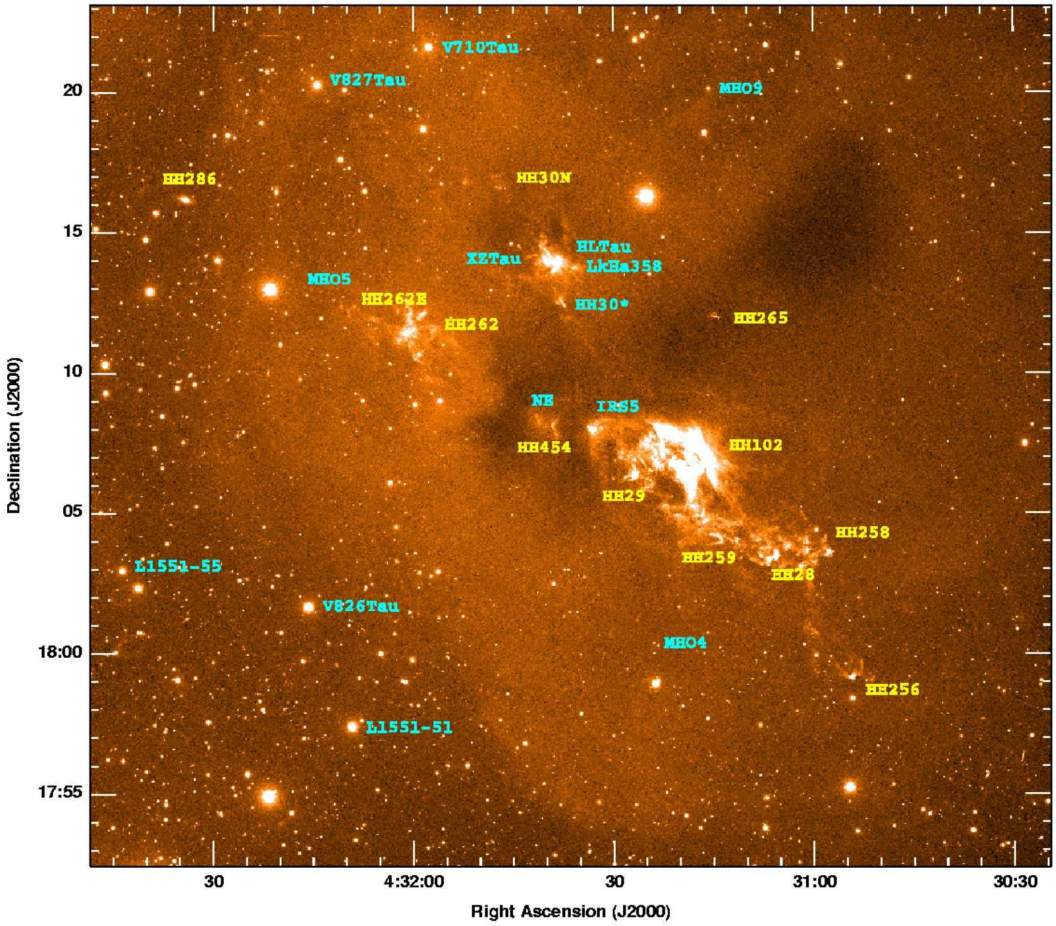

Figure 1.9: [S II] image of the L1551 cloud (Moriarty-Schieven et al. 2006). Known pre-main-sequence objects and YSOs are labeled, along with selected HH objects

wavelengths) very close to the acceleration site, without being blinded by stellar light. Furthermore, by being one of the nearest known HH X-ray sources, the morphology and thus the physics of HH 154 can be studied to a high level of spatial detail impossible in more distant objects, also allowing to detect motions on short time scales.

1.6.2 Multi-wavelength study of the HH 154 jet: observations and numerical models

Proper motion studies of several jets have recently been carried out from the ground, but are severely limited by the long time bases needed, as well as the difficulties in resolving the fine structure in the jets.

HH 154 is the known astrophysical jet located nearest to the Earth, and from our earlier ground based data it appeared very interesting to resolve smaller spatial structures using higher spatial resolution than that achieved from the ground.

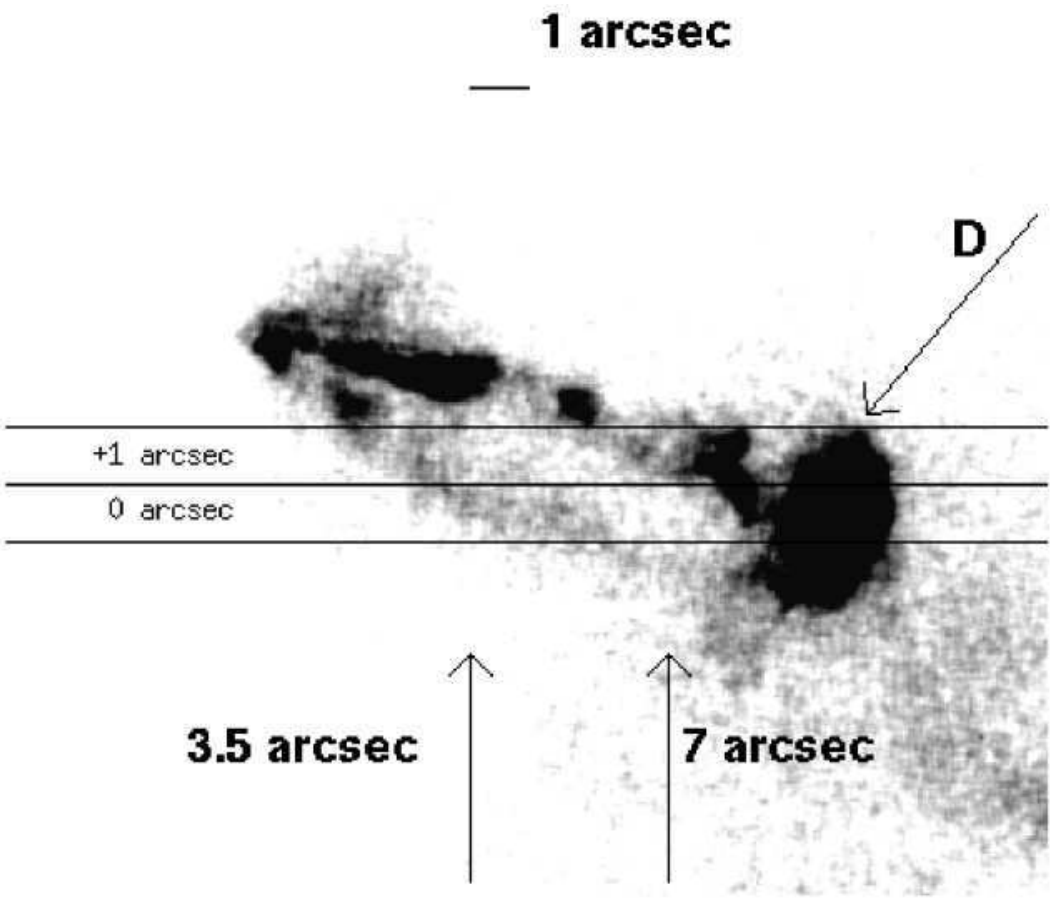

Figure 1.10: The HST R-band image of the HH 154 jet displayed at levels of contrast that show the faint structures. The brightest feature is the so-called feature D, identified as the working surface of the northern jet. The horizontal lines show the positions of the $0''$ and $1''$ slits. The vertical lines are at $3.5''$ and $7''$, respectively, from the nominal position of IRS 5. The scale is indicated by the $1''$ long horizontal bar in the upper part of the figure. North is up, and east is toward the left (Fridlund & Liseau 1998).

In this case, the NASA/ESA Hubble Space telescope (HST) can achieve similar spatial resolution as that utilized in current 2D hydrodynamical calculations of jets ($\sim 10^{14}$ cm). A multi cycle observing program with the HST consequently appeared well motivated, with the primary goal being the study of the time evolution of the jet, and utilizing the shock diagnostic emission lines of H_α and the [SII] doublet at $\lambda\lambda 6717, 6731$Å to determine its physical properties.

X-ray emission from HH objects is now considered as a possibly general feature of such objects. HH 154 is the nearest HH object from which X-ray emission has been detected and the only protostellar jet whose X-ray source's morphology has been resolved so far. The X-rays have been discovered at the same location of the first knot at the base of the jet (Bally et al. 2003) quite likely emanating from the jet itself, due to its impact on circumstellar material. The location of the X-rays coincides with position where optical spectroscopy and HST imaging

finds nebular knots with true velocity of 500 km/s. Favata et al. (2002) and Bally et al. (2003) discovered X-ray emission originating from HH 154, unambiguously excluding that the X-ray source is associated with the L1551 IRS 5 protostar both because of the position of the X-ray source, displaced by 0.5" arcsec from IRS 5 along the jet axis, and because the absorbing column density found from the X-ray spectrum (corresponding to a visual extinction $A_V \approx 7$ mag) is by far too small to be associated with IRS 5 ($A_V \approx 150$ mag). Soft X-ray emission from jets driven by protostellar sources has been discovered in 1999 thanks to the improved sensitivity and spatial resolution offered by both the XMM-Newton and Chandra observatories. HH2 in Orion has been the first source detected (Pravdo et al. 2001), with HH 154 (the jet originating from the embedded binary protostar IRS 5 in the L1551 star-forming region) following shortly thereafter (Favata et al. 2002; Bally et al. 2003). While more sources have been detected later, HH 154 remains the best source to study thanks to both its being nearby (D$\approx$ 150 pc) and to its being observable through a moderate absorbing column density. This allows to study the X-ray emission from the jet with good detail and without any glare from the parent star. X-ray emission from HH 154 was observed with XMM-Newton (Favata et al. 2002), allowing to determine the temperature of the source at about 4 MK. The limited spatial resolution of XMM-Newton did not allow to pinpoint the source of X-ray emission, and Favata et al. (2002) speculated that the source of X-ray emission might be located within the jet's working surface (i.e. the shock formed when the jet hits the circumstellar material), located in 2005 at some 15 arcsec from the parent star. The spatial resolution of Chandra allowed Bally et al. (2003) to reject this hypothesis, showing that the X-ray emission is located very close to the protostar itself and thus to the jet's base.

The comparison between new X-ray observations of HH 154 jet and the morphology of the optical knots can provide improvement on understanding the physical mechanism governing the observed emission.

Numerical results provide a tool to obtain predictions on several physical properties of X-ray emitting protostellar jets, namely proper motion of the source and the variability of the X-ray luminosity. The comparison between our model's predictions and observations, in the X-ray and in the optical wavelength, will lead to a detailed description of the mechanism causing the X-ray emission from protostellar jets.

1.7 Aims of the thesis

The main aim of this thesis is the investigation of the X-ray and optical emission from protostellar jets, both through observations, with the Chandra X-ray telescope (see Appendix B) and the optical Hubble Space Telescope (see Appendix

C), and through detailed numerical simulations performed with the FLASH code (see Appendix A). In fact a complete procedure to investigate the physical mechanisms leading to the optical and X-ray emission detected in protostellar jets is based on the physical properties observed in protostellar jets itself; using these parameters as a starting point, it is possible to develop a detailed numerical model in order to make predictions on the physical characteristics of the jets. Then these model's results can be directly compared with the experimental data so as to verify the model and to constrain the physical configuration of the protostellar jets in general. To this end, in this thesis I deal with both the observed data, following a multi-wavelength approach (optical and X-ray emission analysis), and the development of a numerical model.

In this thesis I study in details the optical and X-ray emission from protostellar jets. The main results of my multi-wavelength analysis are discussed in Chapter 3 and in Chapter 4, concerning the X-ray and optical emission respectively. In order to study the emission from protostellar jets, I developed a detailed procedure for the multi-wavelength analysis of Hubble (optical) and Chandra (X-ray) observations of the nearest HH protostellar jet from which X-ray emission has been detected in the last few years, HH 154 located in the Taurus star forming region. The main topics here discussed are the measurements of the proper motion of the structures within the jet, their emission and variability, the energetics and the dynamics of protostellar jets in general.

The observations have been used as the basis of the development of a detailed hydrodynamic numerical model of the interaction between a supersonic protostellar jets and the ambient medium, discussed in Chapter 2. In our model we take into account the main physical effects describing the jet-ambient interaction, i. e. the thermal conduction and the radiative losses effects. The results derived from the numerical models can be directly compared with observations, in order to verify our model predictions. To this end I developed a method to synthesize the emission as it could be detected with the last generation satellites, as Chandra, taking into account the absorption due to the presence of the interstellar medium and the instrumental response.

Future perspectives are discussed in Chapter 5, where several models, based on varying initial geometric and physical configurations of the jet-ambient system, are investigated in order to explain the complex scenario of protostellar jets.

In Chapter 6 I draw my conclusions on the experimental and numerical analysis of the emission, both optical and X-rays, from protostellar jets in general and from HH 154, the nearest protostellar jet showing X-ray emission, in particular.

Chapter 2

Numerical model

Prompted by the recent detection of X-ray emission from HH objects discussed in Chapter 1, I developed a detailed hydrodynamic model of the interaction between a supersonic protostellar jet and the ambient medium; the aim is to explain the detailed physics that may lead to the observed X-ray emission. I used the FLASH code (Fryxell et al. 2000) with customized numerical modules that treat optically thin radiative losses and thermal conduction (Orlando et al. 2005).

In this chapter I present the numerical simulations of the jet/ambient interaction. I will discuss the comparison between the predictions derived from my model and the observations of HH 154 collected with both XMM-Newton and Chandra X-ray telescopes (see Appendix B).

The chapter is organized as follows: the model which I developed in order to perform the numerical simulations, the numerical setup, the time scales and the parameters used are presented in Sect. 2.2; I will discuss the main results obtained from the simulations, the morphological evolution, the emission and the spectral analysis in Sect. 2.3; I will draw my conclusions in Sect. 2.4.

2.1 Introduction

As extensively discussed in Chapter 1, X-ray emission associated to HH 154 has been detected with XMM-Newton (Favata et al. 2002). However this observation could not pinpoint the site of the X-ray emission, due to the relatively poor spatial resolution of the XMM-Newton telescope and the authors have hypothesized that the X-ray emission would be associated with the "working surface" (discussed in Chapter 1) of the jet, i.e. the site where the jet collides with the circumstellar medium, corresponding to the D knot in Fig. 2.1, located at a distance of about 1500 AU from the jet origin.

Fig. 2.2 shows the X-ray source from HH 154 as detected with XMM-Newton by Favata et al. (2002) compared with an image in the R-band collected with the

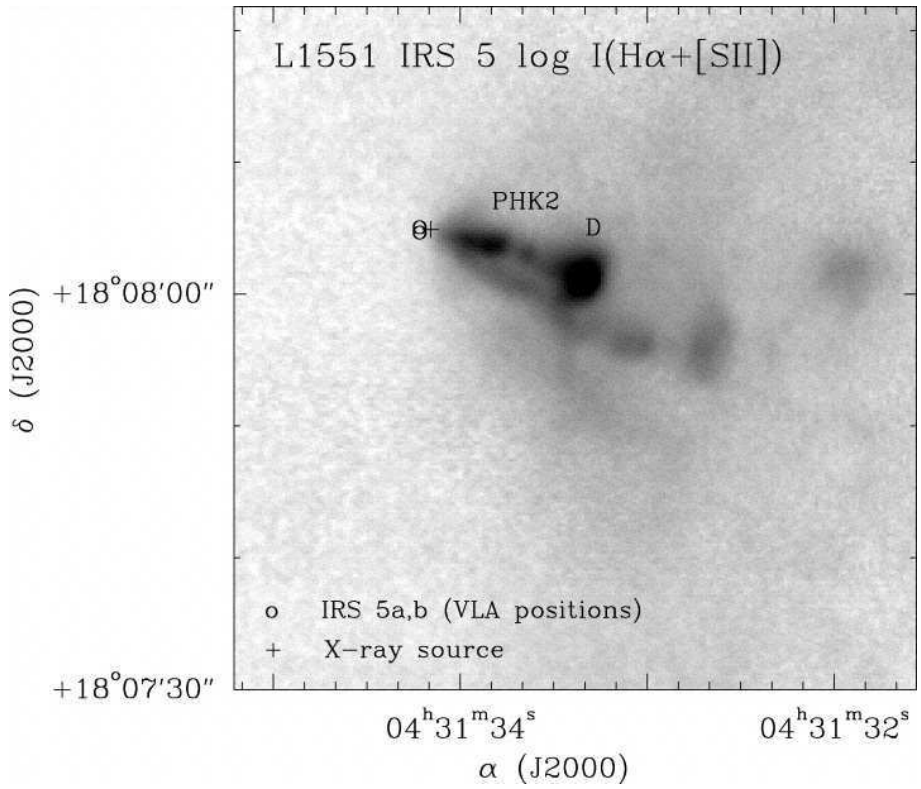

Figure 2.1: Location of the X-ray source, superimposed on an optical image of the HH 154 jet. The optical image shows the sum of H_α and [SII] images obtained with the KPNO 4 m Mayall reflector (Bally et al. 2003).

Hubble Space Telescope WFPC2 camera (see Appendix C for details concerning the Hubble telescope).

The temperature of the X-ray emission ($T = 4.0 \pm 2.5$ MK) determined from XMM-Newton data however, is significantly higher than that expected on the basis of the terminal velocity of the jet. The 2001 Chandra observation (Bally et al. 2003) of the HH 154 jet showed that the X-ray emission in HH 154 comes from a site much closer to the star than the working surface. Fig. 2.1 shows the location of the X-ray source as detected with Chandra in 2001 superimposed on an optical image of the HH 154 jet: the X-ray emission (marked by the cross in the figure) originates close to the basis of the jet, near the binary system IRS 5 (marked by the two circles superimposed on the figure), i.e it is not coincident with the working surface, the D knot at the head of the jet.

Existing observations of X-ray emission from protostellar jets do not allow to constrain the emission mechanism. The distance to the other two known X-ray emitting protostellar jets in Orion is such that no detailed study of their spectrum or variability is possible, while HH 154 is sufficiently nearby and X-ray bright that it has been possible to study both its X-ray spectral characteristics (particularly with XMM-Newton) and its precise spatial location and morphology

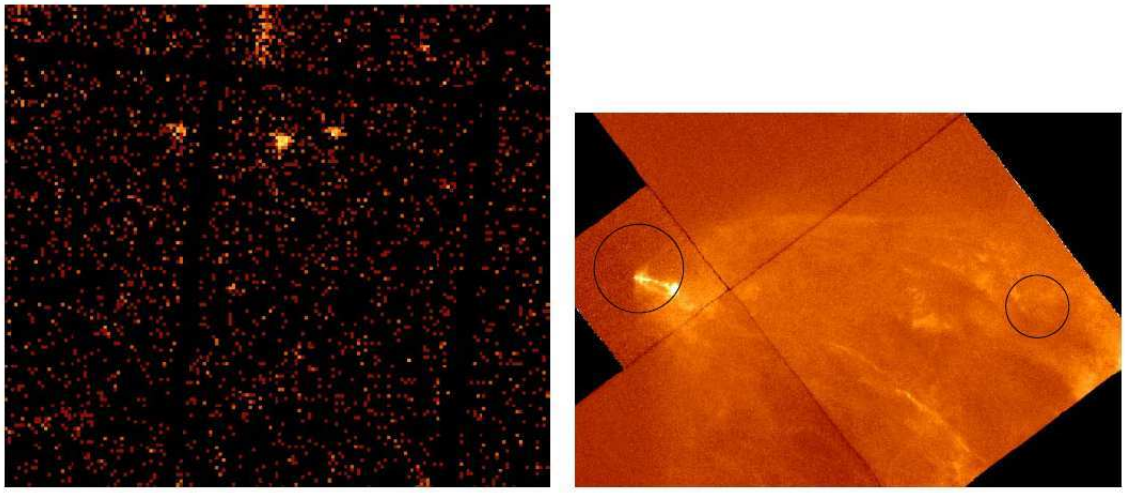

Figure 2.2: The left panel shows the region of L1551 IRS5 in X-rays, as seen in the XMM EPIC-PN camera, while the right panel shows a small part of the same region as seen in a 1800 s R-band CCD image obtained with the Hubble Space Telescope WFPC2 camera. The size of the small detector (the WFPC2-PC chip) on the left part of the HST image is 36.8 arcsec, while the size of the X-ray image is 9.3×6.3 arcmin. The position of the two leftmost X-ray sources visible in the left panel is indicated on the R-band image by the circles. The leftmost X-ray point source is the one associated with L1551 IRS5, while the other point source is a background source (Favata et al. 2002).

(with Chandra) in some detail.

Bally et al. (2003) have proposed several models not based on detailed simulations for the X-ray emission from HH 154. A number of possibilities are discussed, including X-rays scattered from IRS 5 (thus, "coronal" X-ray emission from the IRS 5 protostar reflected by a circumstellar torus, similarly to the model assumed for Seyfert galaxies), co-moving shocks in the jet (conceptually similar to the model we have simulated in detail) and X-rays from fast steady shocks (resulting from the fast stellar winds either hitting the "sides" of the cavity, or the disk). These models are shown in Fig. 2.3.

2.2 The model

I model the propagation of a continuously driven protostellar jet through an isothermal and homogeneous ambient medium. I assume that the fluid is fully ionized and that it can be regarded as a perfect gas with a ratio of specific heats $\gamma = 5/3$. Finally, I assume that any extant magnetic fields are negligible.

The jet evolution is described by the fluid equations for mass, momentum and energy conservation, taking into account the effects of radiative losses and

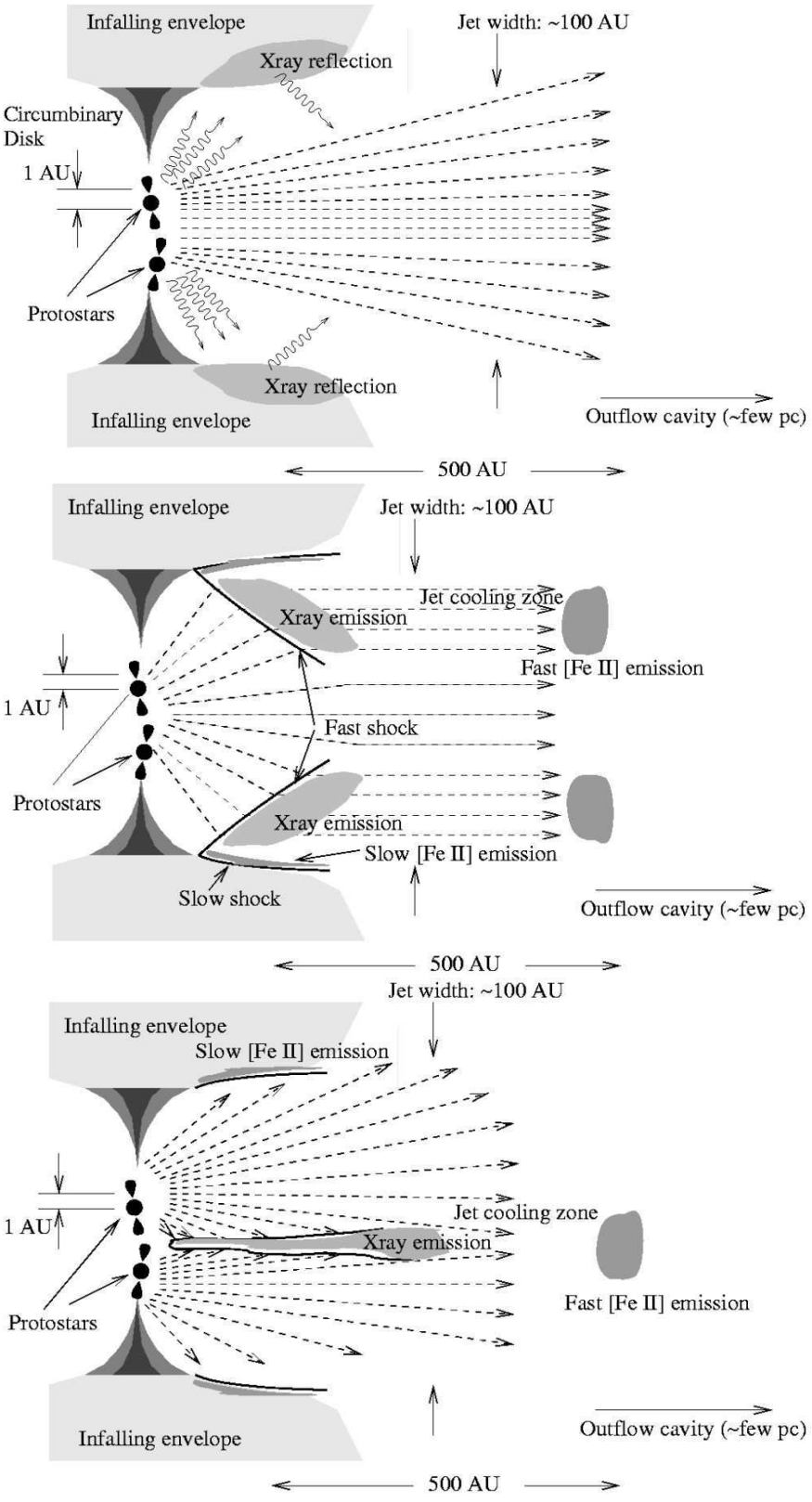

Figure 2.3: Cartoon showing the conceptual models proposed by Bally et al. (2003).

thermal conduction,

$$\frac{\partial \rho}{\partial t} + \nabla \cdot \rho \mathbf{v} = 0 \tag{2.1}$$

$$\frac{\partial \rho \mathbf{v}}{\partial t} + \nabla \cdot \rho \mathbf{v}\mathbf{v} + \nabla p = 0 \tag{2.2}$$

$$\frac{\partial \rho E}{\partial t} + \nabla \cdot (\rho E + p)\mathbf{v} = -\nabla \cdot q - n_e n_H P(T) \tag{2.3}$$

where t is the time, ρ the mass density, $\mathbf{v}$ the plasma velocity, p the pressure, q the heat flux, n_e and n_H are respectively the electron and hydrogen density, $P(T)$ is the optically thin radiative losses function per unit emission measure ($P(T)$ is described by a functional form that takes into account free-free, bound-free, bound-bound and 2 photons emission; see Raymond & Smith 1977; Mewe et al. 1985; Kaastra & Mewe 2000), T the plasma temperature, and

$$E = \epsilon + \frac{1}{2}|\mathbf{v}|^2 \ , \tag{2.4}$$

where E is the specific total energy and ϵ is the specific internal energy. I use the equation of state for an ideal gas,

$$p = (\gamma - 1)\rho\epsilon \ . \tag{2.5}$$

Following Dalton & Balbus (1993), I use an interpolation expression for the thermal conductive flux of the form

$$q = \left(\frac{1}{q_{\rm spi}} + \frac{1}{q_{\rm sat}} \right)^{-1} \ , \tag{2.6}$$

which allows for a smooth transition between the classical and saturated conduction regimes. In the above expression, $q_{\rm spi}$ represents the classical conductive flux (Spitzer 1962)

$$q_{\rm spi} = -\kappa(T)\nabla T \ , \tag{2.7}$$

where $\kappa(T) = 9.2 \times 10^{-7} T^{5/2}$ erg s^{-1} K^{-1} cm^{-1} is the thermal conductivity. The saturated flux, $q_{\rm sat}$, is given by (Cowie & McKee 1977)

$$q_{\rm sat} = -sign(\nabla T) 5 \phi \rho c_{\rm s}^3 \ , \tag{2.8}$$

where $\phi \sim 0.3$ (Giuliani 1984; Borkowski et al. 1989, and references therein) and $c_{\rm s}$ is the isothermal sound speed.

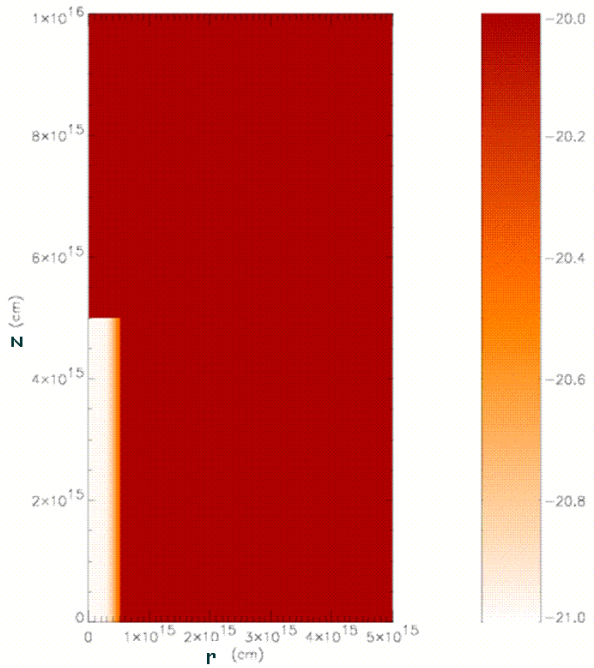

Figure 2.4: Density map of the case of a protostellar jet less dense than the ambient medium. The initial configuration of the protostellar jet in the computational domain is a cylinder with the axis along the z axis.

2.2.1 Numerical setup

Initially, the jet has been simulated adopting a rotationally symmetric cylindrical jet impacting upon a homogeneous medium, as shown in Fig. 2.4.

I adopt a 2-D cylindrical (r, z) coordinate system, with the jet axis coincident with the z-axis. The computational grid size in dimensional form varies from ≈ 300 AU to ≈ 600 AU in the r direction and from ≈ 6000 AU to $\approx 3 \times 10^4$ AU in the z direction, where the particulars of these dimensions are chosen so that I are able to follow the jet/ambient medium interaction for at least 20-50 years.

In the case of a jet less dense than the ambient medium (hereafter called a "light jet") that best reproduces observations, the integration domain extends over 300 AU in the radial direction and over 6000 AU in the z direction. In the case of the jet with the same initial density as the ambient medium (hereafter referred to as an "equal-density jet") that best reproduces observations, the domain is $(r \times z) \approx (600 \times 6000)$ AU. In this latter case, the radial axis is twice as large as in the light jet case because the cocoon surrounding the equal density jet has a radial extension greater than in the light jet case. The dimension of the computational domain in the case of a jet denser than the ambient medium (hereafter, a "heavy jet") that best reproduces observations is $(r \times z) \approx (700 \times 27000)$ AU.

In all of these cases, the initial jet velocity is along the z axis, coincident with

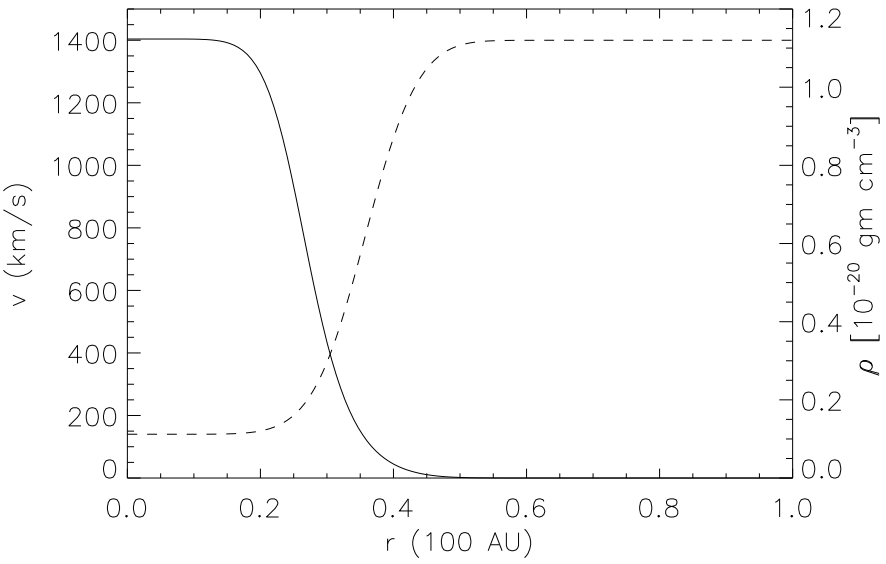

Figure 2.5: Initial jet velocity, $V(r)$, (continuous line) and density, $\rho(r)$, (dashed line) as a function of the distance from the axis, r, for the light jet case discussed in Section 2.3.2 with parameters: $\mathcal{M} = 300$, $\nu = 10$, $n_j = 500$ cm^{-3}, $T_a = 10^3$ K, $r_j = 30$ AU, $w = 4$ (see Table 2.2).

the jet axis, and has a radial profile of the form

$$V(r) = \frac{V_0}{\nu \cosh(r/r_j)^w - (\nu - 1)} \ , \tag{2.9}$$

where V_0 is the on-axis velocity, ν is the ambient to jet density ratio, $r_{\rm j}$ is the initial jet radius and $w = \mathbf{4}$ is the steepness parameter for the shear layer (as an example, see the continuous line in Fig. 2.5, for the light jet case discussed in Section 2.3.2, with corresponding parameters given in Table 2.2), adjusted so as to achieve a smooth transition of the kinetic energy at the interface between the jet and the ambient medium.

The density variation in the radial direction (dashed line in Fig. 2.5) is given by

$$\rho(r) = \rho_j \left(\nu - \frac{\nu - 1}{\cosh(r/r_j)^w} \right) \ , \tag{2.10}$$

where $\rho_{\rm j}$ is the jet density (Bodo et al. 1994).

Reflection boundary conditions are imposed along the jet axis, inflow boundary conditions are imposed at $z = 0$ and $r \leq r_{\rm j}$, and outflow boundary conditions are assumed elsewhere.

The maximum spatial resolution achieved in the best light jet case (in both the r and z directions) is ≈ 1.3 AU, as determined from the PARAMESH methodology for 4 refinement levels, which corresponds to covering the jet radius with 25

points at the maximum resolution. The spatial resolution achieved in the equal-density case is half that obtained in the light jet case; and the spatial resolution achieved in the best heavy jet model is 8 times lower than in the light jet case.

Our choice of different spatial resolutions for these three cases was dictated by the need to limit the computational cost; this constraint arises because the solver for thermal conduction is explicit in our version of FLASH and, therefore, a time-step limiter depending on density, ρ, temperature, T, and spatial resolution, Δx, is required in order to avoid numerical instability (see, for instance, Orlando et al. 2005). Stability is guaranteed for $\Delta t < 0.5\ \Delta x^2/D$, where D is the diffusion coefficient, related to the conductivity, κ, and to the specific heat at constant volume,c_v, by $D = \kappa(T)/(\rho c_v)$. Thus, calculations involving high temperatures (as, for instance, in the heavy jet case) are especially constrained, and therefore a lower spatial resolution is required in order to avoid a very small time-step, Δt.

Characteristic time-scales

Condensations of plasma due to radiative cooling effects can become thermally unstable; however, the presence of thermal conduction can prevent such instabilities. By comparing the radiative, $\tau_{\rm rad}$, and thermal conduction, $\tau_{\rm cond}$, characteristic times (using the CGS System of Units)

$$\tau_{\rm rad} = \frac{p}{(\gamma-1) n_e n_H P(T)} \approx 2.5 \times 10^3 \frac{T^{3/2}}{n} \tag{2.11}$$

$$\tau_{\rm cond} \approx \frac{p}{\gamma-1}\frac{7}{2}\frac{l^2}{\kappa(T)T} \approx 1.5 \times 10^{-9} \frac{n l^2}{T^{5/2}}\ , \tag{2.12}$$

where l represents the characteristic length scale of temperature variations, I can infer which of the two competing processes dominates during the jet/ambient medium interaction. From the condition

$$\left(\frac{\tau_{\rm rad}}{\tau_{\rm cond}}\right)^{1/2} = 1 \tag{2.13}$$

I can derive the cutoff length scale for instability, $l_{\rm F}$ (Field 1965), which indicates the maximum length (using the CGS System of Units)

$$l_{\rm F} \approx 1.3 \times 10^6 \frac{T^2}{n} \tag{2.14}$$

over which thermal conduction dominates over radiative effects in the classical conduction regime. An analogous estimate in the saturation regime leads to

$$(l_{\rm F})_{\rm sat} \approx 3 \times 10^7 \frac{T^2}{n}\ , \tag{2.15}$$

which is one order of magnitude longer than the characteristic length in the classical regime. As discussed later in Section 2.3.2, the comparison between the classical Field length (the shortest characteristic length) and the size of the region behind the shock at the head of the jet will allow us to determine if this region is thermally stable or not.

In order to verify our assumption of a fully ionized gas, I computed the ionization time scale of the most relevant elements in the X-ray spectrum of a shocked plasma at $T = 3.4 \times 10^6$ K, assuming a post-shock density of about 10^4 cm^{-3} (the light jet case). As an example, I can show that the ionization time scale for C and O is 1 to 2 orders of magnitudes smaller than the radiative and thermal conduction time scales, so that the plasma indeed can be considered to be in ionization equilibrium.

2.2.2 Parameters

Our model solutions depend upon a number of physical parameters, such as, for instance, the jet and ambient temperature and density, the jet velocity and its radius. In order to reduce the number of free parameters in our exploration of the parameter space, I have fixed the jet radius to $r_j \approx 30$ AU, following Favata et al. (2002) (who found this characteristic linear scale from the X-ray thermal fit), and Fridlund et al. (2005) (who showed HST images of the internal knots of HH 154 with dimension $r \approx 30$ AU at the base of the jet[1]). However, detailed simulations with different r_j values are not necessary since I can predict the effects of varying the jet radius from the model results I obtained so far. In fact I expect the X-ray emitting region to grow in size as r_j grows. Since the X-ray luminosity is defined as $L_{\rm X} = n^2 V P(T)$, it depends on the cube of the radius. This means that, as $L_{\rm X}$ is constrained from observations, a jet with a greater radius needs a lower density in order to reproduce observations. I impose an initial jet length $z_j = 300$ AU in order to avoid the ejected plasma that travels back inside the boundary during the jet evolution. This choice of a non-zero initial jet length allows us to obtain an unperturbed boundary surface at $z = 0$. In all our simulations, I model a jet with initial density and temperature $n_{\rm j} = 500$ cm $^{-3}$ and $T_{\rm j} = 10^4$ K, respectively, following the values derived from observations (Fridlund & Liseau 1998 and Favata et al. 2002). The density and temperature of the ambient medium, $n_{\rm a}$ and $T_{\rm a}$ respectively, are derived from the choice of the ambient medium-to-jet density contrast, ν and from the hypothesis of initial pressure balance between the ambient medium and the jet. I am left, therefore,

[1]In Fridlund et al. (2005), page 993, the authors discuss the working surface. The radius quoted is that of the elongated Mach disk (probably representative of the jet), and is ≈ 30 AU. The separation between the Mach disk and the working surface is 0.6" or 4 times this ≈ 100 AU (M. Fridlund, private communication).

Table 2.1: Range of parameters used in our numerical model (column 2) compared with typical outflow parameters (column 3 and 4) shown in Bally & Reipurth (2002), Table 1. ν is the ambient medium to jet density contrast; $\mathcal{M}$ is the Mach number; T_a and n_a are the ambient medium temperature and density, respectively; $v_{\rm j}$ is the initial jet velocity; $v_{\rm sh}$ is the shock velocity of the knots inside the jet; $\dot{M}$ is the mass loss rate; and $L_{\rm mech}$ is the mechanical luminosity.

Parameter	Model	Low Mass[a]	High Mass[a]	Units
ν	$0.01 \div 300$	–	–	–
$\mathcal{M}$	$1 \div 1000$	–	–	–
T_a	$30 \div 10^6$	–	–	K
n_a	$5 \div 10^5$	–	–	cm^{-3}
$v_{\rm j}$	$85 \div 8500$	–	–	km s^{-1}
$v_{\rm sh}$	$100 \div 2000$	$100 \div 300$	$100 \div 1000$	km s^{-1}
$\dot{M}$	$10^{-10} \div 10^{-8}$	$10^{-9} \div 10^{-5}$	$10^{-6} \div 10^{-2}$	$M_\odot$ yr^{-1}
$L_{\rm mech}$	$6.7 \times 10^{-5} \div 67$	$0.001 \div 1$	$0.1 \div 1000$	$L_\odot$

[a] Bally & Reipurth (2002)

with two non-dimensional control parameters: the jet Mach number, $\mathcal{M}$, and the ambient medium-to-jet density contrast, ν. For a more extended exploration of the parameter space, see Section 2.3.5, which explores the variation of the initial jet density, $n_{\rm j}$. In our simulations I account for the wide jet/ambient medium parameters range shown in Table 2.1.

In Section 2.3, I discuss the results derived from the exploration of the parameter space defined by $\mathcal{M}$ and ν.

2.2.3 Synthesizing the X-ray spectra

From our 2-D numerical simulations, I synthesized the absorbed focal plane spectra to be compared with observations by using the following procedure, shown also in Fig. 2.6.

As a first step, from the integration of the hydrodynamic Eqs. 2.1, 2.2 and 2.3, I derive the temperature and density 2-D distributions in the computational domain. I then reconstruct the 3-D spatial distribution of these physical quantities by rotating the 2-D slabs around the symmetry axis. This allows us to derive the emission measure, defined as $EM = \int n_e n_{\rm H} dV$ (where n_e and $n_{\rm H}$ are the electron and hydrogen densities, respectively, and V is the volume of emitting plasma).

From the 3-D spatial distributions of T and EM, I derive the distribution of emission measure $EM(T)$ for the computational domain as a whole or for part of it: I consider the temperature range $[10^3 - 10^8]$ K, divided into 74 bins equispaced

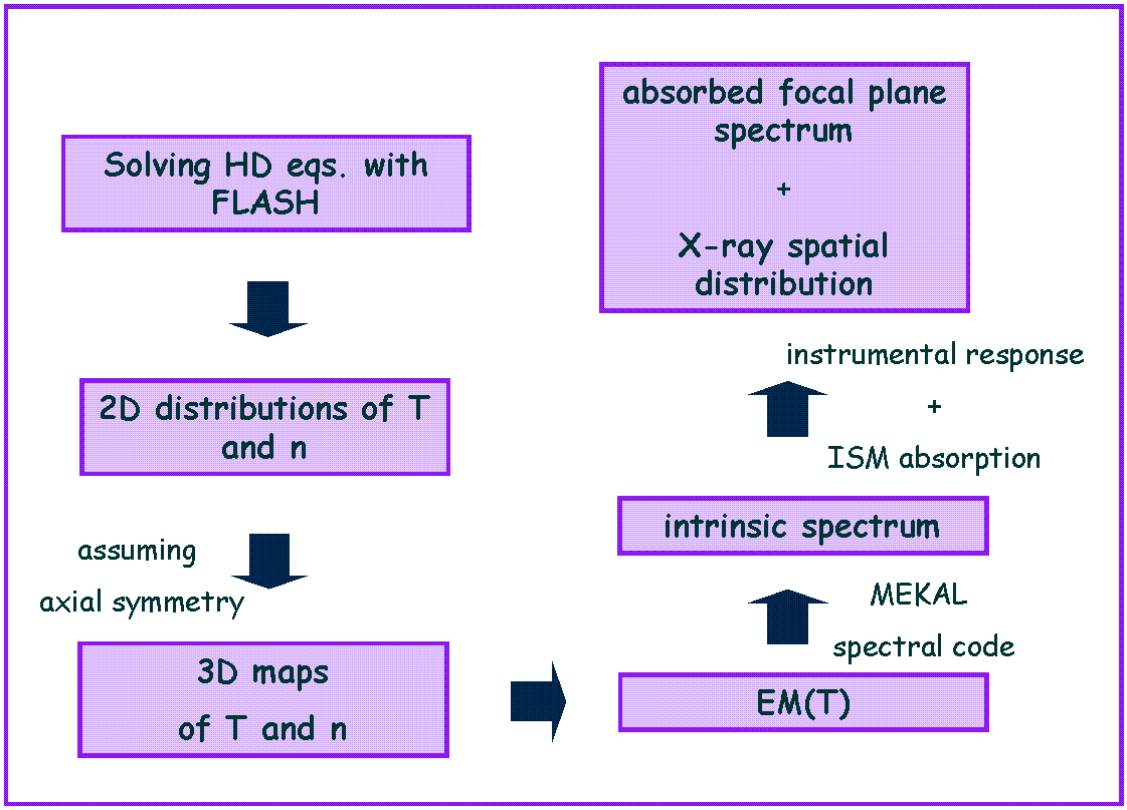

Figure 2.6: Main steps of the procedure used to derive the focal plane spectra. See text for a complete description.

in $\log T$; the total EM in each temperature bin is obtained by summing the emission measure of all the fluid elements corresponding to the same temperature bin.

From the $EM(T)$, using the MEKAL spectral code (Mewe et al. 1985) for optically thin plasmas, I derive the number of photons in the i-th energy bin as follows:

$$I_i = \frac{1}{4\pi D^2} \sum_k \int_{E_i}^{E_{i+1}} \frac{P(T_k, E) EM(T_k)}{E} dE \ , \tag{2.16}$$

where D is the distance of the object from us, E_i is the energy in the i-th bin, $P(T_k, E)$ describes the radiative losses as a function of energy and of the temperature in the k-th bin.

To compare our model results with observations, I synthesize the focal plane spectrum, C_i, as predicted to be observed with the *Chandra*/ACIS-I or XMM-*Newton*/EPIC-pn X-ray imaging spectrometers, taking explicit account of the spectral instrumental response:

$$C_i = \frac{t_{exp}}{4\pi D^2} \sum_k \int_{E_i}^{E_{i+1}} A(E) M(i, E) \times \frac{P(T_k, E) EM(T_k)}{E} dE \tag{2.17}$$

where t_{exp} is the exposure time, $A(E)$ is the energy-dependent effective area and $M(i, E)$ is the instrumental response.

Finally, I take into account the interstellar medium absorption column density, $N_{\rm H}$ (Morrison & McCammon 1983), and analyze the absorbed focal plane spectrum with XSPEC V11.2 in order to compare our findings with published observational results.

2.3 Results

2.3.1 Exploration of the parameter space

I performed a broad exploration of the control parameter space defined by the two free parameters, the jet Mach number, $\mathcal{M} = v_{\rm j}/c_{\rm a}$, and the ambient medium-to-jet density ratio, $\nu = n_{\rm a}/n_{\rm j}$ (see Section 2.2.2). The aim is to determine the range of parameters leading to X-ray emission from protostellar jets that is in agreement with the observations.

I first analyzed adiabatic hydrodynamic models, i.e., models without thermal conduction and radiative losses. Then, for the most promising cases (i.e., for those adiabatic cases that most closely reproduce the values of jet velocity, temperature and luminosity of the X-ray source derived from the observations), I performed more realistic simulations in which I have taken into account thermal conduction and radiative loss effects. By comparing these latter models with those without thermal conduction and radiative cooling, I am able to explore how the presence of these physical processes affects the jet/ambient medium system evolution. I found that, in general, models with thermal conduction and radiation reach lower temperatures (up to 5 times lower than those achieved in the adiabatic cases). I also found that thermal conduction smooths the density and temperature spatial structures that are well visible in the pure hydrodynamic cases.

In the following subsections, I discuss the models (shown in Fig. 2.7) in which both radiative losses and thermal conduction are taken into account. In Fig. 2.7 green and red dots refer to those cases with X-ray luminosity $L_X > 10^{28}$ erg s^{-1}, shock front velocity $v_{sh} > 100$ km s^{-1} and fitting temperature $T < 10^7$ K, consistent with observations. I have chosen L_X one order of magnitude lower than the minimum value observed (see Table 1.1) in order to take into account fainter sources that have not as yet been detected; the red dot refers to the representative case of HH 154 discussed in Bonito et al. (2004). Squares show cases with velocities in the range of values observed, but with $L_X < 10^{28}$ erg s^{-1}; diamonds mark the cases with velocities and X-ray luminosity not consistent with observations; and triangles mark cases with temperatures higher than 10^7 K. The lower panel of Fig. 2.7 shows the initial velocity assumed in our simulations vs. the density contrast.

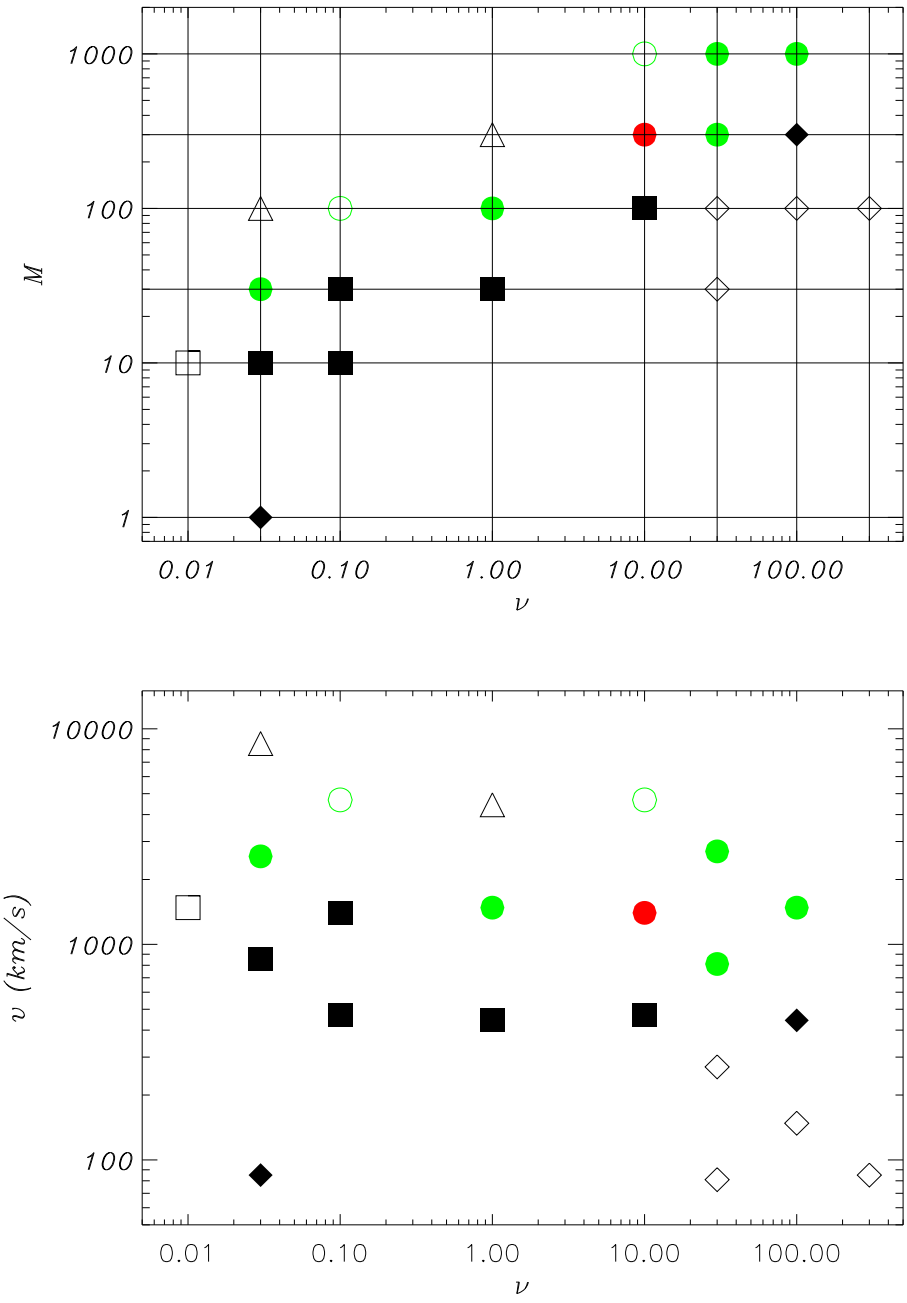

Figure 2.7: Exploration of the parameter space: jet Mach number, $\mathcal{M}$ (upper panel) and initial jet velocity (lower panel) as a function of the ambient-to-jet density contrast, ν. Green and red dots refer to models consistent with observations for X-ray luminosity, shock velocity and fitting temperature values (see text); diamonds refer to models which cannot reproduce observations; squares refer to models in good agreement with observations for shock velocity but not for X-ray luminosity values; triangles refer to models with too high ($T \geq 10^7$ K, one order of magnitude higher than observed) temperature. Empty symbols refer to pure hydrodynamic simulations; filled symbols refer to models in which thermal conduction and radiative losses effects are taken into account.

Table 2.2: Summary of the initial physical parameters characterizing the "best-fit" models in the case of light, equal-density and heavy jets: ambient-to-jet density contrast, ν, jet Mach number, $\mathcal{M}$, initial jet velocity, $v_{\rm j}$, ambient density and the temperature, $n_{\rm a}$, and $T_{\rm a}$, respectively. In all the models, the initial jet density and temperature are $n_{\rm j} = 500$ cm $^{-3}$ and $T_{\rm j} = 10^4$ K, respectively.

model	ν	$\mathcal{M}$	$v_{\rm j}$ [km s^{-1}]	$n_{\rm a}$ [cm^{-3}]	$T_{\rm a}$ [10^4 K]
light	10	300	1400	5000	0.1
equal-density	1	100	1500	500	1
heavy	0.03	30	2500	17	30

From our exploration of the parameter space, I am able to show that the models in agreement with observations lie within a well constrained region in our parameter space. In the following sections, I discuss in detail the "best-fit" models, i.e., those models that reproduce X-ray luminosity and shock front speed values as close as possible to those observed, for the three cases of light, equal-density and heavy jets (see Table 2.2).

2.3.2 Hydrodynamic evolution

In Fig. 2.8, I show the mass density and temperature distributions 20 years after the beginning of the jet/ambient medium interaction for the three best-fit models in Table 2.2. The light jet case best reproduces the physical parameters derived from observations by Fridlund & Liseau (1998) and Favata et al. (2002) for the HH 154 protostellar jet; its properties have been discussed in Bonito et al. (2004).

In all cases, there is clear evidence at the head of the jet of a shock front due to the plasma propagating supersonically along the jet axis. Just behind the shock front there is a localized hot and dense "blob" that can be seen clearly, for instance, in the enlargement of the shock front shown in Fig. 2.9 for the light jet case.

The light jet is enveloped by a cocoon whose temperature T ($\approx 7 \times 10^5$ K) is spatially almost uniform due to thermal conduction; nevertheless, the cocoon temperature is not constant in time but decreases as the evolution proceeds, leading to the formation of a cool and dense external envelope. Fig. 2.10 shows traces of the density (continuous line) and temperature (dashed line) along the radius at $z \approx 5000$ AU, corresponding to the blob position 40 years since the beginning of the jet/ambient medium interaction: the hot (few million degrees) and dense blob is evident for $r < 10$ AU. The density decreases moving away from the jet axis along the radial direction, then increases again at the position corresponding to the external part of the cocoon. In contrast, the temperature

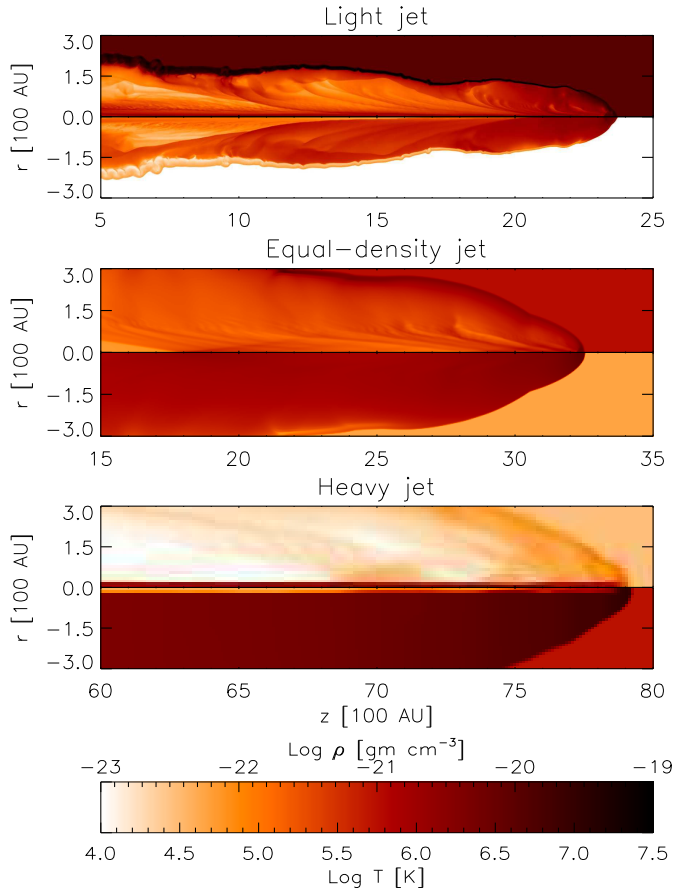

Figure 2.8: Two-dimensional mass density (upper half-panels) and temperature (lower half-panels) cuts in the $r-z$ plane after 20 years since the beginning of the jet/ambient medium interaction for the best cases of light (upper panels), equal-density (middle panels) and heavy jets (lower panels).

monotonically decreases as one moves away from the jet axis along the radial direction. The blob therefore is expected to be an X-ray source; in Section 2.3.4, I will show that this X-ray source has a luminosity and spectral characteristics consistent with those observed.

The central double panel in Fig. 2.8 shows 2-D sections in the (r, z) plane of the mass density and temperature distributions for the best-fit equal-density model (see Table 2.2). The interaction between the protostellar jet and the ambient medium leads to a dense and hot cocoon ($n \approx 1400$ cm^{-3}; $T \approx 2 \times 10^6$ K) surrounding the jet. Once again, the cocoon's temperature is spatially almost uniform (because of thermal conduction), and this temperature decreases with time. Thus, this cocoon gradually cools and becomes denser with time, just as in the light-jet case. Again, the post-shock region shows evidence for a hot and dense blob from which the X-ray emission originates (see Section 2.3.4 for more details).

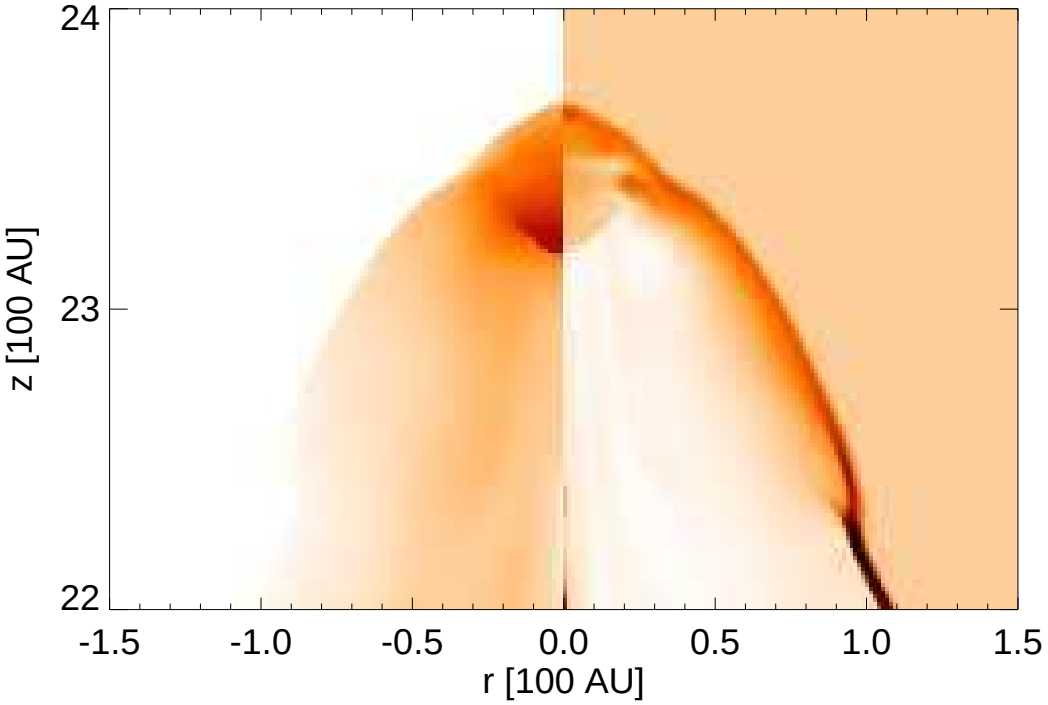

Figure 2.9: An enlargement of the post shock region in the light jet case for temperature (left) and density (right) in linear scale, obtained about 20 years after the beginning of the jet/ambient medium interaction. Note the hot and dense region just behind the shock front.

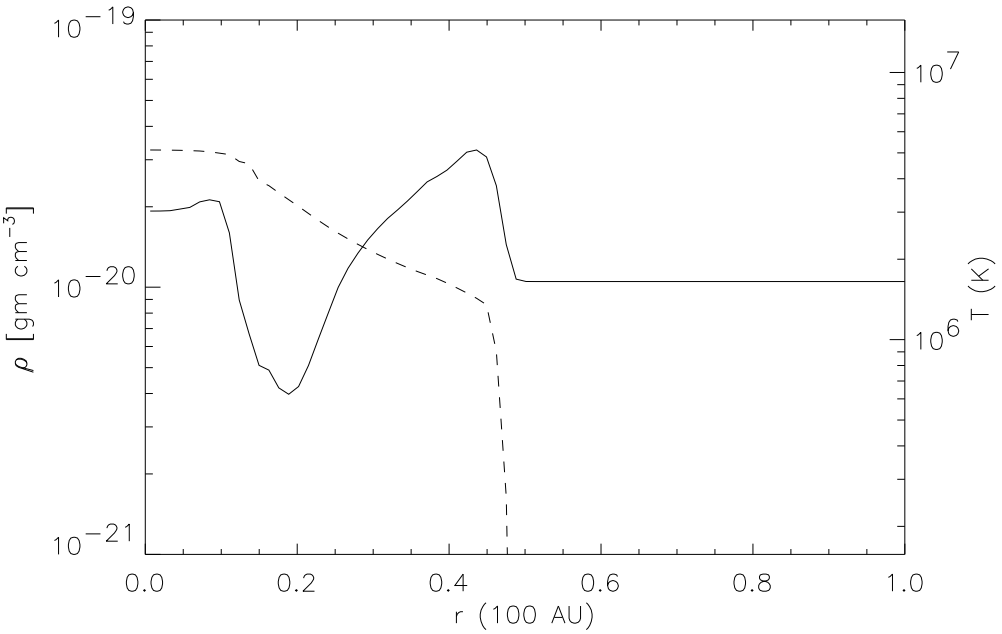

Figure 2.10: Density (continuous line) and temperature (dashed line) profiles along the radial direction at $z \approx 5000$ AU, corresponding to the blob position at $t = 40$ yr ($\mathcal{M} = 300$, $\nu = 10$).

In the heavy-jet case (lower double panel in Fig. 2.8), the jet is surrounded by a cocoon that is well smoothed by the effects of thermal conduction and whose

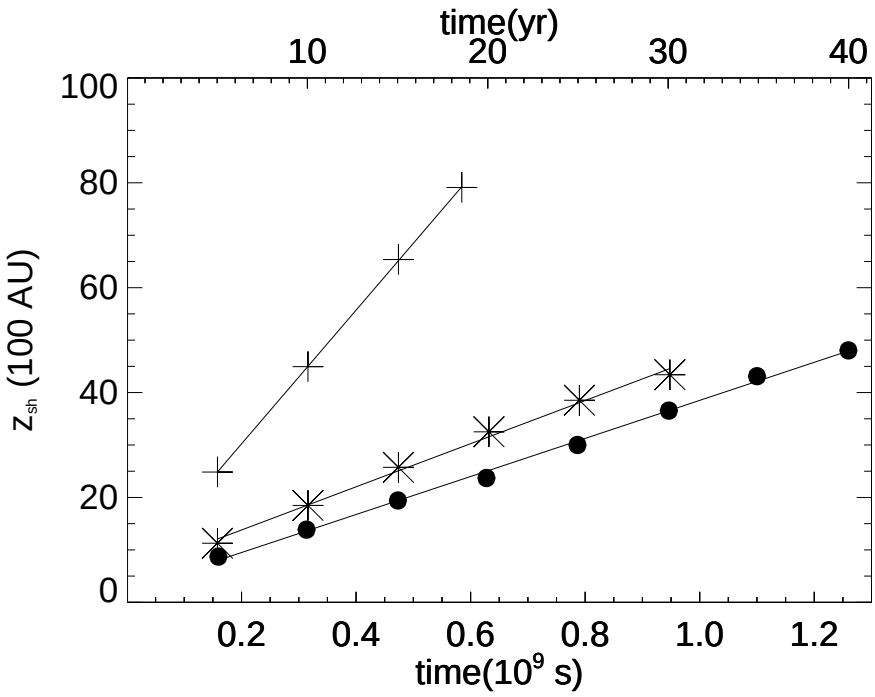

Figure 2.11: Shock front position vs. time. Dots mark the light jet case, stars the equal-density jet, and crosses the heavy jet case. The lines refer to the best fit, from which I derive the average shock speed: $v_{\rm sh} \approx 500$ km s^{-1}, ≈ 600 km s^{-1}, ≈ 1900 km s^{-1} for the light, equal-density and heavy jet case, respectively.

radial extension is larger than that in the other two cases. The cocoon has temperature of a few million degrees, and its density is lower than that of the jet.

For the three best-fit models just discussed, I analyzed the thermal stability of the hot and dense blob localized behind the shock by comparing the size of the blob with the Field length, Eq. 2.14. In the light jet case, the values obtained for the average blob temperature, $T \approx 3.4 \times 10^6$ K, and density, $n \approx 6500$ cm^{-3}, lead to $l_{\rm F} \sim 100$ AU. Since the blob size (which is almost equal to twice the initial jet radius $r_{\rm j} \approx 30$ AU; see Fig. 2.9) is smaller than $l_{\rm F}$, it appears that the blob is thermally stable. In the equal-density jet case, the density and temperature of the blob at the head of the jet are $n \approx 1700$ cm^{-3} and $T \approx 4.3 \times 10^6$, respectively, leading to $l_{\rm F} \approx 10^3$ AU. Also in this case, therefore, I can conclude that the blob is thermally stable, given that its size (~ 100 AU) is roughly 10 times smaller than the Field length. Finally, in the heavy-jet case, the temperature and density of the blob are $T \sim 10^7$ K and $n \sim 10^2$ cm^{-3}, leading to $l_{\rm F} \approx 10^4$ AU. Since the blob behind the shock front now extends over ~ 100 AU, it is thermally stable in this case as well. To summarize: in all of the cases considered in which the predicted X-ray properties agree with observations, I find that the emitting "blob" is thermally stable.

The position of the shock front as a function of time for the three best-fit

models in Table 2.2 is shown in Fig. 2.11. For the light jet case, I derived an average shock velocity $v_{\rm sh} \approx 500$ km s^{-1}, about 3 times lower than the initial jet velocity. This shock velocity is in good agreement with observed speeds in HH objects, and in particular with that derived from HH 154 data. Taking into account the jet inclination ≈ 45 degrees (Fridlund & Liseau 1998), $v_{\rm sh} \approx 500$ km s^{-1} corresponds to a proper motion of ≈ 350 km s^{-1}, which (at the distance of HH 154) can be measured with well time-spaced *Chandra* observations.

In the equal-density jet scenario, I deduced an average shock velocity $v_{\rm sh} \approx 600$ km s^{-1}, slightly greater than the value observed in HH 154 (Fridlund & Liseau 1998; Favata et al. 2002), but consistent with values observed in other HH objects (see Tab. 1.1). For the heavy jet case, the average value of the shock speed is $v_{\rm sh} \approx 1900$ km s^{-1} which is too high with respect to the HH velocities observed (cf. Tab. 1.1).

2.3.3 Emission measure distribution vs. temperature

I derived the distribution of emission measure vs. temperature, $EM(T)$, in the temperature range $[10^3 - 10^8]$ K at different stages of the evolution of the jet/ambient medium system (see Sect. 2.2.3 for more details). Fig. 2.12 shows the $EM(T)$ for the three best-fit models in Table 2.2 20 years after the beginning of the jet/ambient medium interaction.

In all of these cases, I find that the shape of the $EM(T)$ is characterized by two bumps, and does not change significantly during the system evolution. The relative weight of the bumps is different in the three cases. In the light jet case (upper panel in Fig. 2.12), the bumps are quite broad, the first centered at temperature $T \sim 10^4$ K with $EM \sim 10^{55}$ cm^{-3}, and the second one centered at $T \sim 10^6$ K with $EM \sim 10^{52}$ cm^{-3}, about three orders of magnitude lower than the first bump; the EM decreases rapidly above few millions degrees.

In the equal-density jet case (middle panel in Fig. 2.12), the first bump is centered at $T \sim 10^4$ K with $EM \geq 10^{54}$ cm^{-3}, whereas the second bump is centered at $T \sim 10^6$ K with $EM \sim 10^{52}$ cm^{-3}, just as in the light jet case. Finally, in the heavy jet case (lower panel in Fig. 2.12), the $EM(T)$ distribution appears flat, with two weak peaks centered at $T \sim 10^4$ K and at a few million degrees. Note that in the heavy jet case, the EM at temperatures up to a few million degrees is two orders of magnitude lower than in the light jet case.

On the basis of these $EM(T)$ distributions, I expect a bright ($L_{\rm X} > 10^{28}$ erg s^{-1}) X-ray source, whose soft component (due to the cocoon) could be suppressed by the strong interstellar medium absorption (Favata et al. 2002). I also expect that the X-ray emission decreases as the ambient medium-to-jet density ratio, ν, decreases, leading to brighter X-ray emission in the light jet case.

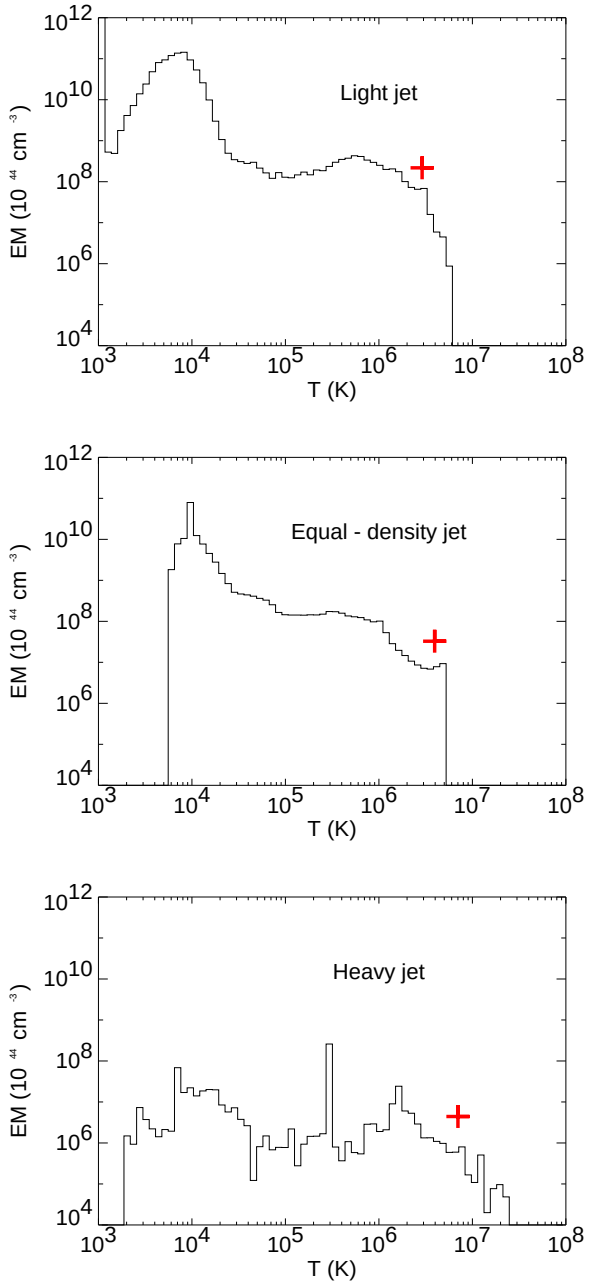

Figure 2.12: Emission measure, EM, as a function of the temperature, T for the three models discussed in the text, at a time 20 years after the beginning of the jet/ambient medium interaction. The cross superimposed on each panel marks the best-fit temperature and emission measure values derived from our simulated absorbed spectra.

2.3.4 X-ray emission

From the $EM(T)$ distributions and the MEKAL spectral code, I have synthesized the focal plane spectra as predicted to be detected with the instruments on board XMM-*Newton* and *Chandra* (see Sect. 2.2.3 for details); in deriving

these predictions, I have taken into account interstellar absorption. In order to compare our numerical models with experimental data concerning HH 154 (the closest and best studied jet emitting in the X-ray band), I assumed a distance of 150 pc (as HH 154 is located in the L1551 cloud in the Taurus star-forming region) and an interstellar absorption column density $N_{\rm H} = 1.4 \times 10^{22}$ cm^{-2} (Favata et al. 2002). Our model results can be generalized to account for the other HH objects observations by considering different values for the distance and the interstellar absorption.

Spatial distribution of the X-ray emission

Assuming that the jet propagates perpendicularly to the line of sight, I computed predicted X-ray images of the jet/ambient medium system from our numerical simulations, to be compared with images obtained with the high spatial resolution *Chandra*/ACIS-I instrument (see Sect. 2.2.3). The analysis of ACIS-I data is interesting because of its high spatial resolution, which allows to localize the X-ray source in the jet with high precision (see Bally et al. 2003). For all the models in Table 2.2, I am able to show that most of the X-ray emission produced during the jet/ambient medium interaction originates from a very compact region localized at the head of the jet, just behind the shock front.

Fig. 2.13 shows an enlargement of the head of the jet (where most of the X-ray emission originates) of our predicted X-ray images, to be compared with *Chandra*/ACIS-I images; our predicted images are assumed to correspond to the jet 20 years after the beginning of the jet/ambient medium interaction. Note that the spatial resolution of the synthesized X-ray images in Fig. 2.13 is 6 times better than that of the *Chandra*/ACIS-I. In all three cases analyzed, a comparison between the X-ray emitting region and the temperature and density maps in Fig. 2.8 shows that the X-ray source is coincident with the hot and dense blob discussed in Section 2.3.2.

I find that even with *Chandra*'s high spatial resolution, the predicted X-ray emitting region cannot be spatially resolved, and so I expect that it will be detected as a point-like source. Furthermore, I expect that significant X-ray emission will be seen only from the hot and dense blob behind the shock front, as the softer cocoon emission is likely to be extinguished by the strong interstellar absorption.

As discussed in Section 2.3.2, the X-ray emitting region for the three cases examined is thermally stable, and therefore the X-ray emission should be continuously detectable during the 20-50 years analyzed. I also found that there are no significant variations of the X-ray source morphology during the evolution: the source size varies by $\pm 25\%$, always below the spatial resolution achievable with *Chandra*. However, for some of the cases shown in Fig. 2.7, our analysis

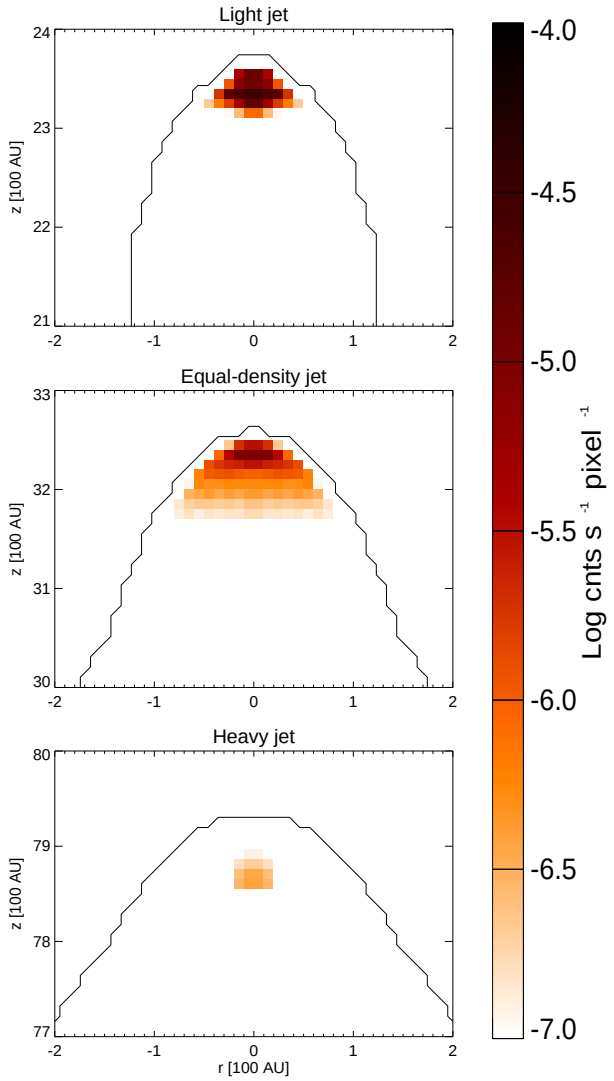

Figure 2.13: Synthesized X-ray emission, in logarithmic scale, as predicted to be observed with ACIS-I, for the three cases examined, 20 years since the beginning of the jet/ambient medium interaction. At a distance $D \approx 150$ pc, 100 AU corresponds to about 0.7 arcsec

predicts transient behaviour of the X-ray source, which extinguishes a few years after the beginning of the interaction between the protostellar jet and the ambient medium, because of radiative cooling that dominates thermal conduction effects.

From Fig. 2.11, the X-ray source coincident with the hot and dense blob discussed in Section 2.3.2 has a proper motion of ~ 0.7 arcsec/yr, ~ 0.8 arcsec/yr, and ~ 2.7 arcsec/yr in the light, equal-density and heavy jet cases, respectively, under the assumption that the jet axis is perpendicular to the line of sight. In addition, I find that the intensity of the X-ray source decreases about one order of magnitude as the ambient medium-to-jet density contrast, ν, decreases. Note that the heavy jet case has the higher shock front speed and the lower X-ray emission.

Spectral analysis

I derived the synthesized focal plane spectra predicted to be observed with XMM-*Newton*/EPIC-pn, an instrument characterized by a large effective area, with the aim of comparing our model results with published data and, in particular, with those data concerning HH 154 (Favata et al. 2002).

I considered two different levels of count statistics in the $[0.3-10]$ keV band: in the low statistics case, I have fixed the exposure time so as to obtain about 100 total photons for each spectrum, whereas in the high statistics case, I imposed about 10^4 counts for each spectrum. Although the latter case is unrealistic (given the low photon counts so far collected from these sources), it can help us to pinpoint some of fundamental features of the predicted spectra. The spectral bins are grouped together to have at least 10 photons in the low count statistics case and 20 photons in the other case.

As an example, in Fig. 2.14, I present the synthesized spectra, with the best-fit thermal (MEKAL) spectra superimposed, 25 years since the beginning of the jet/ambient medium interaction. The top panel shows the unabsorbed parent spectrum derived from the original EM(T) distribution of the whole spatial domain; the middle and bottom panels show the EPIC-pn spectra derived in the low and high statistics cases, respectively.

In Fig. 2.15, I compare the synthesized spectrum 25 years since the beginning of the jet-ambient interaction with the Favata et al. (2002) observations. The MEKAL best-fit spectrum is also shown. Assuming a distance of about 150 pc I obtained 1.2 cnts ks^{-1} in the $[0.3-10]$ keV band with an absorbing column density of 1.5×10^{22} cm^{-2} (Tab. 2.3). The fitting parameters derived from our model (Tab. 2.3) are consistent with those obtained from the observations (Favata et al. 2002).

Table 2.3: Best-fit parameters to the EPIC-pn simulated X-ray spectrum derived from the hydrodynamic model (shown in Fig. 2.15) and to the EPIC-pn data analyzed by Favata et al. (2002).

	Hydrodynamic model	Favata et al.
count rate (cnts/ks)	1.2	1.0
D (pc)	150	150
$N_{\rm H}$ (10^{22} cm^{-2})	1.5 ± 0.3	1.4 ± 0.4
T (10^6 K)	3.4 ± 1.2	4.0 ± 2.5
$F_{\rm X}$ (10^{-13} erg/cm^2/s)	1.4	1.3

For the light and equal-density jet models, the synthesized spectra are well

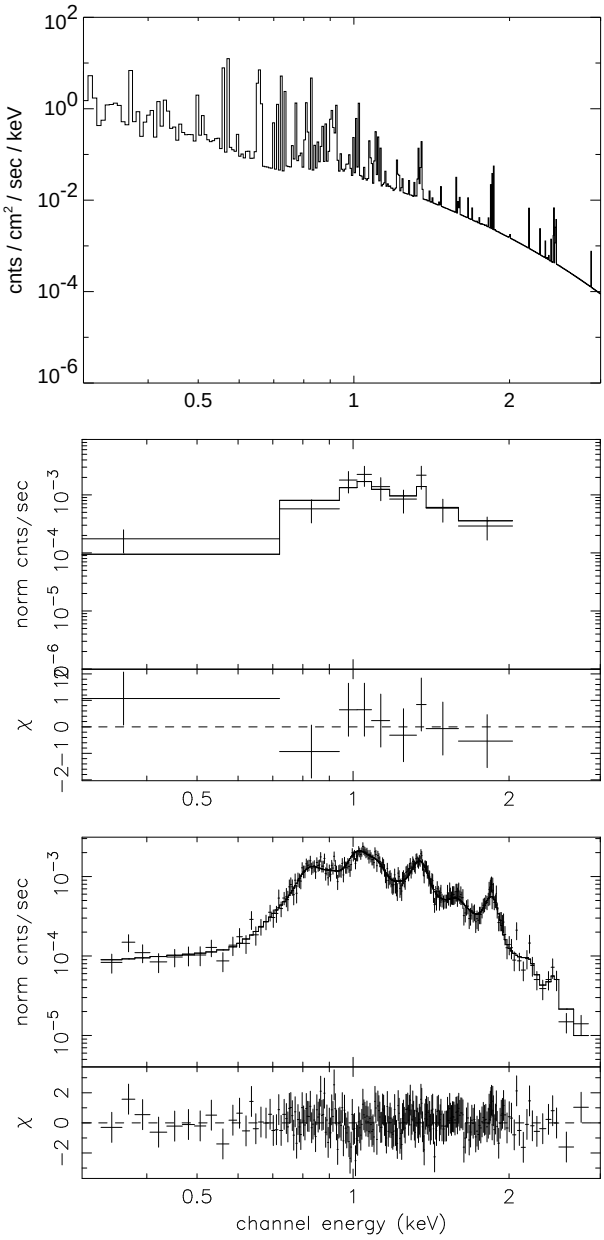

Figure 2.14: Spectra in the $[0.3, 3.0]$ keV band synthesized with the MEKAL code from the original EM(T) distributions of the whole spatial domain, 25 years since the beginning of the jet/ambient medium interaction. The top panel shows the unabsorbed parent spectrum; the middle and the bottom panels show the EPIC-pn spectra derived for two different statistics: 10^2 and 10^4 total counts respectively. For the EPIC-pn spectra each panel shows the simulated data (crosses) together with the best-fit isothermal spectrum (solid histograms) and the contribution of each bin to the total χ. The corresponding best-fit parameters are in Tab. 2.4

described by emission from an optically thin plasma at a single temperature, even in the high count statistics case. This result is due to the strong interstellar absorption which suppresses the soft emission originating from the cooler plasma

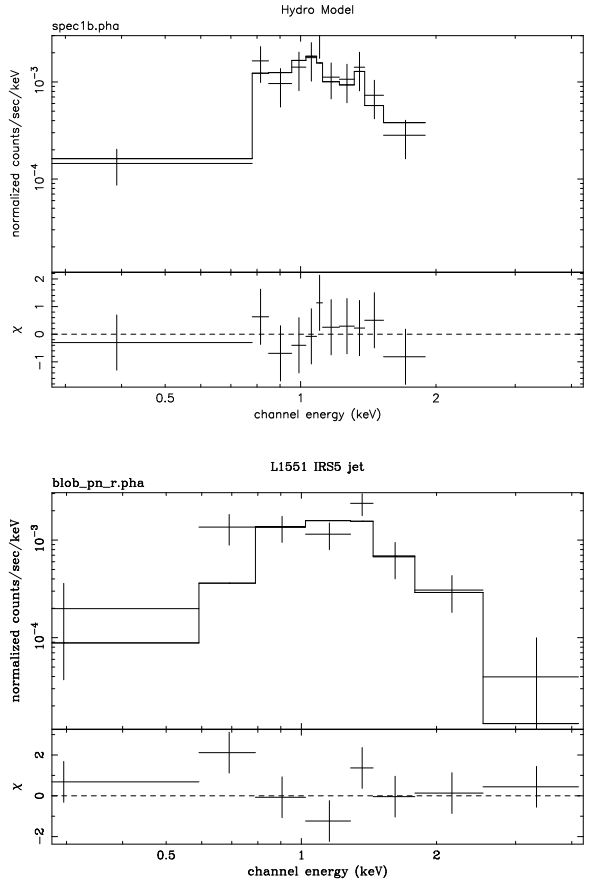

Figure 2.15: Upper panel: synthesized spectrum 25 years since the beginning of the jet-ambient interaction. The MEKAL best fitting spectrum is superimposed. Lower panel: observed EPIC-pn X-ray spectrum of the source HH 154 (Favata et al. 2002).

component in the cocoon. The best fit parameters derived from our simulations are shown in Table 2.4.

The heavy jet model which best fits HH observations shows more structured spectra than those obtained in the light jet and equal-density jet cases: in the high statistics case, the spectra are well described by a two temperature component plasma emission model, with the best fit parameters reported in Table 2.4.

The spectral analysis of course reflects the structure of the $EM(T)$ distribution: the spectra are mostly sensitive to the high temperature portion of the $EM(T)$ (see Fig. 2.12), as the softer component is suppressed by the interstellar medium absorption. On the other hand, in the heavy jet model, the $EM(T)$ distribution is characterized by a broader bump at high temperatures than is found in the other two cases (see Fig. 2.12), implying that the underlying high temperature distribution is more complex than a single temperature model.

Table 2.4: Best-fit parameters for the EPIC-pn simulated X-ray spectra obtained in the low and high statistics cases, respectively, for the three best-fit models of Table 2.2, about 20 yrs since the beginning of the jet/ambient medium interaction.

Model	counts	$N_{\rm H} \pm \Delta N_{\rm H}$ (10^{22} cm^{-2})	$T_1 \pm \Delta T_1$ (10^6 K)	$EM_1 \pm \Delta EM_1$ (10^{52} cm^{-3})	$T_2 \pm \Delta T_2$ (10^6 K)	$EM_2 \pm \Delta EM_2$ (10^{52} cm^{-3})	χ^2	Prob.[a]
Light	102	1.4 ± 0.3	2.9 ± 1.2	2.5 ± 10.9	–	–	0.44	0.88
	10317	1.39 ± 0.02	2.9 ± 0.1	2.2 ± 0.6	–	–	0.73	1.00
Equal-density	71	1.3 ± 0.4	3.1 ± 3.8	0.4 ± 3.5	–	–	0.49	0.75
	10134	1.38 ± 0.02	3.9 ± 0.2	0.33 ± 0.09	–	–	0.72	1.00
Heavy	92	1.4 ± 0.2	6.8 ± 1.7	0.9 ± 3.4	–	–	0.39	0.93
	9811	1.40 ± 0.04	3.0 ± 0.1	0.2 ± 0.2	11.8 ± 0.4	0.016 ± 0.002	0.73	0.99

[a] Null hypothesis probability.

Fig. 2.16 shows the evolution of the X-ray luminosity, $L_{\rm X}$, in the $[0.3-10]$ keV band, derived from the isothermal components fitted to the spectra in the high statistics case. I found that in the light jet case $L_{\rm X}$ varies moderately, ranging between 2 and 5×10^{29} erg/sec during the simulated 40 years time span. The $L_{\rm X}$ values is consistent with that obtained in Favata et al. (2002) ($L_{\rm X} \approx 3 \times 10^{29}$ erg/sec) and confirm the prediction of the simple analytic model proposed by Raga et al. (2002) ($L_{\rm X} \sim 2 \times 10^{29}$ erg/sec, considering the radius of the blob, $r_b \sim 30$ AU, the ambient density, $n_{\rm a} \sim 5000$ cm^{-3}, and the shock front velocity, $v_{\rm sh} \sim 500$ km s^{-1}), in which the authors assume that the X-ray emitting region corresponds to the head of the bow shock, where the gas has a temperature and density of the order of the on-axis post-shock values. Our simulations confirm that assumption, demonstrating that the X-ray emission is effectively localized in a blob just behind the shock front. A crucial feature to achieve such good agreement with Raga et al. (2002) simpler model is the strong absorption of the interstellar medium which suppresses the soft X-ray emission component originating from the cocoon with temperature at slightly less than 10^6 K. The absorption is also essential to fit the HH 154 observations. In the equal-density jet case, $L_{\rm X}$ ranges between 7.4×10^{28} and 2.7×10^{29} erg s^{-1}, in general below the luminosity observed in HH 154, although its values are consistent with those detected in other HH objects (see Table 1.1). On the other hand, in the heavy jet case, the $L_{\rm X}$ values (crosses in Fig. 2.16) are at least one order of magnitude lower than those observed so far in HH objects (Table 1.1), and in HH 154 in particular.

2.3.5 Varying the jet density parameter

As an extension of the exploration of the parameter space, I have varied the value of the initial jet density, $n_{\rm j}$, which has so far been fixed to the value derived by Fridlund & Liseau (1998) for HH 154 (namely $n_{\rm j} = 500$ cm^{-3}). In particular, I performed numerical simulations of a jet with initial density $n_{\rm j} = 5000$ cm^{-3} (ten times denser than the ambient medium, $\nu = 0.1$) and Mach number $\mathcal{M} = 20$, corresponding to an initial jet velocity $v_{\rm j} \approx 950$ km/s. I found that this model is thermally unstable since the size of the X-ray emitting region at the head of the jet is larger than the corresponding characteristic Field length. As a consequence, the X-ray luminosity drops over 2 orders of magnitude (starting initially from $\approx 3 \times 10^{29}$ erg/s) in about 10 years.

Higher values of the X-ray emission could be obtained in cases with: 1) higher initial jet density, $n_{\rm j}$; 2) higher ambient medium-to-jet density contrast, ν; 3) higher initial jet velocity, $v_{\rm j}$.

To account for the first option (higher $n_{\rm j}$), I performed the same numerical simulation discussed above, but with an initial jet density 10 times greater, namely $n_{\rm j} = 5 \times 10^4$ cm^{-3}. In this case, I derived a shock front velocity ≈ 800

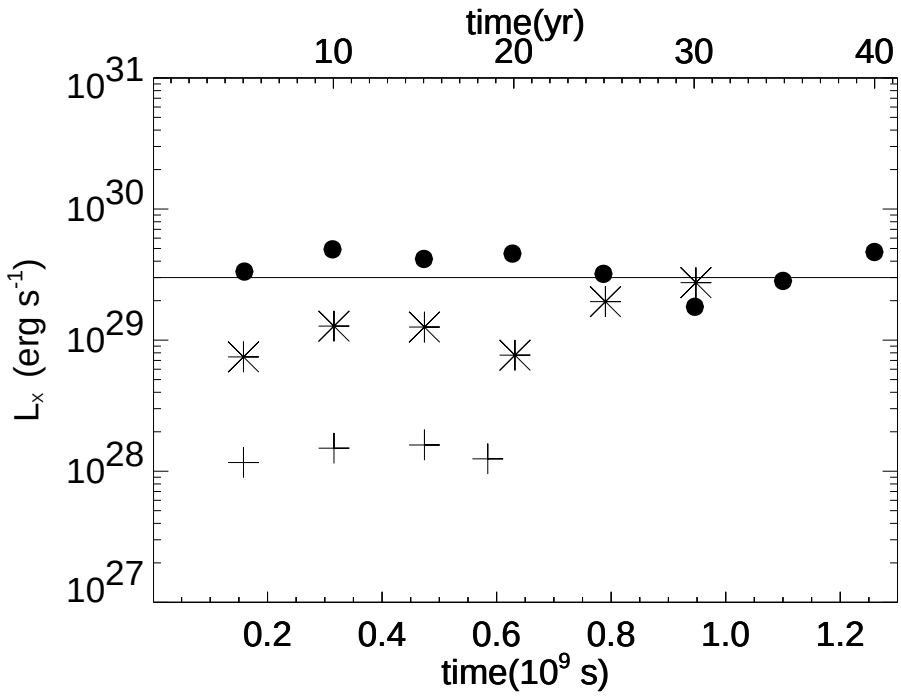

Figure 2.16: X-ray luminosity evolution as a function of time. Dots mark the light jet case, stars the equal-density jet, and crosses the heavy jet case. The line superimposed on this figure marks $L_{\rm X} = 3 \times 10^{29}$ erg s^{-1}, the value observed in HH 154 (Favata et al. 2002).

km/s and an X-ray luminosity ranging between 3 and 30×10^{29} erg/s and emission consistent with HH observation in general, but too high to reproduce the observations of HH 154. Such initial jet density values turn out to be much higher than those derived from observations of HH objects. Podio et al. (2006) studied several HH objects, and derived principal physical properties such as their density; in particular, they found that the density ranges between 400 and 1000 cm^{-3} (see also Fridlund & Liseau 1998 for density values in HH 154).

Finally, as far as the second and third options discussed above are concerned, I expect (based on our exploration of the parameter space, Fig. 2.7) that for a fixed initial jet velocity, the X-ray luminosity will increase with increasing ν and vice versa. Again, I conclude that the jet must be less dense than the ambient medium and/or the jet's initial velocity must be higher than 950 km/s. Once again, our analysis leads to the conclusion that X-ray emission originating from protostellar jets (in particular, from HH 154) is better reproduced by light jets with an initial jet density $n_{\rm j} = 500$ cm^{-3}.

2.4 Discussion and conclusions

In this chapter I have shown our numerical simulations of the interaction between a protostellar jet and the ambient medium from which I derived many interesting features of the X-ray emission due to the formation of shocks at the interaction front between the jet and the ambient medium. Our model explains the X-ray emission observed in protostellar jets as emission from mechanical heating due to shocks produced by the interaction between the jet and the ambient medium.

Our simulations reproduce in a natural way, without any ad hoc assumption, the X-ray emission observed in HH 154 (Favata et al. 2002).

In Bonito et al. (2004), I have shown the feasibility of the physical principle on which our model is based: a supersonic protostellar jet leads to X-ray emission from the shock, formed at the interaction front with the surrounding gas, consistent with the observations in the particular case of HH 154, the nearest and best studied X-ray emitting protostellar jet. Here I have performed an extensive exploration of a broad region of the parameter space that describes the interaction of the jet/ambient medium system, the parameter space defined by the jet Mach number, $\mathcal{M}$, and the ambient medium-to-jet density contrast, ν (Fig. 2.7). These results therefore allow us to study and diagnose the physical properties of protostellar jets over a broader range of physical conditions than that defined by HH 154; and thereby our extensive exploration of the parameter space improves and extends the previous work by allowing us to constrain the main protostellar jets parameters in order to obtain X-ray emission, best fit temperature and shock front speed consistent with experimental data. One of the main results of our analysis is that only a narrow range of parameters can reproduce observations. The ranges of the control parameters which significantly influence the jet/ambient medium evolution are shown in Table 2.1. From a comparison with observed quantities (also shown in Table 2.1, according to Bally & Reipurth 2002) I conclude that the parameters used in our models are consistent with observed values. Note however that the values of initial jet velocity are higher than the observed values. This apparent discrepancy is due to the fact that observers measure the velocity of the knots which have already been slowed down by the interaction with the ambient medium. Hence, I need a higher initial jet velocity to account for these currently observed speed values at the working surface. In the best light jet case, I derive a kinetic power $L_{\rm mech} \approx 0.3\ L_\odot$, more than 2 orders of magnitude lower than the observed bolometric luminosity of HH 154, $L_{bol} \approx 40\ L_\odot$ (see Table 1.1). Thus, the jet velocity values used in our simulations lead to reasonable small kinetic power. Furthermore, comparing the X-ray luminosity derived in the best light jet model here discussed, I deduce that only a small fraction of the kinetic power is converted into X-ray emission: $L_X/L_{\rm mech} \approx (8 \times 10^{-5}\ L_\odot)/(0.3\ L_\odot) = 3 \times 10^{-4}$.

After these preliminaries, I can now proceed to summarize our main findings:

- *Light jet* ($\nu > \mathbf{1}$).
  The light jet cases which reproduce the X-ray emission and optical proper motion observed are those with initial Mach number $\mathcal{M} \geq 300$ and ambient medium-to-jet density contrast $10 \leq \nu < 100$. For Mach numbers lower than $\mathcal{M} = 300$, the X-ray luminosity derived from our simulations is lower than the minimum value observed in protostellar jets ($(L_{\rm X})_{\rm obs} > 10^{28}$ erg s^{-1}) and, in some cases, shows transient behaviour due to thermal instabilities. The values $\mathcal{M} = 300$ and $\nu = 10$ provide the best case which reproduces the HH 154 observations in terms of best fit temperature, emission measure and X-ray luminosity. We also predict a substantial proper motion.

- *Equal-density jet* ($\nu = \mathbf{1}$).
  The three equal-density jet cases analyzed allow us to constrain the initial Mach number of an equal-density protostellar jet to reproduce observations: $30 < M < 300$. From the equal-density model with $\mathcal{M} = 100$ I derive shock front velocities and X-ray luminosities consistent with HH objects observations in general (see Table 1.1).

- *Heavy jet* ($\nu < \mathbf{1}$).
  In order to reproduce some characteristics of the observations in the heavy jet scenario, I require an initial jet Mach number $\mathcal{M} \approx 30$ and an initial jet density much higher than the ambient density, $\nu \leq 0.03$, i.e., a jet 30 times denser than the ambient medium or more. Lower initial Mach number in some cases leads to thermal instability, which in turn suppress X-ray emission about 5 years after the beginning of the interaction between the protostellar jet and the ambient medium. For a jet 30 times denser than the ambient medium ($\nu = 0.03$) and with initial Mach number $\mathcal{M} = 30$, I predict emission from a million degree plasma. Although its $v_{\rm sh}$ is too high and its $L_{\rm X}$ is too low with respect to those observed in HH objects in general (see Tab. 1.1) and in HH 154 in particular (Favata et al. 2002), I cannot reject the possibility of new more sensitive observations which may show fainter emission not yet detected in X-ray emitting HH objects.

Here I discussed light, heavy and equal-density jet models that are in best agreement with experimental results from HH objects in general: a light jet with $\mathcal{M} = 300$ and $\nu = 10$; an equal-density jet with $\mathcal{M} = 100$ and $\nu = 1$; and a heavy jet with $\mathcal{M} = 30$ and $\nu = 0.03$. For each case, I analyzed the evolution of the mass density and temperature spatial distributions derived from our model, the shock front proper motion and its spectral properties, the X-ray emission and its stability. In each best-fit model, the interaction between the supersonic protostellar jet and the unperturbed ambient medium leads to the formation of a

hot and dense cocoon surrounding the jet and smoothed by thermal conduction. Just behind the shock front, there is a hot and dense blob from which the harder, bright X-ray emission originates: the strong interstellar absorption suppresses the softer component due to the cocoon. In all cases examined, the X-ray emitting region is thermally stable, i.e., thermal conduction prevent the collapse of the source due to radiative cooling; furthermore, this X-ray emitting region should show a detectable proper motion.

To compare our findings with HH 154 observations, I have rejected equal-density and heavy jet cases that show a too large shock front velocity ($v_{\rm sh} \approx 600$ km s^{-1} and ≈ 1900 km s^{-1}, respectively) and too small X-ray luminosity ($L_{\rm X} \approx 10^{29}$ erg s^{-1} and $\approx 10^{28}$ erg s^{-1}), all judged with respect to the $v_{\rm sh}$ and $L_{\rm X}$ values observed in HH 154 ($v_{\rm sh} \approx 500$ km s^{-1} and $L_{\rm X} = 3 \times 10^{29}$ erg s^{-1}).

In the best light jet case, I derive a particle density $n \approx 6500$ cm^{-3} and a velocity $v_{sh} \approx 500$ km s^{-1} for the X-ray emitting region, leading to a momentum $mv = 2 \times 10^{-6}$ $M_\odot$ km s^{-1}. This value is consistent with the upper limit 7×10^{-4} $M_\odot$ km s^{-1} obtained for HH 154 (Fridlund & Liseau 1998). This leads to the conclusion that the protostellar jet cannot drive the molecular outflow, whose momentum has been estimated to be between 0.15 and 1.5 $M_\odot$ km s^{-1} (Fridlund & Liseau 1998). This conclusion is based on the relations for the jet mass loss rate and the mechanical luminosity, given by

$$\dot{M} = 1.8 \times 10^{-9} \frac{M_\odot}{yr} \times \\ \times \left(\frac{r_{\rm j}}{5 \times 10^{14} cm}\right)^2 \left(\frac{n_{\rm j}}{500 cm^{-3}}\right) \left(\frac{v_{\rm j}}{1400 km/s}\right) \ , \tag{2.18}$$

$$L_{\rm mech} = 0.3 L_\odot \times \\ \times \left(\frac{r_{\rm j}}{5 \times 10^{14} cm}\right)^2 \left(\frac{n_{\rm j}}{500 cm^{-3}}\right) \left(\frac{v_{\rm j}}{1400 km/s}\right)^3 \ ; \tag{2.19}$$

these expressions allow us to conclude that the jet mass loss rate and mechanical luminosity are, respectively, 3 and 2 orders of magnitude lower than expected in CO outflows (Cabrit & Bertout 1992). This result supports the conclusion discussed by Fridlund & Liseau (1998) that the jet origin is probably different from that of the CO outflow.

I estimated the values of the momentum, mass loss rate and mechanical luminosity for each model that better reproduce the X-ray observation of HH objects shown in Table 2.2. I derived: $\dot{M} \sim 10^{-9}$ $M_\odot$/yr; $L_{\rm mech} = (0.3 - 1.7)$ $L_\odot$; $mv \lesssim 10^{-6}$ $M_\odot$ km s^{-1}. These values are several orders of magnitude lower than those observed in CO outflows (in HH 2, HH 154 and HH 80/81, Moro-Martín

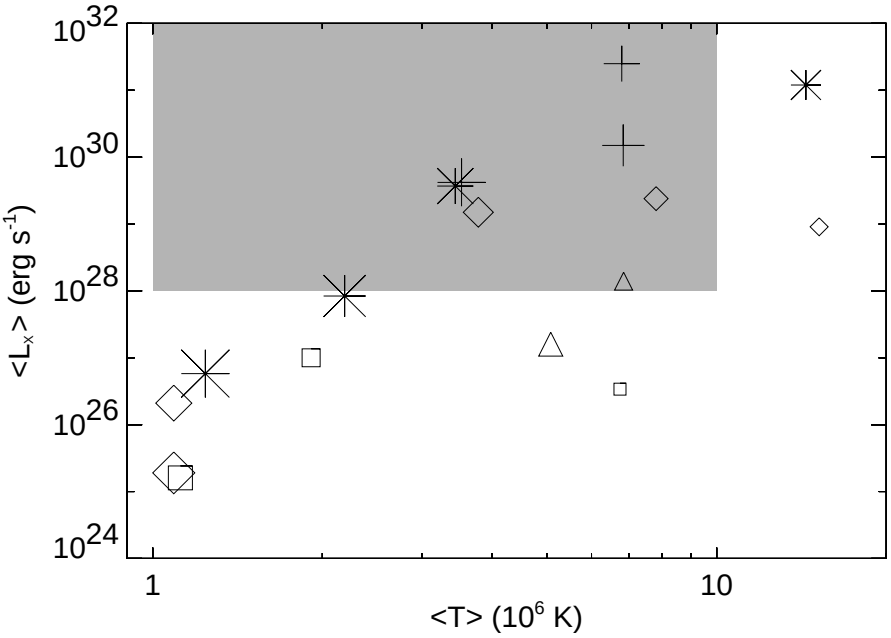

Figure 2.17: Mean value of the X-ray luminosity as a function of the mean value of the best fit temperature, derived from our model synthesized spectra. Crosses correspond to Mach number $\mathcal{M} = 1000$, stars to $\mathcal{M} = 300$, diamonds to $\mathcal{M} = 100$, triangles to $\mathcal{M} = 30$ and squares to $\mathcal{M} = 10$. The increasing size of each symbol corresponds to increasing value of the ambient medium-to-jet density contrast, $\nu = 0.01$-300. The shaded region refers to the ($L_{\rm X}$, T) values consistent with observations of HH objects in general.

et al. 1999; Fridlund & Liseau 1998; Yamashita et al. 1989). From the comparison between our results and the observations of CO outflows, I conclude that the simulated protostellar jets which best reproduce X-ray observations cannot drive molecular outflow.

On the basis of our analysis, I conclude that the light jet scenario, with a jet 10 times less dense than the ambient medium ($\nu = 10$) and with an initial jet Mach number $\mathcal{M} = 300$, with $v_{\rm sh} \approx 500$ km s^{-1} and $L_{\rm X} \approx 3 \times 10^{29}$ erg s^{-1}, is the best case to reproduce the HH 154 observations. This conclusion is also supported by the optical observations of HH 154 (Fridlund et al. 2005) from which the light jet scenario can be deduced, according to the Hartigan (1989) model.

More generally, in Fig. 2.17 I show the values of $L_{\rm X}$ vs. T derived from the spectra synthesized from our model as a function of different values of $\mathcal{M}$ and ν. Crosses mark cases with $\mathcal{M} = 1000$, stars with $\mathcal{M} = 300$, diamonds with $\mathcal{M} = 100$, triangles with $\mathcal{M} = 30$ and squares with $\mathcal{M} = 10$. Bigger symbol sizes correspond to higher values of the ambient medium-to-jet density contrast, ν, in the range 0.01 to 300, as in Fig. 2.7. The shaded zone marks the range of parameters consistent with observation (Table 1.1). We have chosen $L_{\rm X}$ one order of magnitude lower than the minimum observed so far to account for fainter sources.

For a fixed value of $\mathcal{M}$, $L_{\rm X}$ and T decrease with increasing ν and, for a fixed value of ν, $L_{\rm X}$ and T increase with increasing $\mathcal{M}$. From the figure it is possible to derive $\mathcal{M}$ and ν (the velocity and density) of the protostellar jet to be compared with observations (in terms of $L_{\rm X}$ and best fit T). Predictions about possible fainter – not yet discovered – sources can also be made.

Furthermore the results derived from the variation of the initial jet density parameter, $n_{\rm j}$, discussed in Section 2.3.5, lead to the conclusion that, even with different initial density values, a protostellar jet must be less dense than the ambient medium, and must have a high initial velocity (1000 km/s or more) in order to reproduce HH objects observations.

Our model predicts in all cases a significant proper motion of the X-ray source, with values which, in the case of HH 154 would be measurable with *Chandra*, providing a clear test of the model scenario.

As discussed by Favata, Bonito et al. (2006), a 100 ks observation was performed in 2005, showing, when compared with the 2001 observation, a more complex scenario, i.e., both a moving and a stationary source were detected in HH 154, giving the source (in 2005) a "knotty" appearance. Thus, while a traveling shock (likely based on the basic physics explored in the present work) is apparently present in HH 154, the source structure is more complex.

The comparison between our model of a continuous supersonic jet through an unperturbed surrounding medium and the new *Chandra* data, discussed in Favata, Bonito et al. (2006), shows that the model reproduces most of the physical properties observed in the X-ray emission of the protostellar jet (temperature, emission measure, etc.). At the same time, it fails to explain the complex evolving observed morphology, showing, most likely, that the jet is not continuous.

A possible scenario that will be tested in the future is based on similar physics as discussed in the present work, but in the presence of pulsating jets (instead of the constant jet inflow here examined); alternatively, it is worthwhile to consider the interactions between the jet and an inhomogeneous ambient medium, which can lead to the knotty structure observed inside the jet itself. I also plan to explore other physical mechanisms, different from the moving shock at the tip of a supersonic jet, stimulated by the above mentioned *Chandra* observations of HH 154, such as steady shocks formed at the mouth of a de Laval nozzle. New observations of the evolution of HH 154 will however be necessary in order to understand the phenomenon and to further constrain the model scenario.

The constant jet inflow model discussed here is a useful and necessary building block towards more complex (e.g., with a discontinuous time profile) models. The X-ray emission from a pulsed jet, for example, will still take place at the shock front, and will thus be based on the same physical effects and principles as observed in a constant inflow jet. Our (simpler) constant inflow jet model is a very useful tool to infer the right parameter values to use in future, more complex

models needed to also reproduce the observed morphology: using our constant inflow jet model results, shown in Fig. 2.7 and in Fig. 2.17, it is possible to derive the initial jet velocity and ambient medium-to-jet density ratio needed for the new bullets to produce a X-ray luminosity and best fit temperature consistent with observations.

A limitation of our hydrodynamic model is the hypothesis of pressure balance between the jet and the ambient medium, in order to obtain the observed jet collimation. Most models of jet collimation suggest the presence of an organized ambient magnetic field which is known to be effective in collimating the plasma. As a follow-up of our analysis, I am developing an MHD model of protostellar jets that will allow us to relax the assumption of an initial pressure equilibrium. The comparison of the MHD model results with the X-ray observations will provide a fundamental tool to investigate the role of the magnetic field on the protostellar jet dynamics and emission.

Bally et al. (2003) proposed that the X-ray emission may be due to X-rays scattered from the protostellar coronae itself (see Fig. 2.3); such a mechanism, causing X-ray coming from the initial jet collimation, would show no proper motion. Our model unambiguously predicts a detectable proper motion of the X-ray source. In order to discriminate among the various proposed models, I proposed a new *Chandra* observation (approved in AO6 and described in Chapter 3) of HH 154 which will allow us to study the X-ray emitting region and its proper motion. From the analysis of new XMM-*Newton* data, I will compare the $L_{\rm X}$ variability (if any) with that obtained from our simulations.

Chapter 3

X-ray emission and variability from protostellar jets

I describe the analysis of the Chandra observations of the X-ray emission from the nearest protostellar jet, HH 154. In particular I discuss the comparison between the 2005 Chandra observations of HH 154 and the 2001 observations of the same jet, in order to derive the proper motion, the morphology changes of the X-ray source, and the variability of its emission (see also Favata, Bonito et al. 2006).

The chapter is organized as follows: in Sect. 3.1 I present the data analysis; in Sect. 3.2 I discuss the main results derived from the Chandra observations; Sect. 3.3 presents the interpretation of observations inferred from the numerical models; in Sect. 3.4 I discuss the results and draw the conclusions.

3.1 Data analysis

The Chandra observation of the nearest X-ray emitting protostellar jet, HH 154, presented here has been performed on 27 Oct. 2005, for a total exposure time of 97 ks. The observation was centered at the position 04:31:32.9, +18:08:04.7 (using FK5[1] coordinates) and was performed with the ACIS-I camera (see Appendix B). We processed the observation using the Chandra Interactive Analysis of Observations (CIAO) package, and filtered the data to retain only photons in the 0.3 to 4.0 keV band. To allow an uniform comparison, we have also reprocessed the archived Chandra observation collected on 23 July 2001 (described by

[1]The Catalogue of Fundamental Stars is a series of six astrometric catalogues of high precision positional data for a small selection of stars to define a celestial reference frame, which is a standard coordinate system for correlation of star positions. Fourth Fundamental Catalogue (FK4) was measured and published in 1963 to contain 1535 stars in various equinoxes from 1950.0 to 1975.0. Fifth Fundamental Catalogue (FK5) was an update of FK4 in 1988 with new positions for the 1535 stars. It was obsoleted when the quasar based International Celestial Reference Frame (ICRF) was introduced.

Bally et al. 2003) using the same approach. Individual X-ray sources have been detected using the standard wavelet-based algorithm of CIAO. A small positional shift is present between the two observations, as shown by both the stellar and the extragalactic X-ray sources in the field. To allow detection of the expected small proper motion of the jet X-ray source, we have registered the two images by applying a shift determined by minimizing the coordinate differences of the 7 brightest X-ray sources in the field which are also members of L1551 (to minimize the effects of proper motion). The shift between the two observations is (2.43 ± 0.28) arcsec, a value within the absolute attitude reconstruction accuracy expected for Chandra.

3.2 Results

A powerful diagnostic that can discriminate among the various proposed models, and in particular validate (or falsify) our detailed hydrodynamic moving shock model (discussed in Chapter 2; see also Bonito et al. 2007), is the proper motion of the X-ray source. My model unambiguously predicts a measurable (with Chandra) proper motion for the X-ray source, while mechanisms associated with the reflection of the protostellar X-ray flux or with shocks of the wind on the "walls" of the jet cavity (as discussed by Bally et al. 2003) will show no proper motion.

The Chandra observation of HH 154 allows the proper motion of the shocked material to be accurately determined, strongly constraining the emission mechanism.

The X-ray luminosity of HH 154 has varied by a factor of a few between the XMM-Newton (0.84 cnts/ks) and the Chandra (0.77 cnts/ks) observations; this long-term variability by itself is not a strong diagnostic of the emission process, as the (proto-)stellar X-ray luminosity is known to vary typically by such factors. At the same time, the optical and UV emission in high-excitation lines from the jet itself has a similar long-term variability, as individual clumps of material travel along the jet, are shocked and then cool. Hence, the observed X-ray variability is compatible with different emission mechanisms.

An important result of our 2005 Chandra data of HH 154 (Favata, Bonito et al. 2006) is that the observed X-ray morphology of HH 154 is more complex than expected (Fig. 3.1). A detailed comparison between our 2005 Chandra observation (Favata, Bonito et al. 2006) and the previous 2001 Chandra data (Bally et al. 2003) shows that most likely the source consists of both an unresolved, point-like component, without detectable proper motion over 4 yr, and an elongated component.

This result is shown in Fig. 3.1, where both the 2001 (left panel) and the

2005 (right panel) Chandra observations of HH 154 are presented. The position of the protostar from which the jet originates (L1551 IRS5) is superimposed on the figure, from the VLA observations of Rodríguez et al. (2003b).

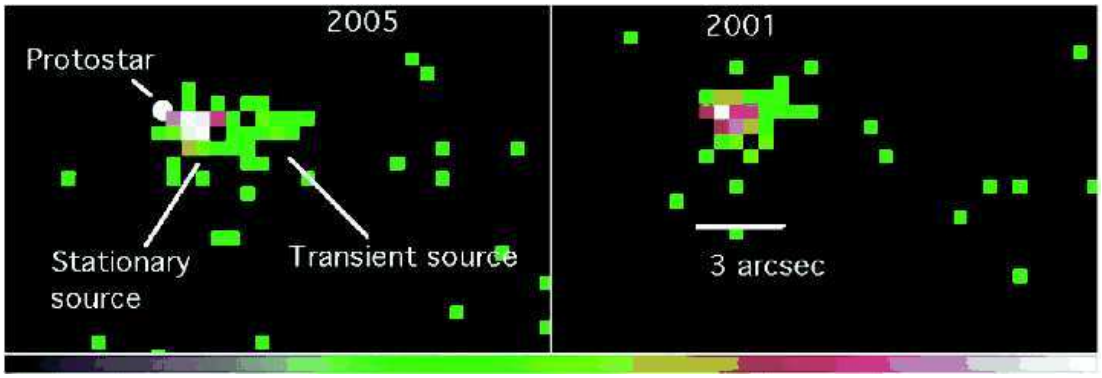

Figure 3.1: The X-ray source associated with the HH 154 jet, in the 2005 (left panel) and 2001 (right panel) Chandra observations. The small white circle in the 2005 observation shows the position of the protostar driving the jet (L1551 IRS5, at 04:31:34.2 +18:08:05). The scale of the image is 0.5 arcsec/pixel, north is up, east left. While a hint of an extended component is already present in the 2001 data (as discussed by Bally et al. 2003), the 2005 observation shows that a better representation is in terms of two components, a point-like source which has the same position as in 2001, and an expanding component which moved, in the jet's direction and away from the driving star, by approximately 2 arcsec between 2001 and 2005. The color scale is the same for both observations.

Bally et al. (2003) had suggested that the jet X-ray source might be extended even in the 2001 observations; in our 2005 observation not only do we confirm that the source indeed has an extended component, but we also show that the morphology has changed, with the size of the extended component clearly increasing with respect to 2001. While the unresolved component does not show a detectable motion with respect to 2001, the extended component has clearly become more elongated along the jet's direction, and shows an expansion in agreement with a shock moving away from the parent star.

The extended nature of the source in the 2005 observation is confirmed in Fig. 3.2, where we performed a Gaussian smoothing of the data, using the software tool csmooth available in the CIAO software. This figure shows the source associated with HH154 to be elongated in 2005 (left panel), while in 2001 (Fig. 3.2, right panel) the same source was compatible with being point-like.

Between the 2001 and 2005 observations the source extent has increased by 2 arcsec, which, at the distance of L1551 ($D \approx 150$ pc), correspond to 4.5×10^{15} cm, or 300 AU. This results in a projected velocity of ca. 330 km s^{-1}, and, assuming the inclination of the jet to be 45 deg (Liseau et al. 2005), this implies a shock velocity of ca. 460 km s^{-1}, or about 100 AU/yr, in good agreement with the model's prediction discussed in Chapter 2 (see also Bonito et al. 2004, 2007).

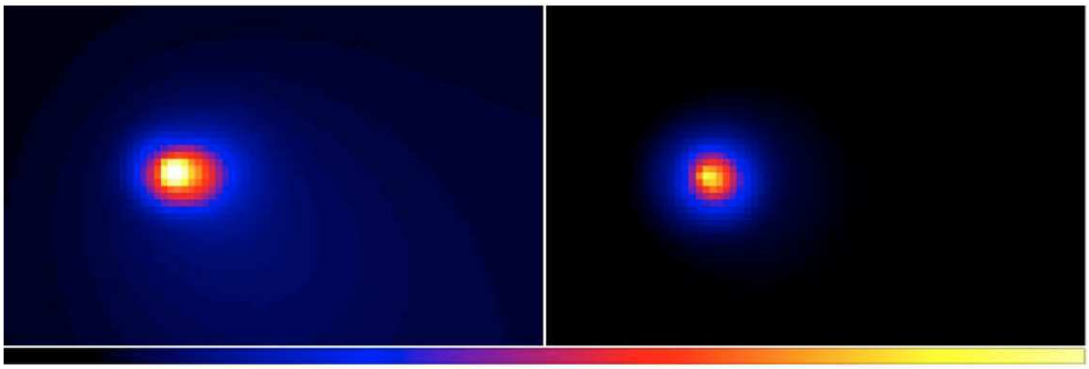

Figure 3.2: The smoothed image of the X-ray sources associated with HH 154 are shown, in the left panel for the 2005 data and in the right panel for the 2001 data. The 2005 data show the presence of an elongated component not present in the 2001 data.

Figure 3.3 shows a horizontal cut through the 2005 Chandra HH154 image (Fig. 3.1, left panel), obtained by adding the number of photons in the two rows where the stationary source peaks. This figure shows the relative intensity of the stationary and the moving components.

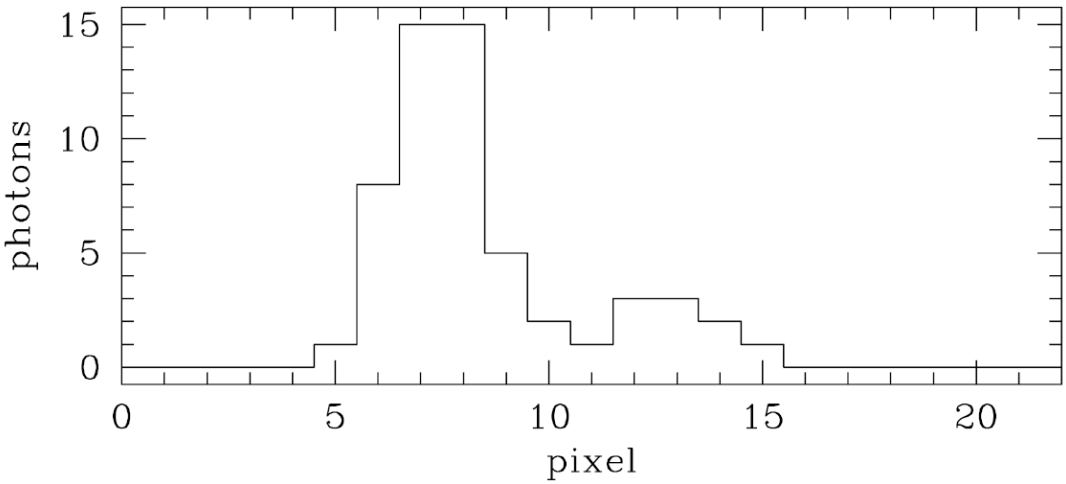

Figure 3.3: A horizontal cut through the 2005 Chandra HH 154 image, obtained by adding the number of photons in the two rows where the stationary source peaks. The profile shows the relative intensity of the stationary (left peak) and the moving (right peak) components.

We derived the spectral properties of the X-ray source detected in HH 154 with Chandra in our 2005 observations. A spectral analysis of the source's emission, have shown that it can be fitted with a simple absorbed thermal plasma (apec model in XSPEC), resulting in a temperature of approximately 0.5 keV and a column density of 1.5×10^{22} cm^{-2}, essentially consistent with previous spectral analysis of the X-ray source detected with XMM-Newton in 2000 (Favata et al. 2002). These results are also compatible with the Chandra 2001 observation,

showing limited spectral variability in the source, even in the presence of significant morphological evolution. These results describe the spectral properties of the X-ray source as a whole, the number of X-ray photons present in the moving component of the source being too small to attempt a separate spectral analysis (see Fig. 3.3).

It would be very useful to obtain new deeper Chandra observations (with exposure time of about 400 ks or even more) in order to discriminate between the spectral contribution due to the point-like stationary source and the elongated component, so as to perform the very first spatially resolved spectral analysis of X-ray emission from protostellar jets.

3.3 Implications on hydrodynamic modeling

The scenario I proposed in Chapter 2 (Bonito et al. 2004, 2007), which the observation discussed here was designed to test, made clear predictions about the evolution of the X-ray emission due to the jet's shock. In particular, the model which best reproduced HH154's X-ray luminosity and spectrum predicted that the X-ray source was point-like, located at the head of the jet and had a continuous motion of about 500 km s^{-1} (see Chapter 2). The observational results discussed here are more complex than expected: the X-ray source displays both an apparently point-like component, without detectable motion, and a probably extended component is moving at about 500 km s^{-1}, a value very close to the value predicted by the Bonito et al. (2004, 2007) model. However, the apparently stationary component is not in agreement with the simple Bonito et al. (2004, 2007) model. The assumptions behind this model were simple, aiming at elucidating the basic physics. In particular, the jet is assumed to be continuously powered, with constant density of inflowing material, and the ambient medium through which the jet propagates is assumed to be uniform. Both these two assumptions are likely to be oversimplification. The optical observations of HH154 in the last two decades show evidence of the jet being highly inhomogeneous, with density varying by some two orders of magnitude within the jet itself (Fridlund et al. 2005), so that the jet is likely to be driven in an eruptive, rather than continuous, form, with new visible features appearing on a time scale of few years. Evidence for the jet to be pulsed, rather than continuous, comes also from the decreasing velocity of individual blobs through the jet: while the de-projected velocity from optical spectroscopy is up to 600 km s^{-1} close to the star, at 3 arcsec from it, it begins to drop, decreasing to 160 km s^{-1} for the working surface which is located at some 15 arcsec from the star in the 2005 observations - see Fridlund et al. (2005) for details. In the presence of a continuous driving of the jet, the shock front should to travel at constant velocity all the way to 15 arcsec; the observed

velocity decrease is thus likely showing a significant pulsating component. At the same time, the assumption of a homogeneous medium through which the jet propagates is unlikely to be correct: the high level of structuring of the medium is shown for example by the fast varying circumstellar absorption (the driving star being hidden by some 150 mag of material, while the jet has less than 10 mag of absorption). Even along the jet optical observations show the absorption to vary between 2 and at least 6 mag (Fridlund et al. 2005). Although the predictions of the simple model of a continuous jet ramming into a homogeneous medium of Bonito et al. (2004, 2007) is not compatible with these observational results, the high level of structuring in both the jet and the medium can possibly explain the phenomenology observed in X-rays, with the same basic physics on which the simple models are based. The density of circumstellar material is very likely to decrease significantly with distance from the jet-driving source (as observed in the structure of the absorbing material), and thus the individual jet pulses (or "bullets") will initially meet a dense medium, and then later propagate through a thinner medium. Bonito et al. (2007) have carried out, building on the approach first used by Bonito et al. (2004), an extensive exploration of the parameter space of both density contrast and velocity for a uniform, constantly driven jet. One result is that the X-ray luminosity of the shock front depends on both the density contrast and the Mach number with which the jet plows through the medium. In the presence of a decreasing ambient density and increasing temperature (due to pressure equilibrium), the jet's luminosity will decrease as it plows though the medium. In addition, in the case of an isolated traveling plasma bullet, the temperature of the X-ray emitting plasma is expected to gradually decrease due to radiative and conductive losses. One possible scenario explaining the observed phenomenology is therefore that the driving source is continuously injecting fresh blobs of material into the jet. As each blob rams into the high density medium near the star it will cause the X-ray emission seen as the stationary X-ray source closer to the protostar. As a given blob plows through the high density medium and starts to move through the thinner medium farther away from the star, its X-ray luminosity will decrease while it moves away, forming the fainter moving X-ray source well evident in our 2005 Chandra observation. This scenario is of course schematic, and it will require detailed modeling before it can be tested in detail (see Chapter 5). It is however supported by optical (Fridlund & Liseau 1994) and radio Rodríguez et al. (2003b) observations of new blobs appearing repeatedly from behind the obscured region every few years. Fig. 3.4 (Neckel & Staude 1987) shows that a new knot, named knot F, which is not visible in 1983, appears in the 1985 data.

The basic characteristics of our scenario are based on the detailed study of the simple, homogeneous jets studied by Bonito et al. (2007) and rely on the same physics. Proper testing of the scenario (a pulsed jet in a non-homogeneous

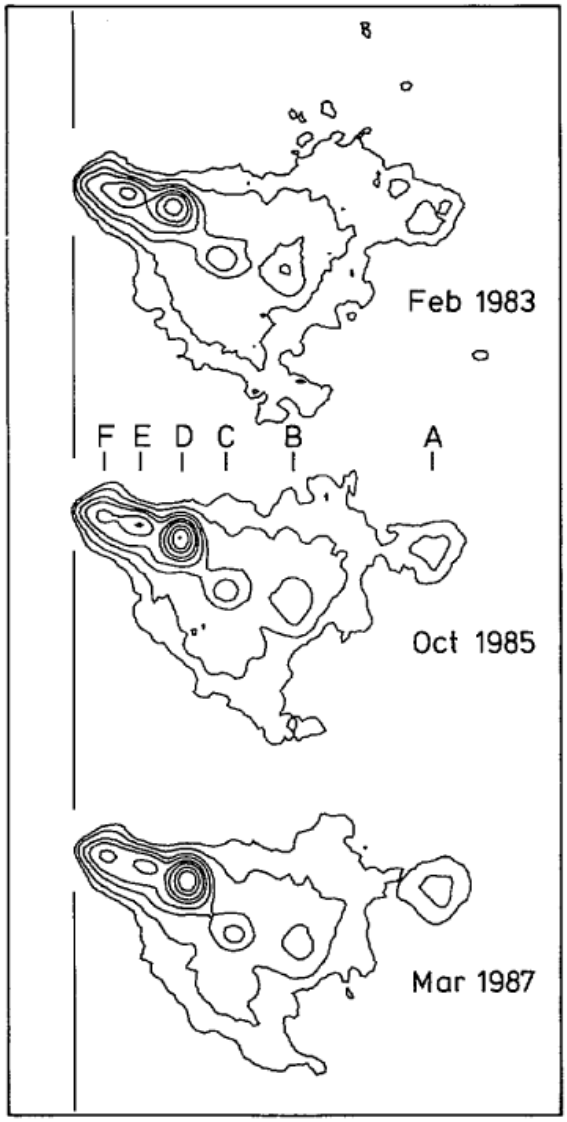

Figure 3.4: The IRS5 jet image at three epochs. The new knot, F, appears in the 1985 data (Neckel & Staude 1987).

circumstellar medium) will also require more sensitive X-ray observations, with sufficient statistics as to allow a determination of the spectrum of the moving component (the one plowing through the thinning circumstellar medium), whose temperature is expected to decrease with distance from the star.

3.4 Discussion

The Chandra 2005 observation discussed here was designed to provide a clear test of whether the X-ray emission from HH154 is due to moving shocks (Bonito et al. 2004, 2007, discussed in Chapter 2) rather than stationary mechanisms such as

scattered stellar X-rays (Bally et al. 2003, discussed in Sect. 3.2). The observed X-ray morphology is more complex than what would be observed in the presence of a continuously driven jet propagating through a uniform medium. This is not surprising given the evidence from optical observation of a pulsating jet driven by an eruptive process, and the observed non homogeneous distribution of absorbing material in the region surrounding the jet. Detailed study and modeling of a number of scenarios along the above lines will be needed to determine in detail which conditions can reproduce the observed morphology. While this work is ongoing (see Chapter 5), simple considerations based on our current models of uniform jets lead us to propose that the most likely scenario explaining the observations is one of an eruptive jet propagating within a medium with strong density gradients. In addition to the (already ongoing) detailed modeling, new, more sensitive X-ray observations will be needed in the future, for example to determine the temperature of the plasma associated with the moving X-ray source, to ascertain whether this is, as expected in such a model, lower than the X-ray temperature associated with the stationary component. These measurement would also provide a direct determination of the scale of density changes in the circumstellar medium around the star, providing an unique probe of such material. Also, they will provide an unique probe of the high energy phenomena at the base of the jet, close to the launch site, constraining the physics of the jet formation.

Any further understanding of the complex nature of the mechanism producing X-rays in HH154 will require an understanding of the evolution of its morphology. We therefore need new observation, also of 100 ks duration (the same as the 2001 and 2005 observations), to provide a clear answer to a number of key questions: is the velocity of the transient source observed in 2005 moving away from the source decreasing? Is the stationary source constant? A "third epoch" observation is necessary to monitor its X-ray luminosity: is the moving plasma bullet fading? Is it cooling? If so, this would allow to constrain the timescale for its radiative cooling, and thus (in a fully in- dependent way) its density. Finally, we will also be able to ascertain whether the stronger, apparently stationary source is indeed not moving, rather than moving more slowly and thus requiring a longer time base for its motion to be detected.

Chapter 4

Optical observations of HH 154

The discovery of X-ray emission from the basis of the HH 154 protostellar jet and the first ever measurement of the proper motion of the X-ray source itself (Favata, Bonito et al. 2006), as predicted by the numerical model discussed in Chapter 2 (see also Bonito et al. 2004, 2007), encourage us to investigate the multi wavelength behaviour of the structures within the jet. To this and we proposed a joint Chandra/HST observations of the HH 154 jet in 2005 (AO6). New optical observations (together with the previous 1996 and 1998 HST observations of the same jet) can provide a relation between the X-ray emission observed and the morphological changes in the inner part of the jet, allowing us to discriminate between different models developed to explain the X-ray emission mechanism. We are observing the "live" evolution of a binary low-mass protostellar jet system, at a spatial resolution equivalent with the best hydrodynamic codes (see also Chapter 2). The evolution of the inner part of the jet is very important to study as this part is associated with the moving and stationary X-ray sources detected from HH 154 (see Chapter 3 and Favata, Bonito et al. 2006). Fig. 4.1 shows the HH 154 jet as observed with HST in the H_α filter in 1996 (lower panel) with all the SIMBAD[1] database objects (marked in the upper panel) superimposed.

I performed the reduction of these optical data (1996, 1998 and 2005 HST observations) at the European Space Agency (ESA)-ESTEC in Noordwijk (The Netherland) in the framework of a scientific collaboration with Dr. Fabio Favata and Dr. Malcolm Fridlund (July 2005, April 2006, July 2007).

In this Chapter I present the main results derived by the analysis of the multi-epochs optical observations of the HH 154 jet. In particular I derive the proper motion of each sub-structure within the jet (the so-called "knots"), their energetics and dynamics.

The Chapter is organized as follows: in Sect. 4.1 I present the technical details concerning the observations and the performed data reduction; in Sect.

[1]The SIMBAD astronomical database provides basic data, cross-identifications, bibliography and measurements for astronomical objects outside the solar system.

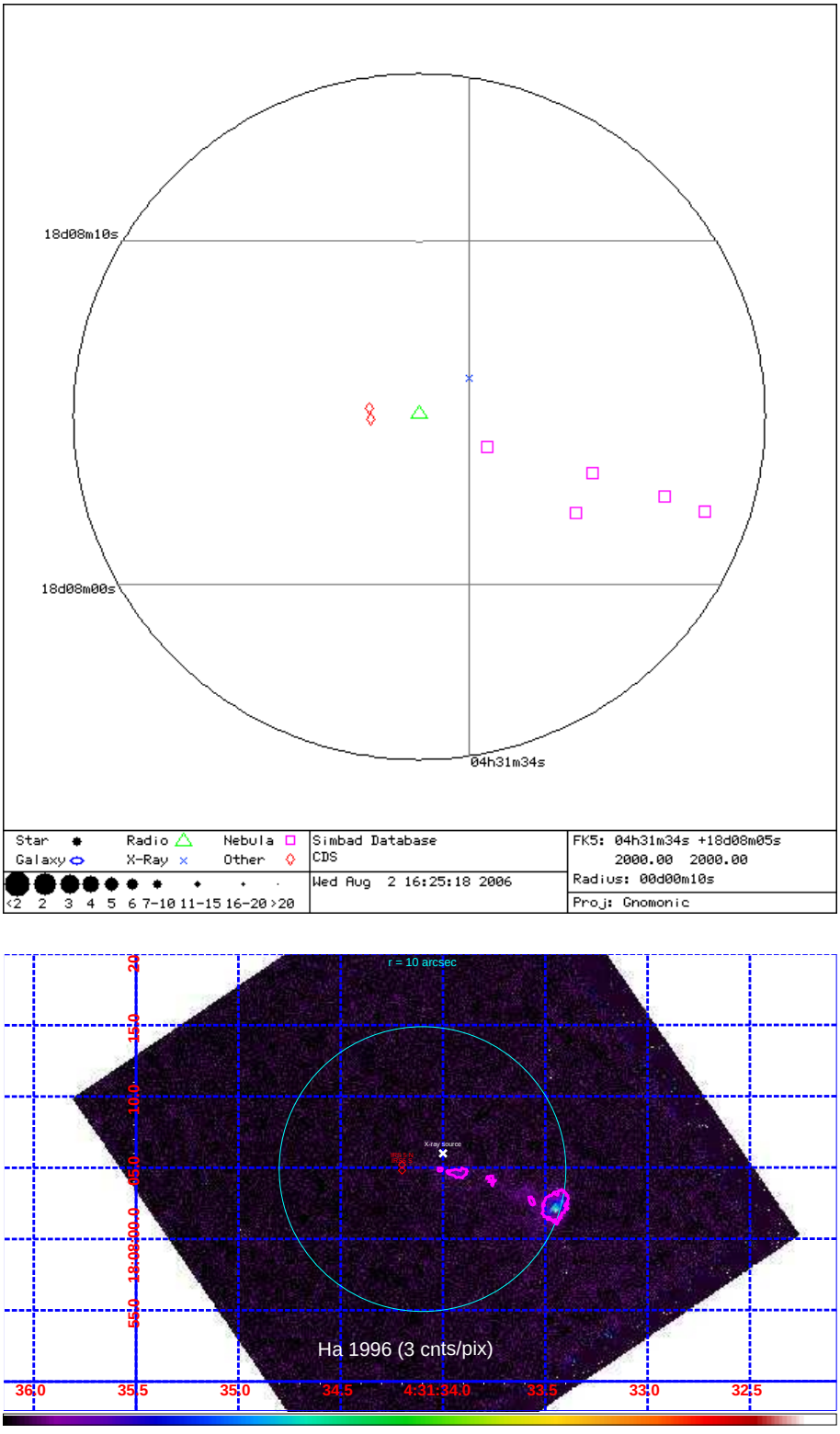

Figure 4.1: HH 154 jet as observed with HST (lower panel) with all the SIMBAD database objects (upper panel) superimposed on the figure.

4.2 I discuss the main results on morphological changes, shock structure, proper motion and flux variation of the knots within the jet and of the jet as a whole; I will draw my conclusions in Sect. 4.3.

4.1 Observations and data reductions

4.1.1 HST/WFPC2 observations

The region centered on L1551 IRS5 jet has been imaged using the Wide Field and Planetary Camera 2 (WFPC2) on board of the *Hubble Space Telescope*. The main characteristics of this instrument are presented in details in Appendix C. Here I show just few properties. This camera consists of 4 adjacent 800 × 800 pixels CCD. Of these, the WF2-4 has a plate scale corresponding to 0.0996"/pix, while the PC1 chip has a better resolution, corresponding to 0.0455"/pix. As in the case of our previous 1996 and 1998 observations, (Fridlund et al. 2005, FL05), we centered the jet (whose total length is currently $\lesssim''15$) in the PC camera, using an orientation of the WFPC2 camera allowing the registration of the only observable star (VSS 4, Vrba et al. 1976) within the WFPC2 field-of-view, on the WF4 chip. Fig. 4.2 shows the mosaic of the four cameras in the H_α filter in 2005. The HH 154 jet is well visible in the PC1 camera, the VSS 4 star in the WF4 camera. In the other two cameras (WF2 and 3) few faint knots are detectable.

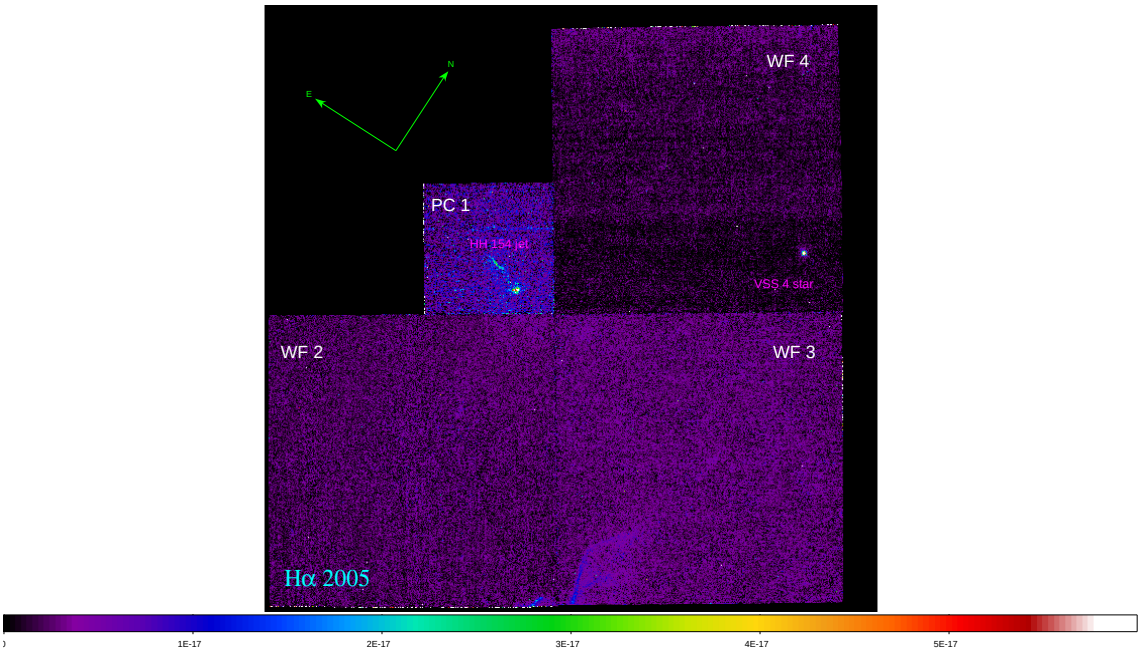

Figure 4.2: Hubble Space Telescope WFPC2 image of the mosaic of the 4 cameras (PC1, WF2, WF3 and WF4) in the H_α filter in 2005. The HH 154 jet and the only one star within the field-of-view of the instrument (VSS 4) are labeled on the figure (Bonito et al. 2008).

Table 4.1: Information about the data in 1996, 1998, and 2005 in both filters.

obs. ID	date	exposure time (s)	filter
u31f0107t	1996 Feb 03	1300	[SII]
u31f0108t	1996 Feb 03	1200	[SII]
u31f0109t	1996 Feb 03	1300	H_α
u31f010at	1996 Feb 03	1200	H_α
u3nj0101r	1998 Mar 15	1300	[SII]
u3nj0102r	1998 Mar 15	1300	[SII]
u3nj0103r	1998 Mar 15	1300	H_α
u3nj0104r	1998 Mar 15	1300	H_α
u9570201m	2005 Jan 22	1200	[SII]
u9570202m	2005 Jan 22	1200	[SII]
u9570101m	2005 Jan 21	1200	H_α
u9570102m	2005 Jan 21	1200	H_α

The 1996 (1996.034), 1998 (1998.074), and 2005 (2005.021 and 2005.022) observations consist of 2 exposures for each filter *F656N* (H_α) and *F673N* ([SII] doublet: $6717, 6731$Å). Dividing each exposure into sub-exposures in order to be able to clean the images from cosmic ray hits, we achieved a total exposure time of 2005 s, 2600 s, and 2400 s for each filter in 1996, 1998, and 2005 respectively (see Tab. 4.1).

4.1.2 Data reduction

Data reduction is made following the main steps shown in Fig. 4.3 (the IRAF[2]/STSDAS[3] tasks used are in brackets).

Briefly, I used the IRAF/STSDAS software environment in order to remove the warm pixels in WFPC2 CCDs (using the STSDAS task **warmpix**). This is an important step because one of our aim is to estimate the fluxes of faint extended sources which could be modified by the presence of such hot pixels. An analogous problem could rise in the case of presence of cosmic ray events near the sources I want to analyze. To avoid errors in computing fluxes due to the

[2]IRAF is the Image Reduction and Analysis Facility, a general purpose software system for the reduction and analysis of astronomical data. IRAF is written and supported by the IRAF programming group at the National Optical Astronomy Observatories (NOAO) in Tucson, Arizona.

[3]The Space Telescope Science Data Analysis System (STSDAS) is a software package for reducing and analyzing astronomical data. It is layered on top of IRAF and provides general-purpose tools for astronomical data analysis as well as routines specifically designed for HST data.

1. Retrieval of data
2. Read data into IRAF (convert from FITS to GEIS format; strfits)
3. Check whether recalibration is necessary
4. Ricalibration
5. Warm pixel rejection (warmpix)
6. Cosmic Ray rejection (crrej e fimgtrim)
7. Photometric Calibration (imcalc)
8. Cosmetic improvement (wfixup)
9. Mosaics (wmosaic)
10. Trasform GEIS in FITS (stwfits)
11. Find the position of VSS 4
12. Register 1998 and 2005 with 1996 (taking into account VSS4 proper motion)
13. Apertures on knots (3 cnts/pix)
14. Flux estimation: Flux = (Flux no background subtracted) - sky
15. Position of each knot
16. Position of the brightest spot within the D knot
17. Proper motion of each knot
18. $\tau_{cooling}$
19. H_α - [SII]
20. [SII]/H_α

Figure 4.3: Main steps of the data analysis of the HST data. The tasks used are in brackets.

influence of cosmic ray emission, I remove the cosmic rays by using the STSDAS task **crrej** in the two exposures for each filter for the three epochs. Due to the fact that cosmic ray events are very numerous in long exposures, several pixels are affected by double hits, which cannot be removed by running the crrej task (which just compares the two exposures). So I need to identify cosmic ray and to remove them in each image (using the task **fimgtrim**).

The images have been interpolated across bad pixels using the STSDAS task **wfixup** and mosaics are obtained of all four detectors images of WFPC2 using the STSDAS task **wmosaic**, which takes into account chip distortions and rotation, and reduces the PC field to the same resolution as the three WF images. Note that these images are only for illustrations purpose. All the quantitative results and measurements are derived by the single chip images (in particular for those concerning the structures detected in the high resolution camera, PC).

What is new in my analysis especially compared to the procedure of FL05 is the method used to register the images and to define the apertures around each structure within the jet, in order to derive the position and the total flux of each knot and consequently its proper motion and emission variability, by comparing the multi-epochs observations. First of all I match the images in the three epochs by using the World Coordinate System in SAOImage ds9. In this way I rotate the image so as to have the North up and the East on the left of the image (this

is analogous to rotate the figure of the value of the header keyword ORIENTAT) and I register the position of the center coordinate as the right ascension and declination of each camera. As a next step, I find the position of the VSS4 star in the WF4 chip for both filters in the three epochs. From a comparison of the positions of the star in 1996, 1998, and 2005 I have found an offset which I account for in registering the multi-epochs observations. Furthermore, the VSS4 star shows a significant proper motion (Cudworth & Herbig 1979), which in 9 years, the time baseline between 1996 and 2005 observations amount to (+0.″14,-0.″54). I have taken into account the proper motion of VSS4 together with the offset found between the multi-epochs observations in the position of VSS4 in the WF4 chip to register the images, in order to compute the proper motion of each substructure within the jet. The accuracy in the shift measured between 1998 and 2005 images with respect to the 1996 position of the VSS 4 star in WF4 chip is ~ 0.1", due to the resolution of the camera.

In order to identify in each epoch the single structures within the jet in both filters, I tested several criteria concerning the choice of the contours defining each knot. The position of these contours will allow us to define the position of each knot and, as a consequence, to derive the proper motion of the knots by comparing the multi-epochs images in both filters, as discussed in sect. 4.2.3. First, I used contours at a fixed fraction of the maximum flux in each knot. Noting that the value of these maxima are different for different structures (i.e. the maximum is a local property of each knot), I decided not to use such a procedure as a definition of the contours around the structures. On the other hand, also the value of the background varies, up to 4 times between 1996, 1998 and 2005 images. So I have chosen not to use contours at $k\sigma$ with respect to the background to identify the structures. These considerations lead us to choose a fixed threshold for the contours in each epoch. In particular I obtained that in 1996, 1998 and 2005 H_α images of HH 154 the knots within the jet are well defined as separated structures if contours at 3 cnts/pix are used. This makes sense because of the exposure being almost the same across the whole set. This value corresponds to contours at about 1000σ, 500σ and 600σ with respect to the background for the 1996, 1998 and 2005 H_α data, respectively.

The new method that I have developed for the identification of the substructures within the jet and that is described above, leads for the first time to a quantitative and reproducible definition of the contours on each knots in protostellar jets.

4.1.3 Photometric calibration

The contours used to define the knots within the jet are also used to measure the total flux of each structure: I compute the total flux within the contour on

each knot. This value takes into account also a contribution due to the sky. In order to derive the flux associated to the knot itself, I subtract the background by estimating the value of the sky within the same contour defining each knot. This procedure leads to the consequence that any bias level removal is unnecessary. The comparison of the multi-epochs estimations of fluxes will allow us to derive informations about the energetics of the substructures within the jet and of the jet as a whole as well. Photometric calibration is made following Holtzman et al. (1995) calibration for narrow-band filters. The fluxes are represented as erg cm^{-2} s^{-1} and are derived by the observed counts as

$$F = \frac{DN}{s}\frac{14}{GR}\frac{E}{A\,QT\,1.1} \tag{4.1}$$

where F is the total flux in the line, DN/s are the detected counts per second, GR and QT are parameters which take into account the instrumental response ($GR = 1.987$ for the PC1 chip, 2.003 for WF2, 2.006 for WF3, 1.955 for WF4; $QT = 0.11978$ for the [SII] filter, 0.11273 for the H_α filter), $E = hc/\lambda$ is the energy of a photon at the wavelength of the line, $A = \pi R^2$, where $R = 120$ cm is the radius of the HST primary, 1.1 is a correction factor.

4.2 Results

4.2.1 Morphological changes

In Fig. 4.4, I show the 1996 (left panels), 1998 (middle panels) and 2005 (right panels) HST observations of the HH 154 jet in the H_α (upper panels) and [SII] (lower panels) filters.

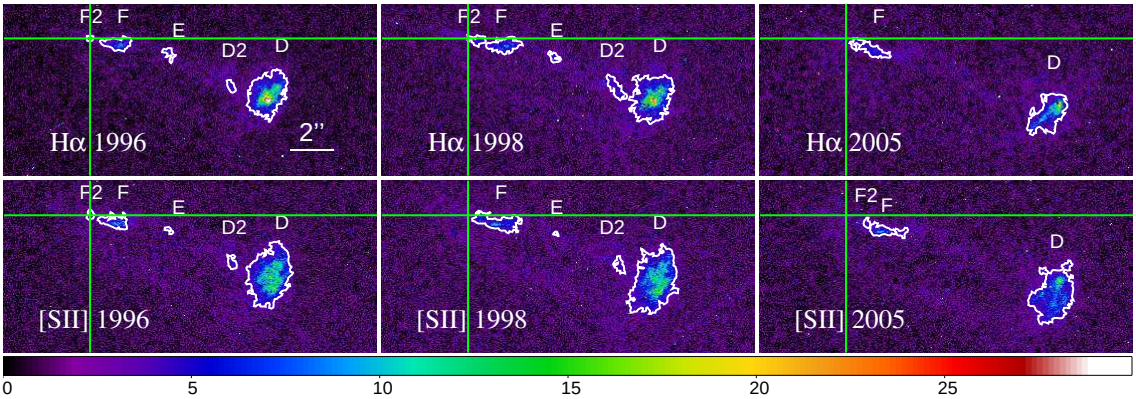

Figure 4.4: Multi-epoch image of the HH 154 jet in 1996 (left panels), 1998 (middle panels) and 2005 (right panels) in H_α (upper panels) and [SII] (lower panels). The green cross superimposed on each panel marks the same position in each image, corresponding to the center of the knot F_2 in 1996.

The jet consists of two separate components ('northern jet' and 'southern jet'). As suggested by Fridlund & Liseau (1998), these two jets can be traced (Rodríguez et al. 2003a) each to be originating from one of the two components of IRS5 found by Looney et al. (1997) and by Rodríguez et al. (1998). This structure is, however, not immediately evident in the representation of Fig. 4.4, but it is evident from the mosaic image of the 1996 HST observations of the HH 154 jet (Fig. 4.5), the emission from the southern jet is fainter than the more active northern jet. Even the knots observed at the end of the fainter jet have emission several order of magnitude lower that those at the head of the northern jet.

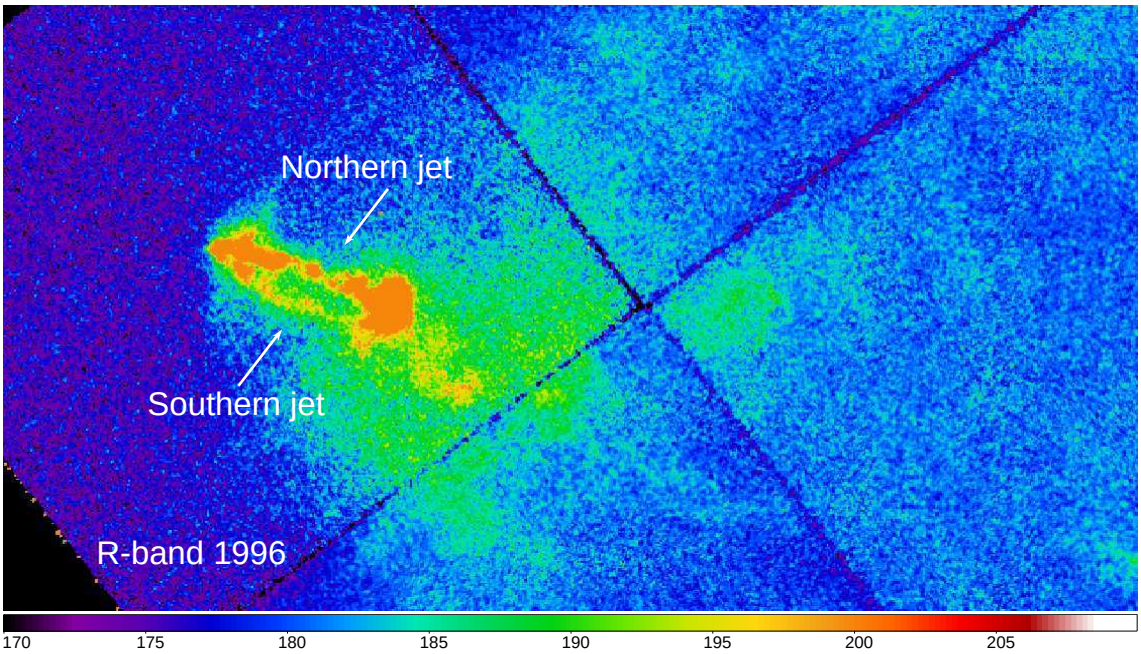

Figure 4.5: R-band image of the HH 154 jet as detected with HST in 1996.

The knotty structure within the jet is evident (the nomenclature of each knot inside the jet is according to Fig. 1, lower panel of Fridlund et al. 2005) even in the Fig. 4.6 which shows a cut of the HH 154 jet along the axis direction.

The HH 154 jet emerges from the highly obscured ($\approx$ 150 mag) region surrounding the driving source IRS5 and the first visible structure at the basis of the jet is the 'F-complex' (nomenclature of FL05 – see enlargements of the basis of the jet in H_α and [SII] in Fig. 4.7). It consists of 2 knots, F_2 and F, merging in a single stretched structure as it evolves (see 2005 H_α image, upper right). At this position, the extinction is between 4.5 and 6 magnitudes in V, while at the very base of the jet it is significantly larger.

From Fig. 4.7 the variation of the emission and of the morphology of the F-complex with time and with wavelength is evident. First of all the knot F_2

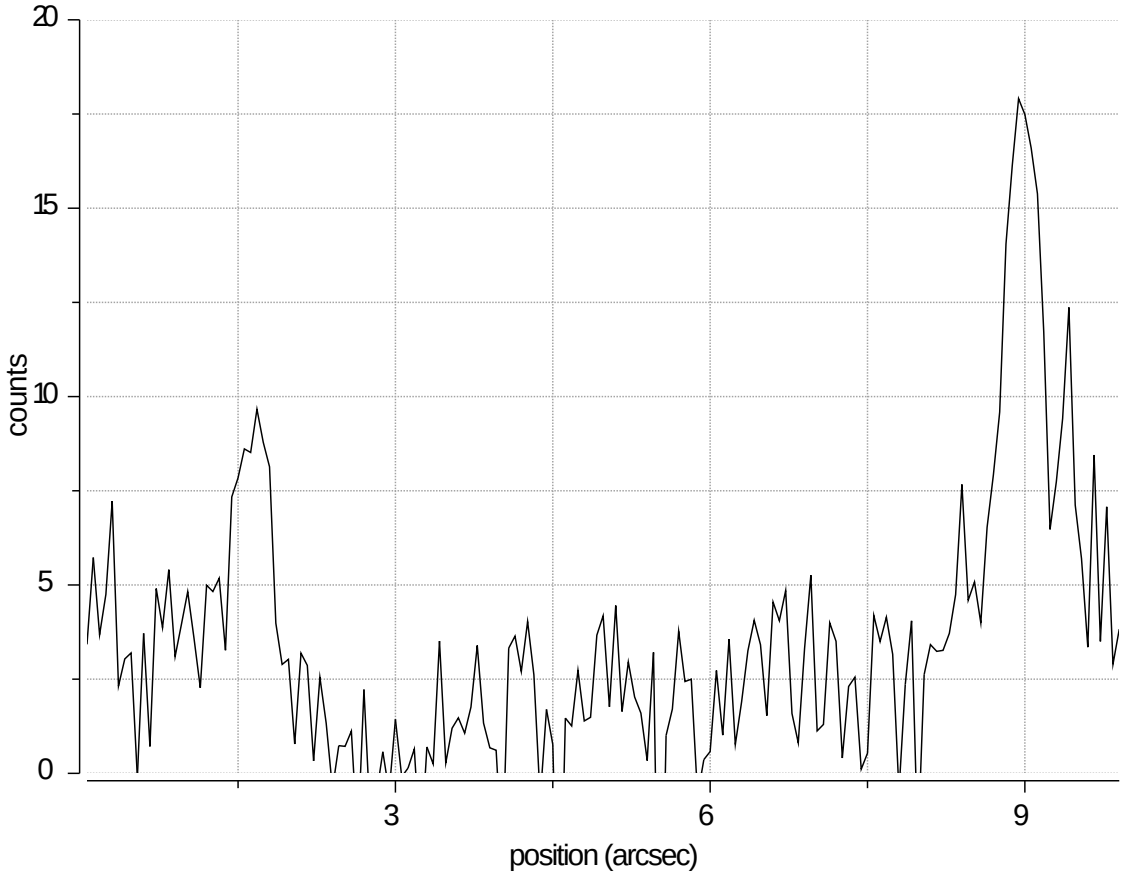

Figure 4.6: Cut along the axis of the HH 154 jet as detected with HST in 1996 in the H_α filter.

seems to approach knot F with time. Furthermore the whole F-complex evolves as a single elongated structure in the new 2005 observations.

The middle section of the jet is now very faint and devoid of large structures, and a trend is clearly seen in the images over the period covered by our HST observations especially in the new 2005 observations. In a similar way as in the case of the F-complex discussed above, the knots in the middle part of HH 154 show changes in emission and have variable morphology with time in our data. The faint structures within the middle portion of the HH 154 jet, knot E (near the F-complex) and knot D_2 (near the terminal working surface, knot D), seem to become fainter and fainter, vanishing in our new 2005 observations or maybe decomposing into several sub-knots, remnants of previous individual knots (see Fig. 4.8), or merging with other structures.

The brightest knot within the HH 154 jet, knot D, is located at the head of the jet (far from the source IRS5, from which the jet originates) and can be identified with the terminal working surface, where the jet interacts with the surrounding medium. The morphological changes of the spatial structures are well visible not

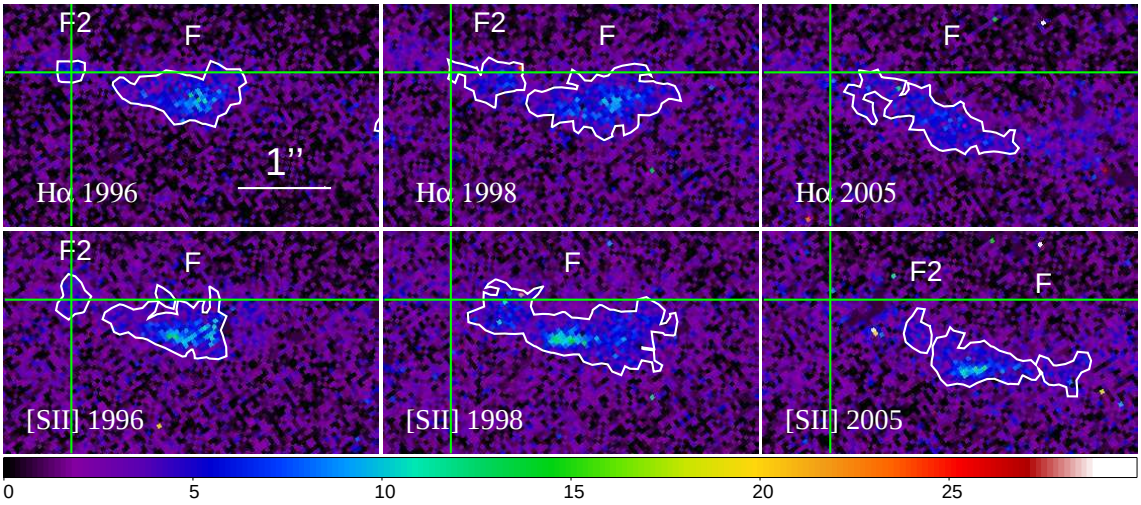

Figure 4.7: Enlargement of the F-complex at the basis of the HH 154 jet in 1996 (left panels), 1998 (middle panels) and 2005 (right panels) in H_α (upper panels) and [SII] (lower panels). Contours for the identification of knot F_2 (on the left) and F (on the right) are superimposed on this figure. The green cross superimposed on each panel marks the position of the center of knot F_2 in 1996, H_α, as in Fig. 4.4.

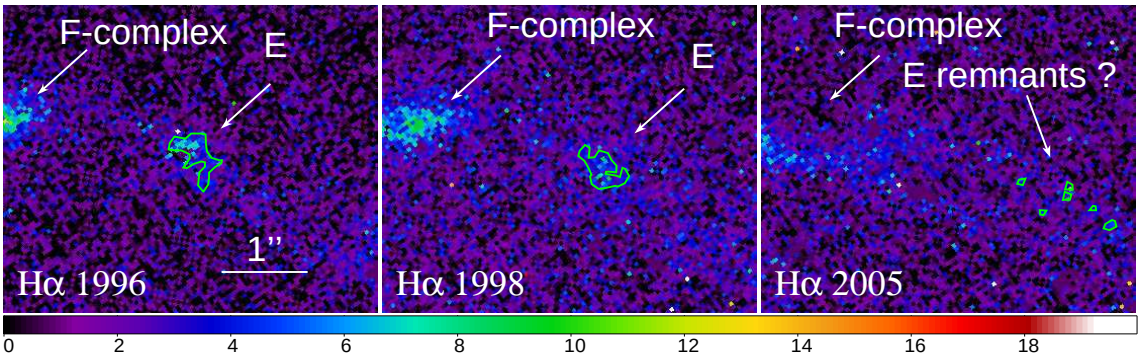

Figure 4.8: The E knot within the HH 154 jet in 1996, 1998 and 2005 observation in H_α filter. In 2005 this knot is disappearing or is decomposing into several remnants.

just within the jet as a whole, but even within each single small structure (optical knots). This is evident in the case of knot D, as shown in Fig. 4.9, where a shift of the brightest spot within the knot itself is detectable. In particular, I measure the shift of the brightest spot within the knot D deriving a value of about 1″ in the NW direction in about 9 years (it was about 0.3″ between 1996 and 1998), in the reference system of the knot itself (Fig. 4.10). Details on the value of the maximum of the brightest spot within the D knot and on its position in H_α images in 1996, 1998 and 2005 are summarized in Tab. 4.2.

Feature D_2 appears to be merging with the working surface, knot D. The process continues and now our new 2005 HST observations show no presence of traces of this knot near the working surface D. This can have influenced the

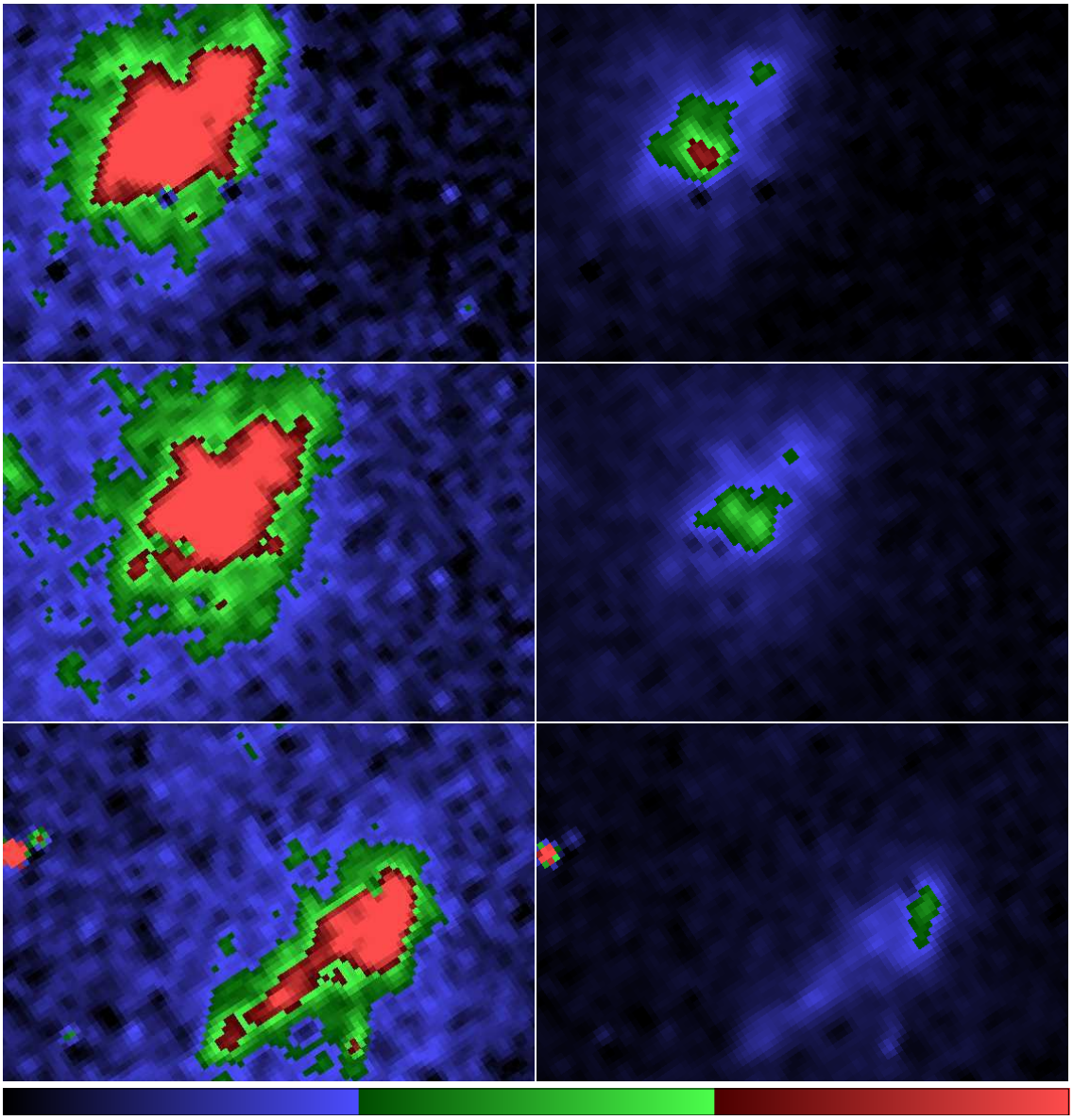

Figure 4.9: Enlargement of the terminal working surface, knot D, at the head of the HH 154 jet in 1996 (upper panels), 1998 (middle panels) and 2005 (lower panels) in H_α, at 2 different contrast levels: high contrast (on the left) to show the fainter features and low (on the right) to show the brighter features.

detectable movement of the brightest spot observed within the knot D towards the NW direction.

4.2.2 H_α and [SII] structure

H_α emission identifies the position of the shock, in fact collisional excitation of neutral atoms entering the shock marks the physical location of the shock front itself. Otherwise, the cooling zones behind the shock front mainly emit forbidden

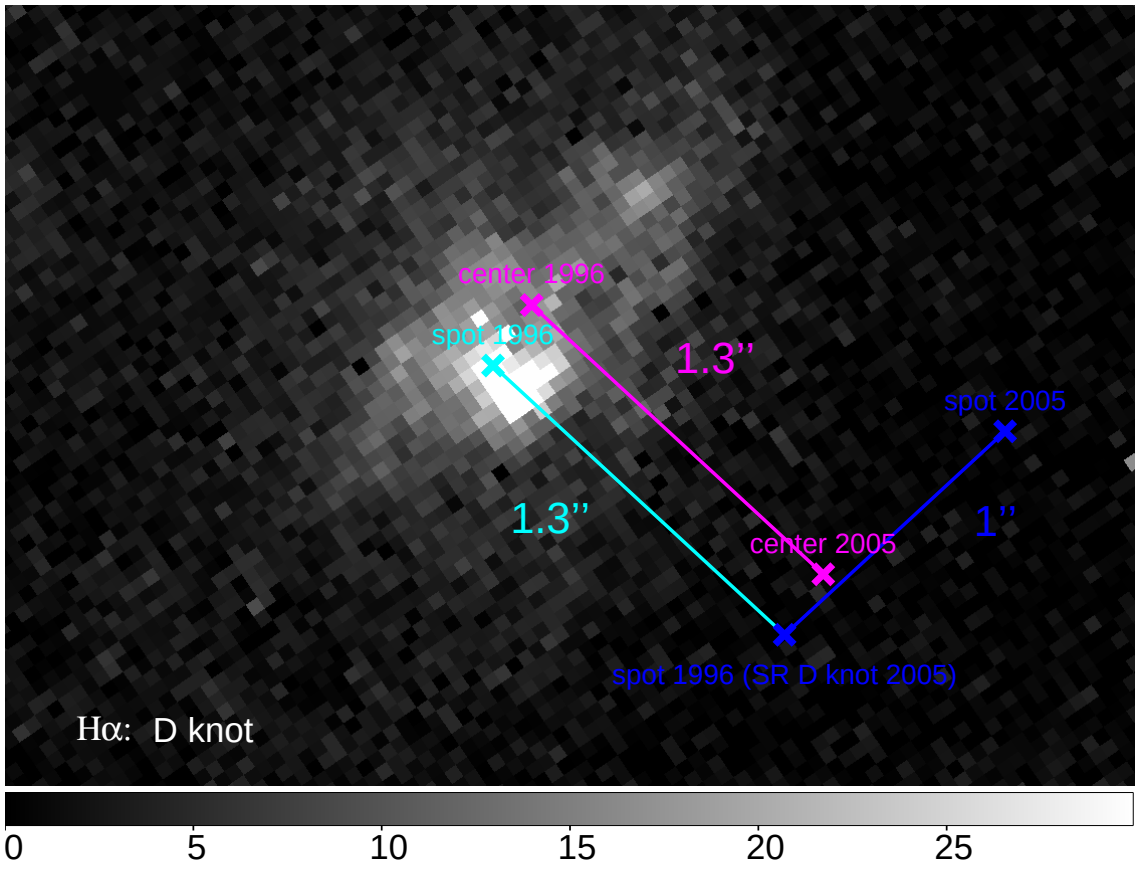

Figure 4.10: Displacement of the brightest spot within the D knot within the HH 154 jet in the reference system of the knot itself.

Table 4.2: Position and value of the maximum corresponding to the bright spot within the D knot evaluated from the H_α images in 1996, 1998 and 2005.

yr	max (cnts)	position (deg)
1996	37.2284	(67.88939, 18.13391)
1998	29.6317	(67.88926, 18.13388)
2005	20.6488	(67.88890, 18.13385)

line radiation, such as [SII]. Hence the stratification of the H_α and [SII] emission makes it possible to recognize the location of two very different physical regions within protostellar jets.

To this end in Fig. 4.11 we show the difference image H_α - [SII] of the HH 154 jet as a whole as observed with HST in 2005. As pointed out by Fridlund & Liseau (1998), the difference image results in the cancellation of the jet, leading to the conclusion that the central part of the jet is of intermediate excitation ([SII]/H_α < 1.5, Raga et al. 1996). At the spatial resolution of HST/WFPC2, I expect to be able to resolve the shock structure of the brightest knots. The

working surface consists, in general, of two shocks, the bow shock and the Mach disk, marked by the H_α emission, and of a cooling zone (between the shocks) marked by the [SII] emission. The bright and dark structures in the difference image in Fig. 4.11 are indicative of a stratification in the two different emission, H_α and [SII], corresponding to the two different physical zones, the shock front and the post-shock region in the particular case of the HH 154 jet.

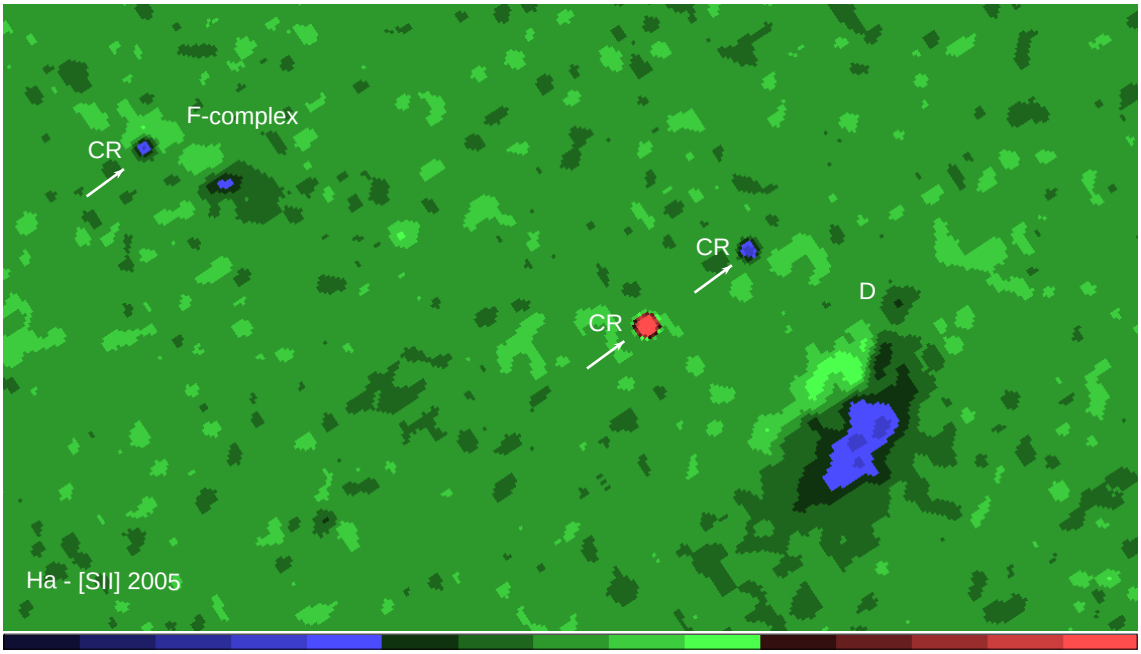

Figure 4.11: Difference image H_α - [SII] of HH 154 as observed with HST in 2005. Cosmic rays not subtracted by the images are marked in the figure.

In particular, in Fig. 4.11 there is no evidence of H_α emission marking the forward shock (bow shock) expected to be furthest away from IRS5 with respect to the location of the cooling zone marked by the [SII] emission.

H_α emission of the brightest knot, the D knot, appears to vary from an almost ellipsoidal blob in both 1996 and 1998 HST observations (see upper and middle panels in Fig. 4.9) to the most elongated structure observed in 2005 (see lower panels in Fig. 4.9). This stretched blob is evident in the difference image H_α - [SII] derived from 2005 observations (Fig. 4.11). Here the [SII] cooling region appears to wrap around the H_α emitting region corresponding to the reverse shock.

A similar structure seems to be present at the position corresponding to the complex F at the base of the jet, where the jet velocities reach their maximum value (Fridlund et al. 2005). This could be evidence of a new shock formed near the parent star, where X-ray emission has been detected with Chandra (Bally et al. 2003; Favata et al. 2002).

4.2.3 Proper motion

The three different HST observations of HH 154 in three epochs (1996, 1998 and 2005) allow us to perform proper motion measurements with time basis of about 2 years and of about 9 years, i. e. to derive average velocities over 9 years, comparing the 1996 and 2005 HST data sets, and almost "instantaneous" velocities over 2 years, from 1996 and 1998 observations.

Fig. 4.12 shows the RGB image of the HH 154 jet in 1996 (blue), 1998 (green) and 2005 (red) in both H_α (left panel) and [SII] (right panel) filters: the elongation of the jet over few years is well visible from this figure and strongly suggests a detectable motion of the knots within the jet and of the jet as a whole.

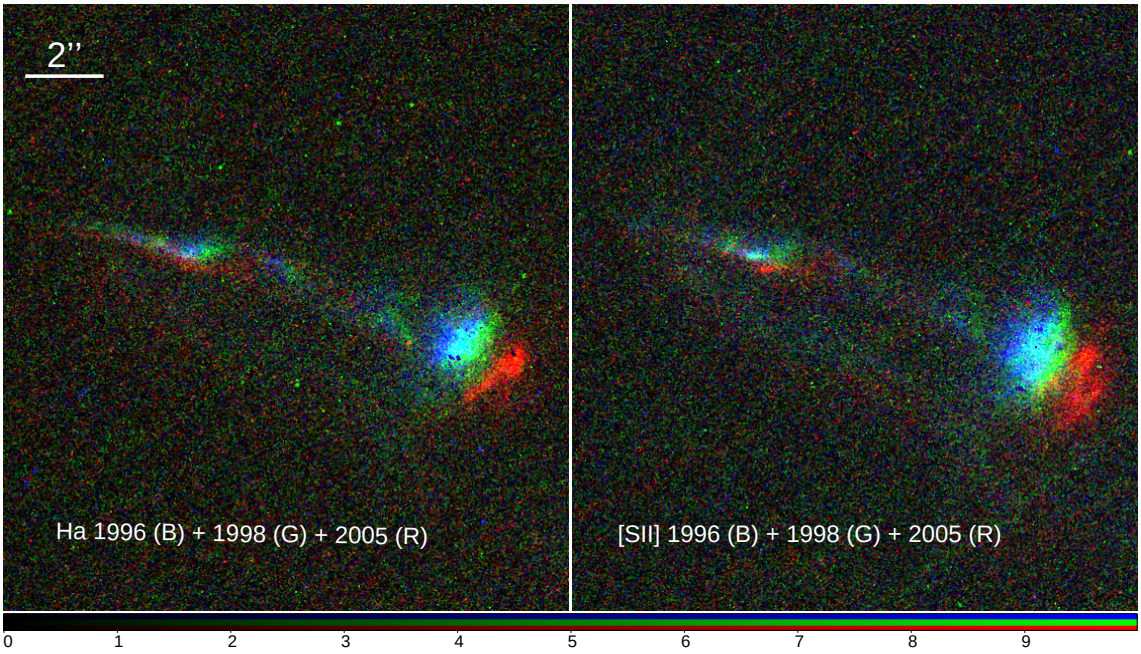

Figure 4.12: RGB image of the HH 154 jet in 1996 (blue), 1998 (green) and 2005 (red) in H_α (left panel) and [SII] (right panel).

The contours defining the knots within the jet are chosen following the method described in sect. 4.1. Fig. 4.4 shows each substructure in the jet and the corresponding contour.

Once a criterion for the identification of each knot has been chosen, as discussed in sect. 4.1, I derive the position of the center of the contours defining the knots. To calculate the center of a polygon, one sums the vector for each vertex and then divides by the number of vertexes (SAOImage ds9 support team, private communication). Note that the position of the center of the contour does not necessarily correspond to the position of the maximum of the knot within the contour. A consequence is that the proper motion of the D knot, computed by considering the position of the center of the contour, does not account for the

motion of the brightest spot within the D knot itself. However, our choice of the contours lead to the definition of a single structure consisting of both knots F and F_2 in [SII] image in 1998 and H_α image in 2005 (see Fig. 4.4, central lower panel and right upper panel). In this case I compare the position of the maxima corresponding to each knot separately to compute the proper motion.

Starting from the estimation of the physical quantity that I can directly measure, i.e. the position of the knots, I can infer the instantaneous (over 2 yr) or average (over 9 yr) velocity of each sub-structure within the jet.

Tab. 4.3 summarizes the displacements of the position of each knot in about 2 (from 1996 to 1998) and 9 years (from 1996 to 2005) in both filters and the corresponding proper motion.

Note that I consider different values of the velocity in the H_α and [SII] filters as these two emissions refers to different physical regions, as explained in sect. 4.2.2.

I can only compare the average speeds derived over 9 years, from 1996 to 2005, with the "instantaneous" speeds derived over 2 years, from 1996 to 1998. It would be very interesting to perform new HST observations of the HH 154 jet in the next few years so as to be able to compare "instantaneous" velocities. This comparison would allow us to infer detailed informations on the dynamics of the protostellar jet, the deceleration of its knots being one of the main topics. From the HST data sets reported in this paper, I can argue that the average speed of the knots at the basis of the jet (the F-complex) over the last 9 years is significantly lower (of about a factor of 4; see Tab. 4.3) than the "instantaneous" speed over 2 years observed 9 years ago, suggesting a deceleration of this region.

The same is not valid in the case of the D knot, whose average speed increases of about 26% with respect to the "instantaneous" speed derived about 9 yr ago (see Tab. 4.3). Here there are indications of a slight acceleration of the D knot during the last 7 years (from 1998 to 2005), but it remains to be confirmed through later epoch observations.

The faintest knots within the jet, the E and the D_2 knot, disappeared in new 2005 observations (see discussion in sect. 4.2.1), making it impossible to infer details concerning their dynamics from the direct comparison of the velocities.

The variation of the length of the jet as a whole is shown in Fig. 4.13 and the corresponding values are presented in Tab. 4.4 for each epoch in both filters. The length of the total jet is defined as the distance between the extremes of contours on "complex F" (or knot F_2 if it is well defined) and knot D.

The average change in length found during this period (from 3 Feb. 1996 to 21-22 Feb. 2005 = 3306-3307 days) derived from the values in Tab. 4.4 is 0.082"/yr in H_α and 0.048"/yr in [SII], corresponding to a space velocity of about 58 km/sand 34 km/s, respectively.

Table 4.3: Proper motion computed for each knot within the jet. For knots F and F_2 we use the position of the maxima within the contours ("max" in the column "Comment") instead of the position of the center ("center" in the column "Comment") of the contours (see text for discussion).

Δt	Feature	displacement H_α	displacement [SII]	v@150pc H_α	v@150 pc [SII]	v error	Comment
yr		arcsec	arcsec	km/s	km/s	km/s	
1998 - 1996	D	0.24	0.28	84	99	36	center
1998 - 1996	D_2	0.35	0.46	125	165	36	center
1998 - 1996	E	0.38	0.46	134	164	36	center
1998 - 1996	F	0.39	0.28	138	100	36	max
1998 - 1996	F_2	0.75	0.93	265	331	36	max
2005 - 1996	D	1.34	1.54	106	122	8	center
2005 - 1996	D_2	-	-	-	-	-	disappeared in 2005
2005 - 1996	E	-	-	-	-	-	disappeared in 2005
2005 - 1996	F	0.24	0.74	19	58	8	max
2005 - 1996	F_2	0.76	1.19	60	94	8	max

Table 4.4: The length of the jet at different epochs and in both H_α and [SII] filters computed as the distance between the extremes of contours on knots F_2 (or "complex F" when there is a single contour for both F_2 and F knots) and knot D. Δt is the number of days between successive epochs.

Filter	Year	Δt	Length	Rate of change	Rate of change@150 pc		v error
		days	arcsec	arcsec/yr	AU/yr	km/s	km/s
H_α	1996	0	9.53	-	-	-	-
H_α	1998	771	9.74	0.0997	15	71	36
H_α	2005	2535	10.27	0.0765	11	54	10
$[SII]$	1996	0	9.76	-	-	-	-
$[SII]$	1998	771	10.02	0.1234	19	88	36
$[SII]$	2005	2536	10.19	0.0245	4	17	10

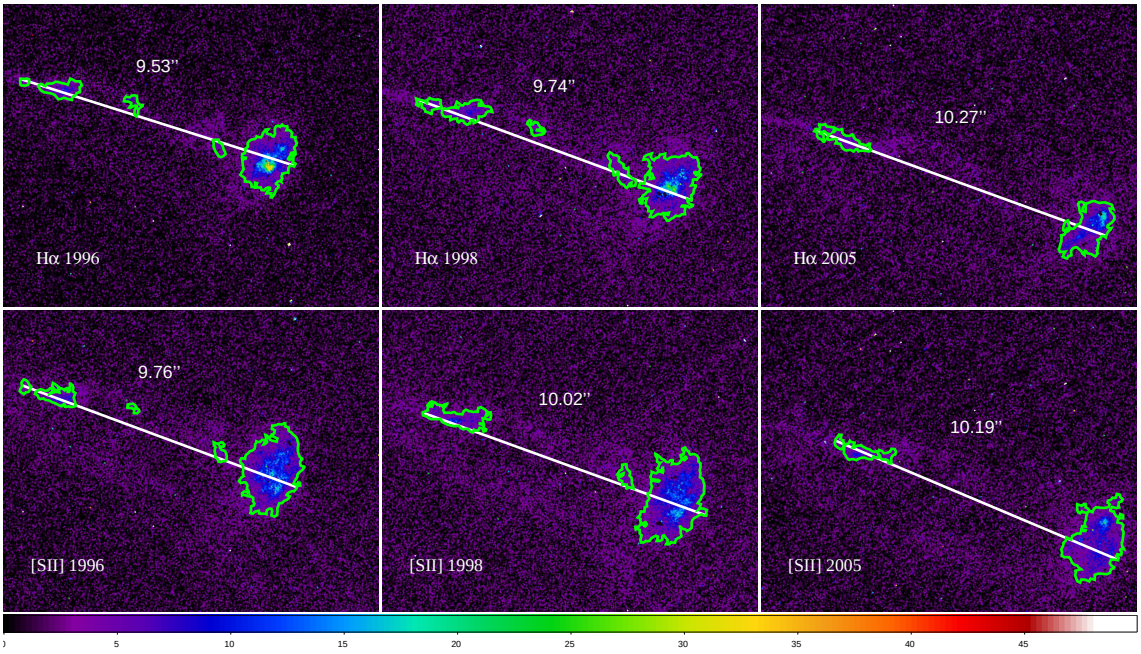

Figure 4.13: Total length of the HH 154 jet in 1996 (left panels), 1998 (middle panels) and 2005 (right panels) in H_α (upper panels) and [SII] (lower panels).

4.2.4 Flux

In order to investigate the energetics describing the evolution of the knots within the HH 154 jet, I measure the fluxes inside the contours which define each structure in the jet (I use the same contours used in deriving the proper motion of the knots, as in sect. 4.2.3). Our results are summarized in Tab. 4.5, where I present the total flux collected in the apertures around each single knot when it is well defined, as in the case of knot D in both filters and for all the three epochs, or in the aperture containing multiple structures, as in the case of F-complex (in [SII] image in 1998 and H_α image in 2005, Fig. 4.4, central lower panel and right

upper panel). Note that the apertures on each knot have different sizes for different epochs or filters. In fact one of the main characteristics of the sub-structures within the jet is their rapid morphological evolution in few years.

The relative variations of the fluxes in 1998 or 2005 with respect to the 1996 values give us information concerning the activity of each knot within the jet and of the jet as a whole. In more details, the flux measured from the D knot decreases of the 7% in [SII] from 1996 to 1998 up to the 46% in H_α from 1996 to 2005. The same is true for F and E knots, whose fluxes decrease up to 6% and 51%, respectively. On the other hand, the fluxes of the F_2 and D_2 knots increase. An explanation of this result can be related to the fact that my choice of the contours defining the knots leads to greater apertures on these two knots, F_2 and D_2, in the epochs corresponding to higher fluxes. As said above, I am comparing fluxes within different areas in different epochs, because we are interested in following the evolution of the substructures in the jet, even their morphological variations. So I do not fix the areas of the knots through the epochs but let them change as the jet evolve. Computing the surface brightness of F_2 knot, as an example, I obtain that it decreases, thus leading to a 1998-to-1996 areas ratio increasing faster than the corresponding fluxes ratio, and I can conclude that the increased flux observed is due to increasing area, since the surface brightness itself decreases.

The total flux of the jet as a whole, defined as the sum of the fluxes of each knots and shown in Tab. 4.5, varies decreasing from its maximum value of about 1.6×10^{-14} erg cm^{-2} s^{-1} in 1996 to its minimum of about 8.8×10^{-15} erg cm^{-2} s^{-1} in 2005, in the H_α filter, and from its maximum value of about 1.7×10^{-14} erg cm^{-2} s^{-1} in 1996 and 1998 to its minimum of about 1.3×10^{-14} erg cm^{-2} s^{-1} in 2005, in the [SII] filter. The contribution of the single knots to the total flux of the jet as a whole ranges from 2% of the faintest knots, D_2 and E, to 88% of the brightest knot, the terminal working surface, i. e. the knot D. The flux of F-complex at the base of the jet contributes $(11 - 20)\%$ to the total flux.

4.3 Discussion

We first focus on the terminal working surface, identified with the D knot at the head of the jet. The H_α emission is interpreted as the emission originating from the Mach disk and the [SII] emission as due to the post-shock region just behind the bow-shock. Following the Hartigan (1989) model, a Mach disk significantly brighter than the bow shock, as evident in Fig. 4.14, is indicative of a jet traveling through a denser ambient medium, in good agreement with the Bonito et al. (2004, 2007) (see also Chapter 2) numerical results. In fact one of the main result of their model is that only a narrow range of parameters of the jet/ambient system can reproduce the observations of protostellar jets. In particular only the

scenario of a "light jet", i. e. the case of a jet traveling through a denser medium, can reproduce the observations of the HH 154 jet, concerning the proper motion of the X-ray source, its emission and spectral behaviour.

The separation observed between the centers of the contours defining the knot D in H_α and [SII] is about 0.″38 (Fig. 4.14), consistent with the dimension of the width of the basis of the jet. As in Hartigan (1989), both the bow shock and the Mach disk are radiative, the separation being of the order of the jet radius.

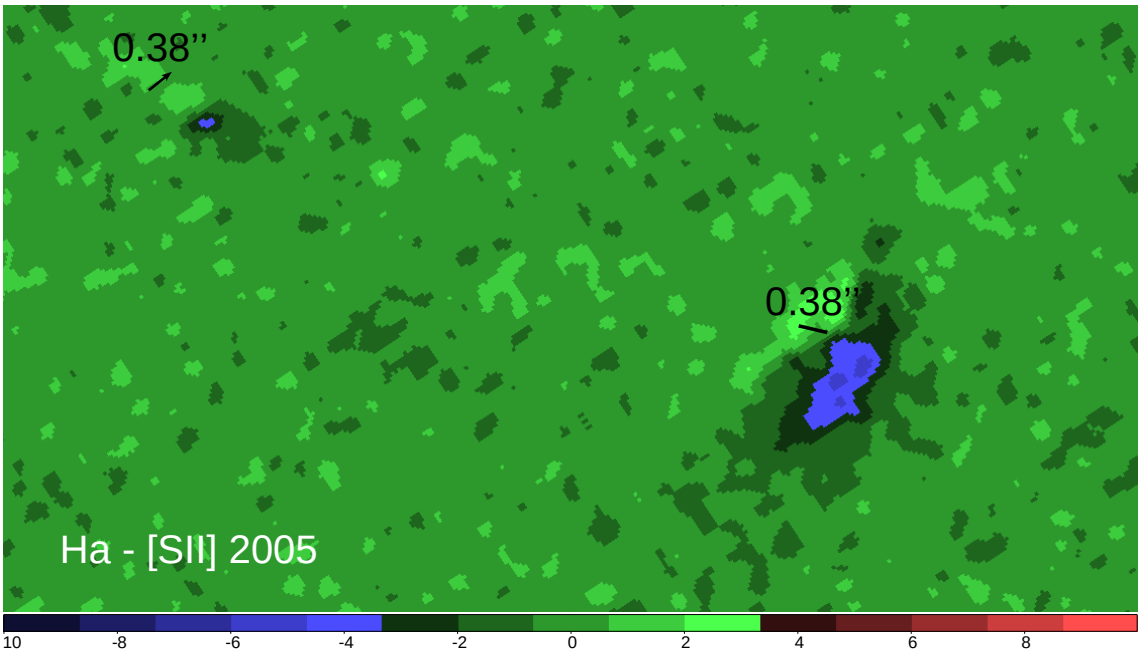

Figure 4.14: Difference image H_α - [SII] of HH 154 as observed with HST in 2005. Contours on each knot in H_α (red) and in [SII] (white) are superimposed on the figure. The arrows indicate the dimension of the jet radius at its basis and the cooling length, defined as the distance between the center of the contour on the D knot in H_α and in [SII].

In sect. 4.2.3, I realized that, unlikely the other sub-structures within the HH 154 jet, the terminal working surface, identified as the D knot at the head of the jet, shows indication of acceleration (the velocity increases up to 26%) during the last 7 years, i.e. from the 1998 observation to the last one, in 2005. In order to explain this result, I also point out once again that the fast D_2 knot (see its velocity in Tab. 4.3) disappears in our new HST observations collected in 2005 (see right panels in Fig. 4.4). From this consideration, I can argue that possibly a collision between the two knots, D and D_2, has occurred during the 7 years between 1998, when the D_2 knot is still well visible in both H_α and [SII] images of HH 154 (see central panels in Fig. 4.4), and 2005. Using the velocities shown in Tab. 4.3 and the density derived in FL05 (assuming quasi-spherical knots for simplicity), I derive, from the equation for momentum conservation in a totally inelastic collision, the density of the D_2 knot. It should be about 30 times denser

than the D knot in order to explain a totally inelastic collision between the two knots, leading to the higher speed observed in the D knot in 2005. This collision between the two knots, D_2 and D knots, could also explain the detectable motion of the brightest spot observed within the D knot (Fig. 4.9).

As I pointed out in sect. 4.2.3, F and F_2 knots speed decreases in the time baseline of about 9 years from 1996 to 2005 (E and D_2 knots are almost disappeared in new 2005 observations). Together with this time dependence of the velocity of the knots in the jet, there is also a dependence with the distance from the protostar along the jet axis ("space dependence"). In fact there is a clear decrease in the velocity derived in 1998 with increasing distance from the protostellar source IRS5, at the base of the jet. In fact the maximum value of the knots speed is measured at the basis of the jet, where the F_2 knot is, and then the speed decreases along the jet axis, reaching its minimum value at the head of the jet, corresponding to the terminal working surface, the D knot (Tab. 4.3). In particular, the velocity of the F_2 knot is almost three times greater than the D knot's speed, $v(F_2) \approx 3 \times v(D)$. Both time and space dependence of the speed of the sub-structures within the jet can be used as a strong diagnostic power in detailed numerical simulations. In fact, as I explained in Chapter 2 (see also Bonito et al. 2004, 2007), the shock formed at the interaction front between a supersonic protostellar jet and the surrounding medium travels at a velocity which is up to a factor of three lower than the initial jet velocity in the case of a light jet, ten times less dense than the ambient through which it propagates. Once again I stress the fact that new small time-spaced observations of the HH 154 jet with HST could lead to more information about the "instantaneous" velocity instead of the average one derived with long time-spaced observations (as 1998 and 2005). By following this approach I could constrain the relevant physical parameters describing the jet/ambient system, as their density ratio, the initial jet velocity and the shock speed, and so on.

The direct measurements of the fluxes of each sub-structure within the HH 154 jet, in the three different epochs (1996, 1998, and 2005) and in both H_α and [SII] filters, allow us to infer important information concerning the dynamics of the knots in the jet. In particular, I can compare the variation of the fluxes in about 2 or 9 years with the rate expected during the characteristic time scale of cooling by radiative losses. FL05 derived the following temperatures and densities from spectroscopic data for the D and F knots in [SII]: $T_e(D) = (8700 \pm 1000)$ K, $T_e(F) = (14250 \pm 1750)$ K, $n_e(D) = (1600 \pm 200)$ cm^{-3}, and $n_e(D) = (1800 \pm 200)$ cm^{-3}. According to these values, I obtained a characteristic time scale for the radiative cooling, $\tau_{cool} \approx 290$ yr for both knots. We expect the fluxes of the knots to be reduced by a factor of 0.969 in 9 years (from 1996 to 2005) and by a factor of 0.993 in 2 years (from 1996 to 1998). However, the ratio between the fluxes in the two epochs (i.e. F_{2005}/F_{1996} or F_{1998}/F_{1996}) are much lower than expected (in

fact from Tab. 4.5, I derive: $F_{2005}/F_{1996} = 0.73$ and $F_{1998}/F_{1996} = 0.93$, for the D knot, and $F_{2005}/F_{1996} = 0.94$ for the F knot, while in 2005 the F knot cannot be identified within a single contour). Comparing the above results, I can conclude that the D and F knots cool down faster than expected (with the hypothesis that they are isothermal structures). I estimate the characteristic time scale for the thermal conduction and it is several order of magnitude greater than the cooling time scale. Thus the radiative losses effects dominate over the thermal conduction effects. So we can suppose that the jet propagates turbulently into the surrounding medium and, as a consequence, a merging between the knot and the ambient medium is occurring. This process could reduce the emission from the knot itself more than if the structure were isolated, i.e. not interacting with the surrounding. So we are observing at an evidence of the strong interaction between the jet and the ambient through which it is traveling supersonically.

The excitation index defined by the ratio of [SII] to H_α flux (Raga et al. 1996) indicates the level of excitation of all the substructures in the jet. In Tab. 4.6, I show the value of the excitation index for each knot in the three different epochs.

Among all the substructures in the jet, only the knot D, the working surface, shows an excitation index greater than 1.5 (in 2005), indicative of a low-excitation emission. However the [SII]/H_α ratio of the D knot varies in about 9 years, ranging from 1.15, 1996, to 1.57, 2005. This behaviour corresponds to an initial high excitation emission from this structure, which is weakening with time. The opposite is true for the F-complex at the basis of the jet, from which is likely that the X-ray source observed with Chandra (Favata, Bonito et al. 2006) originates. In fact in the case of the F-complex, the excitation index varies from 1.17, in 1996, to 0.94, in 2005, indicative of a high excitation increasing with time.

As shown in Sect. 4.2.2, at the basis of the jet there is the indication of a new shock structure originating from the knot nearest to the protostar IRS5, the F-complex. In fact the stratification of the H_α and [SII] emission suggests the presence of a shock front, marked by the Balmer filament, and of the cooling zone just behind it, where the [SII] emission dominates as in the more evident terminal working surface (Fig. 4.14). The hypothesis of a new shock at the basis of the jet can be invoked only for the 2005 $H_\alpha-$ [SII] difference image. In fact in both 1996 and 1998 $H_\alpha-$ [SII] difference images there is no evidence of a shock front, i.e. H_α and [SII] stratification, at the basis of the jet. This result could be related to the activity of the protostar from which the jet originates, having a time scale of the order of few years and can also be related to the evidence, described above, that the excitation increases with time near the basis of the jet, where the F-complex is located and, more important, where the X-ray source has been discovered (Bally et al. 2003). In fact the location of the X-ray source from the HH 154 jet is very close to the position of the F-complex at the basis of the jet itself, i. e. to the knot with highest proper motion (knot F_2, see Tab. 4.3).

This is evident in Fig. 4.15, showing the X-ray source as detected with Chandra in 2005 with the optical knots contours superimposed (left panel), and the H_α emission observed with HST in 2005 with the X-ray contours superimposed.

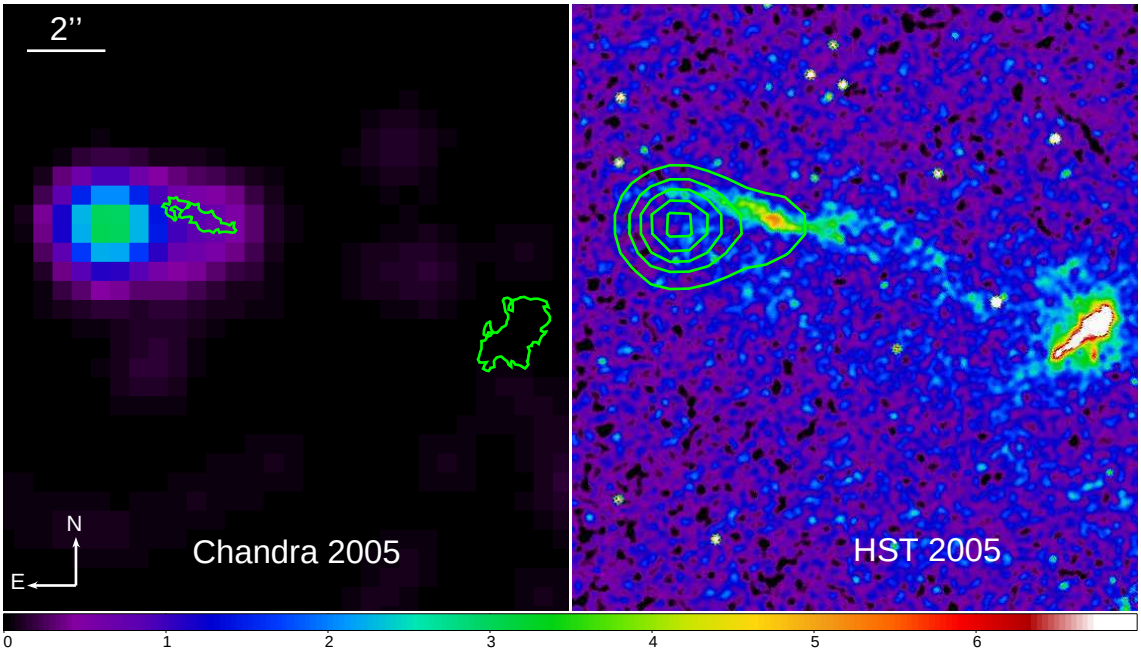

Figure 4.15: X-ray (left panel) and H_α (right panel) emission of the HH 154 jet as detected with Chandra and Hubble respectively. The contours of the optical knots and of the X-ray emission are superimposed on the X-ray and optical images respectively.

Table 4.5: Fluxes (erg cm^{-2} s^{-1}) and brightness of each knot within the jet and of the jet as a whole in H_α and [SII] filters for 1996, 1998 and 2005 HST observations. The accuracy is computed adding in quadrature the measurement error and the precision in the flux calibration (5%, following Holtzman et al. 1995). The two values correspond to H_α and [SII] filters, respectively. The values in brackets are not measured within a single aperture containing the two knots, but they are the sum of the values measured in single knots, and the corresponding accuracy is computed using the addition in quadrature rule.

Feature	flux H_α	flux $[SII]$	Source	Accuracy (%)	brightness (10^{-15}) H_α	brightness (10^{-15}) $[SII]$
D	1.3×10^{-14}	1.5×10^{-14}	HST 1996	5.3 - 5.9	4.8	3.7
D_2	3.5×10^{-16}	3.7×10^{-16}	HST 1996	9.6 - 10.0	2.3	1.9
E	4.1×10^{-16}	8.9×10^{-17}	HST 1996	8.8 - 19.6	2.6	1.8
F	1.8×10^{-15}	1.6×10^{-15}	HST 1996	6.1 - 6.7	3.1	2.7
F_2	1.8×10^{-16}	2.1×10^{-16}	HST 1996	11.2 - 12.1	3.0	1.9
$F + F_2$	(2.0×10^{-15})	(1.8×10^{-15})	HST 1996	(5.7) - (6.1)		
Σ_{Alljet}	(1.6×10^{-14})	(1.7×10^{-14})	HST 1996	(4.5) - (5.2)		
D	1.1×10^{-14}	1.4×10^{-14}	HST 1998	6.3 - 6.2	3.6	3.1
D_2	8.4×10^{-16}	3.4×10^{-16}	HST 1998	9.0 - 11.1	1.9	1.5
E	2.9×10^{-16}	4.4×10^{-17}	HST 1998	11.2 - 19.3	1.8	1.5
F	1.8×10^{-15}	-	HST 1998	7.2	2.7	-
F_2	4.5×10^{-16}	-	HST 1998	11.1	1.9	-
$F + F_2$	(2.2×10^{-15})	2.3×10^{-15}	HST 1998	(6.2) - 7.3		2.1
Σ_{Alljet}	(1.4×10^{-14})	(1.7×10^{-14})	HST 1998	(4.9) - (5.3)		
D	7.0×10^{-15}	1.1×10^{-14}	HST 2005	6.8 - 6.3	3.5	3.2
D_2	-	-	HST 2005	-	-	-
E	-	-	HST 2005	-	-	-
F	-	1.5×10^{-15}	HST 2005	7.3	-	2.6
F_2	-	2.1×10^{-16}	HST 2005	11.8	-	2.1
$F + F_2$	1.8×10^{-15}	(1.7×10^{-15})	HST 2005	6.9 - (6.5)	2.7	
Σ_{Alljet}	(8.8×10^{-15})	(1.3×10^{-14})	HST 2005	(5.6) - (5.5)		

Table 4.6: The excitation index, defined as the ratio of [SII] to H_α flux (Raga et al. 1996), for the knots within the HH 154 jet for the three epochs, 1996, 1998 and 2005. The values in brackets are not measured within a single aperture containing the two knots, but they are the sum of the values measured in single knots.

Feature	Year	[SII]/H_α	Accuracy (%)
D	1996	1.15	7.9
	1998	1.27	8.8
	2005	1.57	9.2
D_2	1996	1.06	13.9
	1998	0.40	14.3
	2005	-	-
E	1996	0.22	21.5
	1998	0.15	22.3
	2005	-	-
F	1996	0.89	9.1
	1998	-	-
	2005	-	-
F_2	1996	1.17	16.5
	1998	-	-
	2005	-	-
$F+F_2$	1996	(0.90)	
	1998	(1.00)	
	2005	(0.94)	

Chapter 5

Future perspectives

In order to investigate the physical mechanisms governing the X-ray emission observed in HH objects, I developed a hydrodynamic numerical model (including thermal conduction and radiative losses) of a continuous supersonic protostellar jet propagating through an uniform medium (Bonito et al. 2004, 2007, see Chapter 2). Such a model explains the detected X-ray source as the emission from the shock formed by the interaction between the jet and the ambient medium. The hydrodynamic numerical modeling indicates that the X-ray emitting shock should move at a speed of about 500 km/s, consistent with the velocity of the observed extended X-ray component (see Chapter 3) and with the observed velocity of recombination emission lines (see Chapter 4). Albeit this moving shock model answers many of the previous questions, the physical scenario suggested by the observations seems more complex than expected. While the presence of the transient X-ray source rules out simple models such as scattered stellar X-ray light (proposed by Bally et al. 2003 and discussed in Chapter 2), the complex morphology present in the 2005 observation raises more questions than it does answer. The observed evolving morphology is not compatible with any of the simple models proposed to date.

In this Chapter I briefly discuss new configurations of the jet/ambient system which may describe satisfactorily the observations. In particular, as a follow up of my work, I have started developing new numerical models concerning the interaction between a continuous supersonic jet and an inhomogeneous ambient medium (see Sect. 5.1), the auto-interaction between "blobs" ejected at different epochs, i. e. the scenario of a pulsed jet (see Sect. 5.2), and the case of a protostellar jet collimated by a so-called de Laval nozzle where standing shocks can develop at several distance from the driving source (see Sect. 5.3).

Table 5.1: Summary of the initial physical parameters characterizing the model of a protostellar jet traveling through an interstellar cloud: jet Mach number, M, initial jet velocity, $v_{\rm j}$, jet temperature, $T_{\rm j}$, jet density, $n_{\rm j}$, ambient-to-jet density contrast, $\nu_{\rm a}$, cloud-to-jet density contrast, $\nu_{\rm b}$.

M	$v_{\rm j}$ [km s^{-1}]	$n_{\rm j}$	$T_{\rm j}$ [K]	$\nu_{\rm a}$	$\nu_{\rm b}$
30	1400	500	10^4	0.1	10

5.1 Jet-cloud

The rapid variation in space of the circumstellar absorption (Fridlund et al. 2005) indicates that the ambient medium is highly inhomogeneous. In order to take into account this experimental result, as a follow up of my first analysis (Bonito et al. 2004, 2007), recently I modeled another, probably more appropriate, scenario of the interaction between a supersonic protostellar jet traveling through an inhomogeneous surrounding medium. As part of this effort, I am evaluating the effect of inhomogeneities in the jet propagation. To this end I developed a hydrodynamic model of a protostellar jet traveling through an interstellar inhomogeneity, described as a dense spherical cloud ten times denser than the protostellar jet and 100 times denser than the ambient medium.

Fig. 5.1 shows the bi-dimensional density (right half-panel) and temperature (left half-panel) distributions after 6, 8 and 10 years since the beginning of the jet-ambient interaction. It is evident how the presence of the dense cloud affects the expansion of the jet, which appears quite collimated inside the cloud, even in this case in which any magnetic field has been neglected.

In Tab. 5.1, I resume the relevant initial physical parameters of the jet/cloud system. From the model, I found that the X-ray emission associated to the jet consists of an almost stationary source at the base of the jet/cloud system and a faster component at the head of the jet with velocity of about 500 km/s (computed from my numerical model), consistent with the observations of HH 154 (Favata, Bonito et al. 2006).

Comparing the X-ray emission synthesized from the model (Fig. 5.2) with observations (Fig. 3.1), I conclude that the scenario of a jet/cloud interaction could reproduce the complex morphology observed in the X-ray source of HH 154, with an almost stationary source at the base of the jet/cloud system and a faster component at the head of the jet. However this model fails to reproduce the X-ray luminosity of the two sources. In fact I derive that the brighter source is the moving one, while the fainter is located at the basis of the jet. This result is not in agreement with the observations of the X-ray emission from HH 154, where the brightest source is the stationary one at the basis of the jet.

These results are promising and show that the basic physics on which my

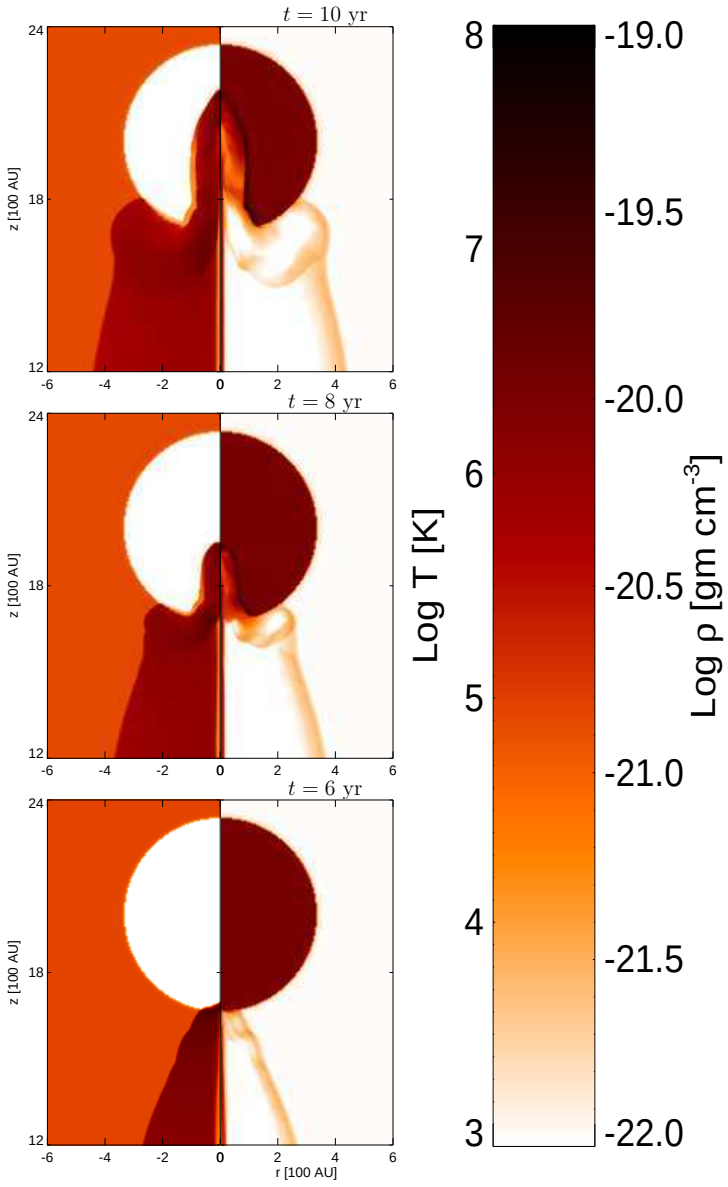

Figure 5.1: Bi-dimensional density (right half-panels) and temperature (left half-panels) distributions of the jet/ambient interaction after 6, 8 and 10 years.

models are based could reproduce the observations. A full exploration of the parameter space is in order. I am now improving my model by considering more realistic cases among which the interaction between a pulsed jet, described in the next Section, with interstellar inhomogeneities.

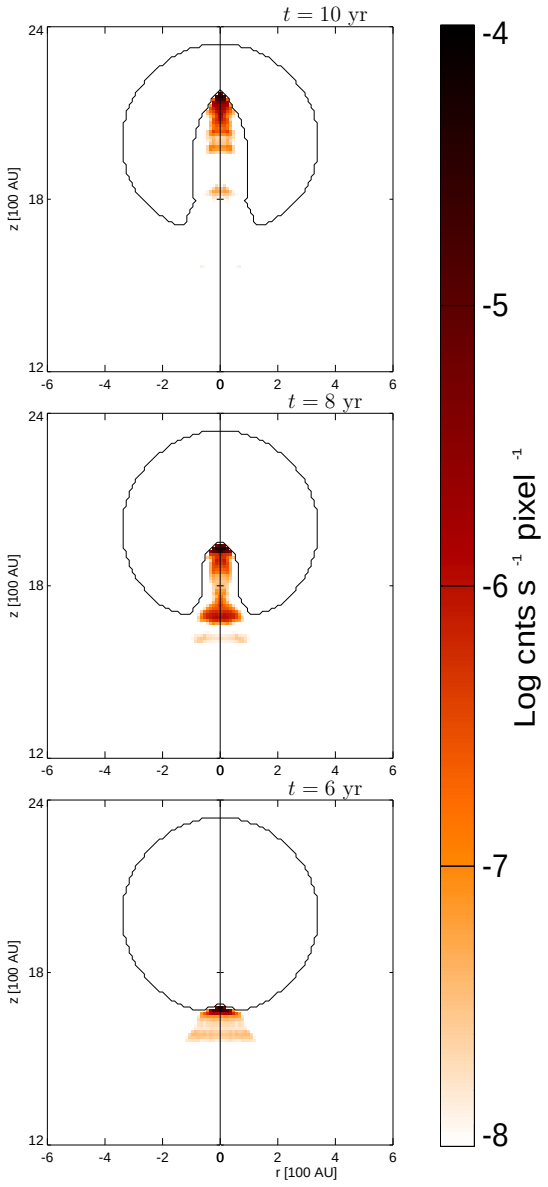

Figure 5.2: X-ray emission as would be observed with Chandra/ACIS-I, synthesized from my numerical model of the jet/cloud interaction.

5.2 Jet pulsed

Another possible scenario that may describe the observations is the case of a pulsed jet. To this end I developed a two-dimensional hydrodynamic model of pulsed jet which account for the thermal conduction effects, solving the time-dependent fluid equations of mass, momentum, and energy conservation with the FLASH code (Fryxell et al. 2000). The jet consists of several bullets, each

modeled as an impulse 0.5 yr long, ejected with a rate 1 blob/yr with a random velocity (with direction along the z axis).

Following the observations of HH 154 (Fridlund & Liseau 1998) and my previous model results (Bonito et al. 2004, 2007), I impose an initial blob temperature $T_j = 10^4$ K and an ambient medium with density $n_a = 5000$ cm^{-3} and temperature $T_a = T_j/10$.

From the simulations I synthesized the X-ray emission as it would be detected with Chandra/ACIS-I. In Fig. 5.3, I show the X-ray source synthesized from my model for three different evolutionary stages.

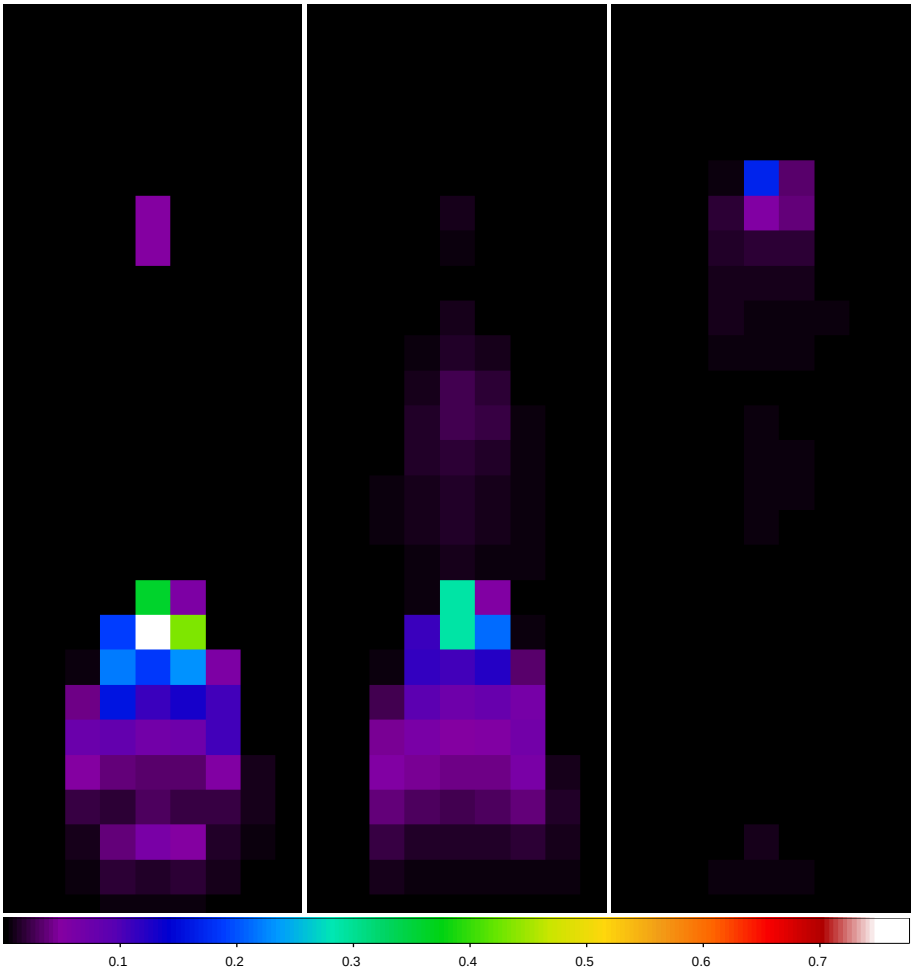

Figure 5.3: The X-ray emission as it would be detected with Chandra/ACIS-I, synthesized from the numerical model of a pulsed jet for three different evolutionary stages.

In Fig. 5.4, I compare the morphology of X-ray emission derived at a selected time with the model (upper panel; Bonito et al. 2008, in preparation) with the observations of HH 154 in 2005 (lower panel; Favata, Bonito et al. 2006) put on the same spatial scale. The model of a protostellar jet with variable initial velocity reproduces a multi-structures morphology as that observed in the X-ray

source from HH 154.

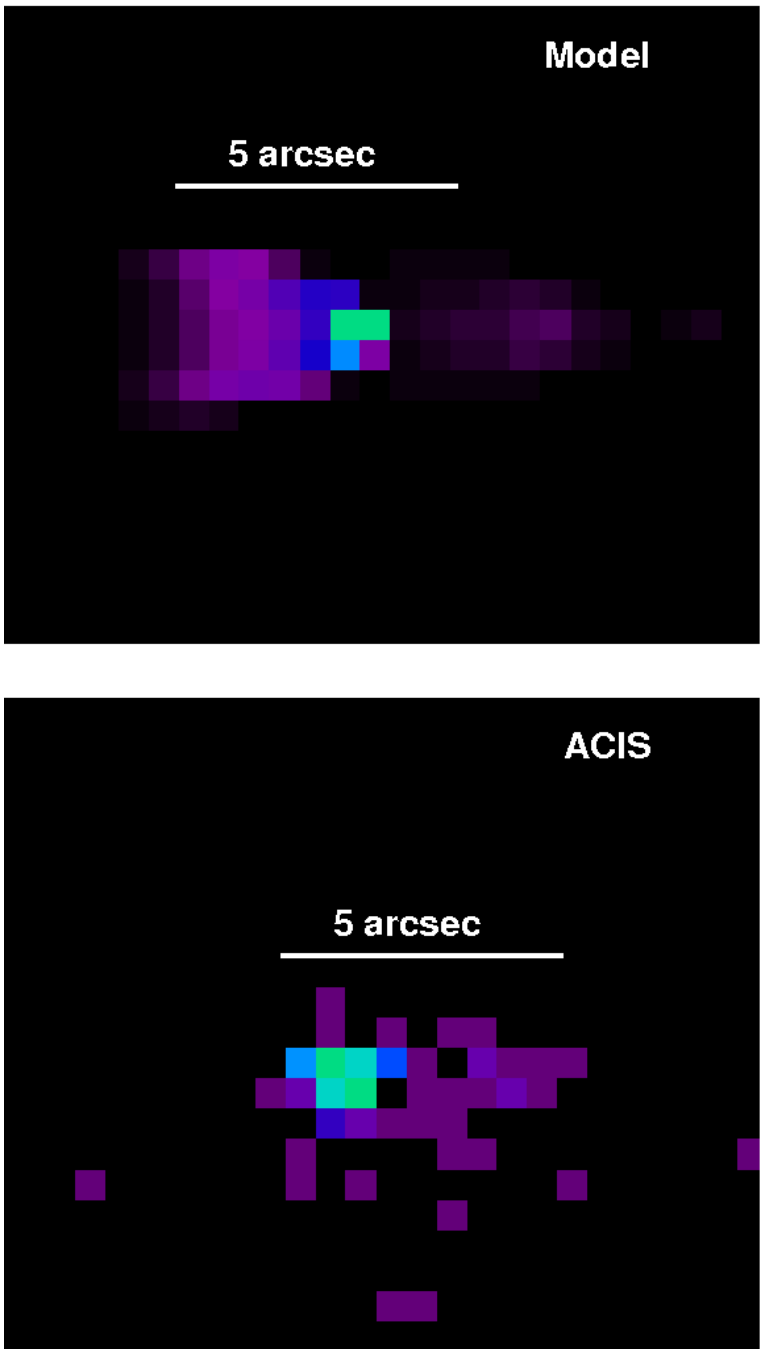

Figure 5.4: Comparison between the observation of the X-ray source from HH 154 (lower panel) and the morphology of the X-ray emission as synthesized from the numerical model of the pulsed jet.

Fig. 5.5 shows the distribution of the total emission along the jet axis integrated over the time. I found that most of the X-ray emission originating from the jet is located at its base at distances from the protostar below 1500 AU. This

result is consistent with the fact that the X-ray emission detected in protostellar jets is located at their base.

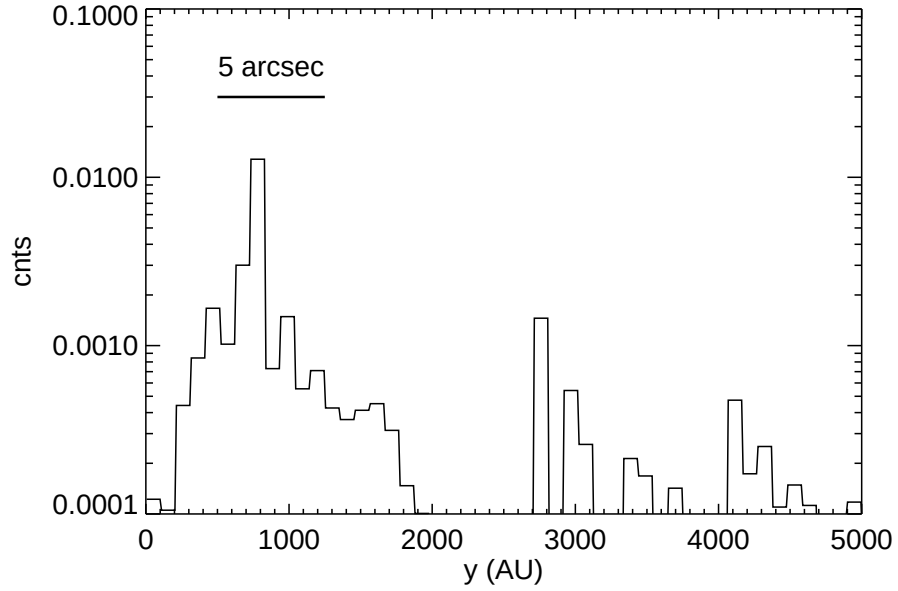

Figure 5.5: Distribution of the total emission along the jet axis integrated over time in the pulsed jet model.

New observations of the X-ray emission of protostellar jets with Chandra could be used to validate the pulsed jet model. The distance between the X-ray emitting knots and the protostar may be used as a powerful diagnostic tool. In fact the comparison between the observations and the model predictions could allow us to constrain the physical configuration and the parameters of a protostellar jet which can reproduce the observed emission and its evolution.

5.3 de Laval nozzle

As explained above, one possible explanation (as discussed in Favata, Bonito et al. 2006) could be related with episodic ejection of plasma bullets from the jet's source, which first glow brighter by interaction with a circumstellar "shell" and then grow fainter as they travel through the thinning medium (in this scheme the transient source would be a moving bullet). In this framework the bright stationary source indicates the location of the shell. This scenario however suffers from the ad hoc assumption that bullets were hitting the shell both in 2001 and 2005 to explain the stationary source. The observed morphology could however better explained with a less ad hoc model, in particular one based on the so-called de Laval nozzles. These nozzles are based on the acceleration of an initially subsonic plasma flow to supersonic speeds through a narrowing "tube", which later

opens allowing the flow to escape. At the exit of the nozzle, a strong stationary shock may form downstream of it, and weaker and weaker shocks (related to reflections from the tube walls) form further downstream in the escaping plasma, as shown in Fig. 5.6.

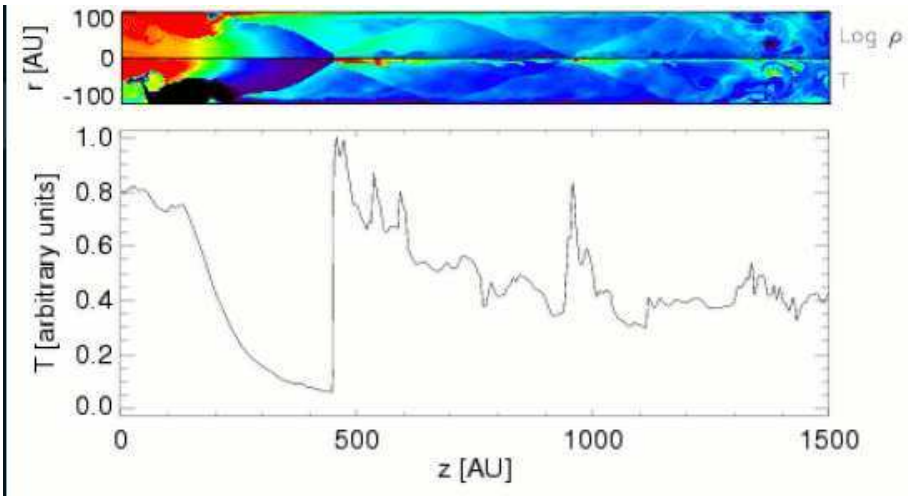

Figure 5.6: A simple hydrodynamic simulation of a jet accelerated in a de Laval nozzle. Density and temperature are shown in the top image, the central temperature profile in the bottom graph, 5 years after the initial acceleration. z is the spatial coordinate along the jet. The shock at the acceleration site is well visible near the jet origin's, with the first shock is at about 500 AU in this mode, followed by a weaker one at about 900 AU. A third shock is forming at about 1400 AU, and it fully develops in the simulation about 5 years later. The absolute scale for the temperature values depends on the jet initial parameters, in particular speed and density; the emission measure and temperature observed for HH154 can be reproduced with values for the jet's speed and density compatible with the ones determined observationally (few hundreds km/s for the speed, $10^2 - 10^4$ cm^{-3} for the density). Measuring the temperatures for a number of shocks will validate the de Laval model and allow determination of the key parameters.

If the de Laval nozzle hypothesis is correct, then in HH 154 the stationary X-ray source (located at some tens of AU from the protostars) marks the location of the first post-acceleration shock (at about 500 AU from the origin in Fig. 5.6). The nozzle's site likely hidden from view by the large absorption near the protostar, and the transient source observed in 2005 is the second post-acceleration shock, fainter and cooler. The downstream shocks will likely vary in intensity with time (and perhaps in position) due to e.g. changes in the incoming flow speed or in the nozzle shape (e.g. due to changing geometry of the magnetic field and of the confining matter).

We have built a simple hydrodynamic model of jet acceleration through a de Laval nozzle (shown in Fig. 5.6), with parameters explaining the X-ray emission in HH154, and I am currently working to implement a detailed magneto-hydrodynamic modeling of the observed process. This model makes specific pre-

dictions about the characteristics of the X-ray emission and in particular about its temperature (for both the strong shock in the nozzle and the weaker shocks downstream, as shown in the bottom panel of Fig. 5.6). A study of the spectrum of the X-ray sources, and a search for the weaker shocks expected further downstream will test whether the de Laval nozzle mechanism is at work in HH154 and constrain the models, allowing us to understand the physics of jet acceleration. Indications of at least two more shocks being present further downstream comes from extant shallow [OIII] HST observations showing two emission knots (knots F and D, see Fridlund et al. 2005) indicative of high temperature, excited plasma.

Unfortunately the statistics of our 2005 observation are too poor to address the above questions. While the stronger, stationary component has sufficient statistics to allow a crude spectrum to be extracted and thus a temperature to be measured, the number of photons detected from the transient component (12 counts) is simply too small to allow any meaningful analysis, and thus to constrain the theoretical models. Also, the expected weaker downstream shocks would not produce sufficient flux to be visible in X-rays. A deep observation (400 ks or even more) of the HH 154 jet with Chandra could provide spectra for both the stationary and the transient X-ray source, and have sufficient sensitivity to detect (if present) the downstream shock, allowing us to determine whether it indeed is a de Laval nozzle accelerating the jet and to determine its characteristics. This in turn would provide a clear strong framework for the acceleration of jets in YSOs, as well as perhaps for jet acceleration in general.

Chapter 6

Summary and conclusions

In this thesis I report on the investigation of the physical mechanisms which can give rise to X-ray emission from protostellar jets consistent with observations of the last few years. In order to explain the experimental results with an unambiguous theory, I focused on the development of a detailed numerical model describing the interaction between a supersonic protostellar jet and the ambient medium. The model's predictions can then be compared with new observations of protostellar jets in order to verify or even improve the proposed model itself.

In this framework, I performed detailed numerical models of the jet/ambient system and derived the main physical properties of protostellar jets. Then we proposed a joint Chandra (X-rays) and Hubble (optical) observations of the nearest protostellar jet from which X-ray emission has been detected (HH 154) to verify my model. The comparison between the observations and the numerical model shows that on one hand my model is very promising in explaining the main characteristics of protostellar jets, and on the other hand a more complex scenario is necessary to explain the new features observed.

6.1 Numerical model of the jet/ambient system

Prompted by the recent detection of X-ray emission from protostellar jets, I started a project voted to the investigation of the physical mechanisms which can give rise to emission consistent with observations. In fact the physics involved in this phenomenon is still unclear. I aim at explaining the X-ray emission from protostellar jets by performing detailed numerical simulations of the interaction between a supersonic jet and the ambient medium. As a first step, I developed a simple model of a continuous jet ramming through a denser homogeneous ambient medium. The results of this first model were presented in Bonito et al. (2004). As a follow up, I performed a wide exploration of the space of the parameters which mainly influence the evolution of the jet/ambient system. In Bonito et al. (2007)

I discuss the main results of these models: the morphological evolution of the main components of the jet/ambient system, e.g. the cocoon surrounding the jet itself or the shock front forming at its head; the thermal stability of the structures within the jet where the X-ray emission originates; the velocity of the shock front, forming where the supersonic jet interacts with the unperturbed ambient medium, and the comparison between this value and the initial jet velocity; the synthesis of the X-ray spectra, derived from the emission measure distribution as a function of the temperature, assuming realistic value for the interstellar absorption and the instrumental response. All these topics derived from our numerical models are compared with observations in the X-ray band of the nearest protostellar jet from which X-ray emission has been detected (HH 154, observed with both XMM-Newton and Chandra satellites). One of the main results of my analysis is that the exploration of the parameters space allows us to constrain the physical configuration of the jet/ambient system which reproduces the observations. In fact I derived that only a narrow range of initial parameters leads to emission in good agreement with XMM-Newton and Chandra data. In particular the physical characteristics (velocity, luminosity, spectra of the X-ray source) of the HH 154 jet is well described with the scenario of a "light jet" (i.e. a jet less dense than the ambient medium) with an initial velocity of about 1400 km/s and a corresponding shock velocity of about 500 km/s. These two aspects (the light jet case and the high, i.e. $>$ 1000 km/s, initial velocity) have been controversial until now, but my model demonstrates unambiguously that only the scenario of an initially high velocity light jet can reproduce the observations of HH 154. Furthermore optical observations of the same object confirm the scenario of a jet traveling through a denser ambient medium, as discussed in more details in Chapter 4 and in Bonito et al. (2008).

The results of my model (Bonito et al. 2007) are very promising in fact the main physical properties of the jet's emission are consistent with observations. This shows that the basic physics explored in Bonito et al. (2007) are well established. However this first simple model does not reproduce the complex morphology observed in the 2005 X-rays data of HH 154 discussed in Favata, Bonito et al. (2006). To this end I aim at exploring new physical configurations of the jet/ambient system which can reproduce the "knotty" structure of the X-ray source from HH 154. In more details, I have started developing the numerical simulations of the interaction between a continuous supersonic jet colliding with inhomogeneities (e.g. a dense cloud) in the surrounding medium and the auto-interactions of a pulsed jet, which consists of several bullets ejected from the central source with random velocity in an homogeneous medium. The more general case of a pulsed jet traveling through an inhomogeneous surrounding medium will be explored as a follow up of these two models.

6.2 X-ray emission from HH 154

The numerical model discussed in the last section (see also Bonito et al. 2004, 2007) leads to accurate predictions on the proper motion, variability and spectral behaviour of the X-ray source detected in the HH 154 protostellar jet. In order to verify or improve instead the model here discussed, we proposed a joint optical and X-ray observations of the HH 154 jet to be directly compared with the model's results. The X-ray observations have been collected with Chandra/ACIS-I so as to exploit the high spatial resolution of this instrument which allows to pinpoint the position of the point-like X-ray source observed. The HH 154 jet has been detected with Chandra in 2005, almost 4 years after the first observation performed with the same instrument in 2001, and the comparison between these two sets of data is discussed in Favata, Bonito et al. (2006).

The main surprising result is that the morphology of the X-ray source detected in 2005 is more complex than expected. In fact it consists of two components: a bright stationary (over the 4 years time basis of observations) component at the basis of the jet and a fainter elongated component showing a detectable proper motion consistent with the scenario of a shock front propagating away from the central source at a velocity of about 500 km/s. The luminosity and the shock speed are almost consistent with the numerical model's predictions of Bonito et al. (2004, 2007). However, as discussed in the last section, although the basic physics of the model there discussed reproduce the main physical characteristics of the jet/ambient system, an improvement of that simple model is necessary in order to explain the morphology observed.

Furthermore it would be very interesting to obtain new deeper observations of the same jet with Chandra so as to perform spatially resolved spectral analysis of the two components of the X-ray source. In fact the poor statistics achieved with our present data prevent us from properly explain the spectral behaviour of the X-ray emission.

6.3 Optical emission from HH 154

The proposal of a joint optical and X-ray observation of the HH 154 jet aiming at verifying my model's predictions discussed in Bonito et al. (2004, 2007) was performed using the Hubble Space Telescope (HST) in the optical band. The HST telescope has been chosen for its high angular resolution which allow us to resolve the small structures within the shocks in the jet. Our aim is to study the evolution of the sub-structures observed within the jet, i.e. its characteristic "knotty" morphology, computing in particular their proper motion, their energetics and dynamics as well as their auto-interactions. To this end I developed a new method of analysis of the HST data, which leads for the first time to a quantitative and

reproducible definition of the contours on each knots in protostellar jets. Using this well tested method, it is possible to obtain a consistent analysis for different sets of data (e.g. collected at different epochs and in different filters, as in the case described in this thesis). I analyzed the optical emission from the HH 154 jet in both the H_α and [SII] filters in three different epochs (1996, 1998, 2005)[1]. First of all I examined the variability in the morphology of the substructures within the protostellar jet and of the jet itself as a whole. Then I analyzed in more details the stratification of the emission observed within the single knot in the jet, marked by the different spatial location of the H_α and [SII] in each structure identified as a shock front. Once a unambiguous definition of the position of the knots in the jet has been established using my new method, I was able to compute the proper motion of each structure within the jet and even of the smallest spot observed within the brightest knot, the D knot at the head of the jet. The identification of the knots in the jet allow us also to evaluate the total emission of the structure so as to estimate the flux and its variation over almost 10 years.

One of the main result of this detailed analysis of the optical emission from the HH 154 jet is that there is strong indication for the jet to be a "light jet", i.e. a jet less dense than the surrounding medium. This scenario, although being still a controversial topic in the framework of the protostellar jets, seems to be the more realistic for the case of HH 154 and is consistent with the model's prediction discussed by Bonito et al. (2004, 2007). Even the value and variability of the velocity of the knots are consistent with the model which I developed. Another result derived from the analysis of the shock stratification observed in some knots within the jet is the indication of a new shock structure originating from the knot nearest to the protostar IRS5, the F-complex, located where the X-ray source has been discovered. Taking into account this evidence we are strongly suggested to identify the highest velocity component found at the basis of the jet (knot F_2) with a region very close to the X-ray source, i.e. $(0.5 - 1)''$ from the radio position of the IRS5 protostar. In this way it is possible to link for the first time the active optical emitting region, located at the basis of the jet near the protostellar source, with the recently discovered phenomenon of the X-ray emission discovered in protostellar jets.

6.4 Future perspectives

My work is based on the multi-wavelength and multi-epoch analysis of the emission from protostellar jets, through both modeling and observations. This leads

[1]This part of my work was performed at the European Space Agency (ESA)-ESTEC in Noordwijk (The Netherland) in the framework of a scientific collaboration with Dr. Fabio Favata and Dr. Malcolm Fridlund (July 2005, April 2006, July 2007).

to one of the more complete approach to the analysis of the physical characteristics of protostellar jets. The numerical model that I developed (Chapter 2, see also Bonito et al. 2004, 2007) makes detailed predictions which have been used as the starting point of a program of observations in both X-ray and optical band, through the accepted proposal for a joint observation with Chandra (X-ray telescope) and Hubble (optical space telescope). These observations verify the model's predictions, as discussed in this thesis. Furthermore the new results obtained from these observations (as the complex morphology detected int he X-ray source from HH 154, discussed in Chapter 3 and in Favata, Bonito et al. 2006) open the way for new scenarios of the physical interaction between protostellar jets and their environments to be explored. Prompted by these unexpected and interesting results, I have started developing new numerical models (described in Chapter 5) in order to explain the observations and to infer a more complete description of the physics of the protostellar jets.

Appendix A

The FLASH code

FLASH (Fryxell et al. 2000) is a numerical code for astrophysical plasma which has been developed mainly in the *FLASH Center* of the Chicago University.

The core of FLASH is based on a directionally split Piecewise Parabolic Method (PPM) solver to handle compressible flows with shocks (Colella & Woodward 1984). FLASH uses the PARAMESH library to handle adaptive mesh refinement (MacNeice et al. 2000) and the Message-Passing Interface (MPI) library to achieve parallelization. The FLASH code is modular, adaptive and parallel. It is modular, i.e. it is possible to modify the initial and boundary conditions, to chose the algorithm and to add several physical effects in a very simple way. It is adaptive because it uses the PARAMESH library to handle adaptive mesh refinement (MacNeice et al. 2000), which allows to increase the spatial resolution only in the portion of interest of the entire computational domain. It is parallel, in fact it uses the Message-Passing Interface (MPI) library to achieve parallelization.

A.1 FLASH code architecture

The FLASH code consists of several modules which can be combined in order to use the code for a wide variety of physical topics. An abstract representation of the FLASH architecture appears in Fig. A.1. Each box in this figure represents a component (FLASH module).

In the following sections I will describe the main modules used in this thesis.

A.1.1 Driver module

The driver module controls the initialization (i. e. the choice of some initial parameters), the evolution of the FLASH simulations, and the production of output files.

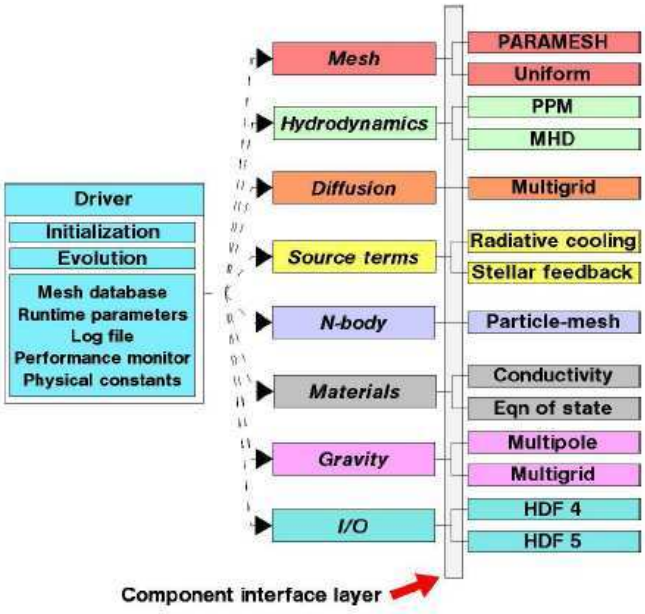

Figure A.1: Scheme of the FLASH modules.

A.1.2 I/O module

The main task of this module is the production of the output files, both checkpoint and plot files. A checkpoint file contains all the information needed to restart the simulation. The data is stored at the same precision (8-byte reals) as it is carried in the code and includes all of the variables. A plotfile contains all the information needed to interpret the tree structure maintained by FLASH and includes a user-defined subset of the variables. Furthermore, the data is stored at reduced precision to conserve space.

There are several parameters that control the frequency of output, the type of output, and the name of the output files.

Furthermore this module generates the log files, i.e. files containing all the informations on the computing performance and on the values of each parameter describing the physical system analyzed.

A.1.3 Mesh module

The mesh module is responsible for maintaining the grid used to discretize the simulation. It divides the computational domain into one or more sub-domains or blocks, each of which contains a number of computational zones (nxb in the x-direction, nyb in the y-direction, and nzb in the z-direction). A perimeter of guardcells of width nguard guard cells surrounds each block of data, providing it with the data from the neighboring blocks or boundary conditions. The mesh

module also manages the coordinate information for each block.

The size of the computational domain in physical units is specified at runtime through the (xmin, xmax), (ymin, ymax), and (zmin, zmax) runtime parameters.

The mesh is initially decomposed into $Nblockx \times Nblocky \times Nblockz$ blocks, each containing $nxb \times nyb \times nzb$ cells. For the adaptive mesh, these blocks can then be further refined.

Fig. A.2 shows a single 2-D AMR block. Each block consist of the interior zones (shaded in Fig. A.2) and the perimeter of guard cells. The number of guard cells in each direction can be chosen by the user through the parameter *nguard*.

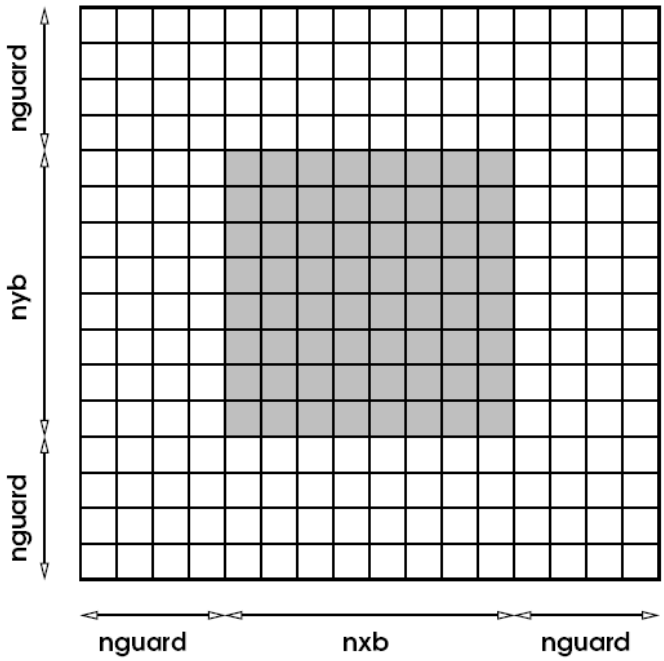

Figure A.2: Structure of a single block of the mesh. The interior zones and the perimeter of guard cells are indicated.

The geometry for a particular problem is set at runtime through the geometry runtime parameter, which can take a value of "cartesian", "spherical", "cylindrical", or "polar". Together with the dimensionality of the problem, this serves to completely define the nature of the problem's coordinate axes (Tab. A.3). Note that not all modules or meshes support all the geometries.

Adaptive mesh

Many scientific modeling challenges attempt to simulate processes that span very large ranges in spatial scale. Uniform meshes that can be run on the largest computers do not provide sufficient resolution. Larger dynamic ranges in spatial

name	dimensionality	axisymmetric	x-coord	y-coord	x-coord
cartesian	1	n	x		
cartesian	2	n	x	y	
cartesian	3	n	x	y	z
cylindrical	2	y	r	z	
cylindrical	3	n	r	z	ϕ
spherical	1	y	r		
spherical	2	y	r	θ	
spherical	3	n	r	θ	ϕ
polar	1	y	r		
polar	2	n	r	ϕ	

Figure A.3: Different geometry types supported by the FLASH code.

resolution are required, and adaptive mesh refinement (AMR) techniques are used for this scope.

The FLASH code uses a package known as PARAMESH (Olson et al. 1999) for the parallelization and adaptive mesh refinement (AMR). PARAMESH consists of a suite of subroutines which handle refinement/derefinement, distribution of work to processors, guard cell filling, and flux conservation.

PARAMESH uses a block-structured adaptive mesh refinement scheme.

In block-structured AMR, the fundamental data structure is a block of cells arranged in a logically Cartesian fashion. Each cell can be specified using a block identifier (processor number and local block number) and a coordinate triple (i; j; k), where i = 1...nxb, j = 1...nyb, and k = 1...nzb refer to the x-, y-, and z-directions, respectively. The complete computational grid consists of a collection of blocks with different physical cell sizes, which are related to each other in a hierarchical fashion using a tree data structure. The blocks at the root of the tree have the largest cells, while their children have smaller cells and are said to be refined. Three rules govern the establishment of refined child blocks in PARAMESH. First, a refined child block must be one-half as large as its parent block in each spatial dimension. Second, a block's children must be nested; i.e., the child blocks must fit within their parent block and cannot overlap one another, and the complete set of children of a block must fill its volume. Thus, in d dimensions a given block has either zero or 2d children. Third, blocks which share a common border may not differ from each other by more than one level of refinement.

A simple domain is shown in Fig. A.4).

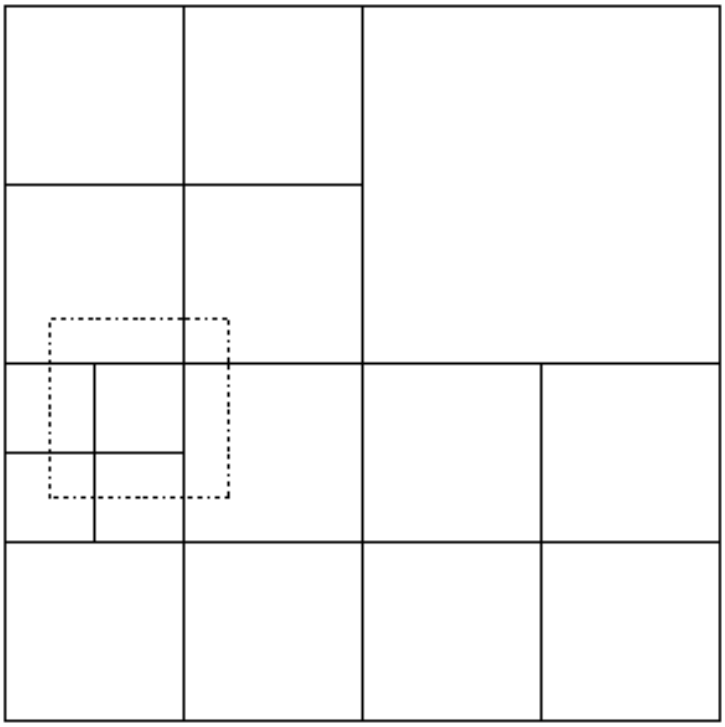

Figure A.4: A simple computational domain showing varying levels of refinement. The dotted lines around one block outline the guard cells for that block.

Each block contains $nxb \times nyb \times nzb$ interior cells and a set of guard cells (Fig. A.2). The guard cells contain boundary information needed to update the interior cells. These can be obtained from physically neighboring blocks, externally specified boundary conditions, or both. The number of guard cells needed depends upon the interpolation schemes and the differencing stencils used by the various physics modules (usually hydrodynamics); for the explicit PPM algorithm distributed with FLASH, four guard cells are needed in each direction, as illustrated in Fig. A.2.

PARAMESH handles the filling of guard cells with information from other blocks or a user-specified external boundary routine. If a block's neighbor has the same level of refinement, PARAMESH fills its guard cells using a direct copy from the neighbor's interior cells. If the neighbor has a different level of refinement, the neighbor's interior cells are used to interpolate guard cell values for the block. If the block and its neighbor are stored in the memory of different processors, PARAMESH handles the appropriate parallel communication (blocks are not split between processors).

At jumps in refinement, the fluxes of mass, momentum, energy (total and internal), and species density in the fine cells across boundary cell faces are summed

and passed to their parent, which will be at the same level of refinement as the parent's neighboring cell because PARAMESH limits the jumps in refinement to one level between blocks. The flux in the parent that was computed by the more accurate fine zones is taken as the correct flux through the interface and is passed to the corresponding coarse face on the neighboring block (see Fig. A.5).

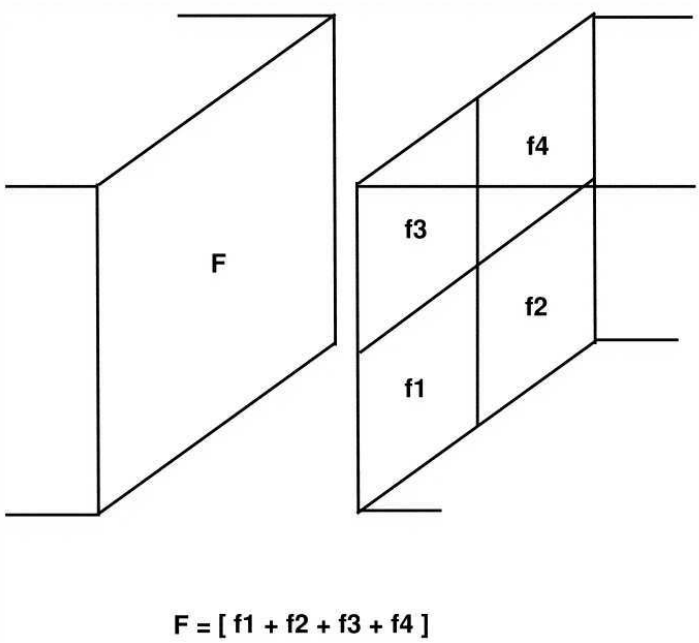

Figure A.5: Flux conservation at a jump in refinement. The fluxes in the fine cells are added and replace the coarse cell flux (F)

The refinement criterion used by PARAMESH is adapted from Löhner (1987). Löhner's estimator is a modified second derivative, normalized by the average of the gradient over one computational cell. In one dimension on a uniform mesh, it is given by

$$E_i = \frac{|u_{i+1} - 2u_i + u_{i-1}|}{|u_{i+1} - u_i| + |u_i - u_{i-1}| + \epsilon(|u_{i+1}| - 2|u_i| + |u_{i+1}|)} \tag{A.1}$$

where u_i is the refinement test variable's value in the i-th cell. The last term in the denominator of this expression acts as a filter, preventing refinement of small ripples. The constant ϵ can be chosen properly by the user.

Spatial resolution in the adaptive mesh

The spatial resolution which can be achieved with the adaptive mesh depends on the choice of two main initial parameters: $lrefine\_min$ and $lrefine\_max$.

The initial computational domain is divided into $nblockx \times 2^{lrefine\_min}$ block in the x direction and the same is made in each directions. This corresponds to the minimum spatial resolution. The maximum spatial resolution, otherwise, is achieved when the computational domain is divided into $nblockx \times 2^{lrefine\_max}$ blocks. In particular if the domain extends from $xmin$ to $xmax$, in the x direction, divided in $nblockx$ each containing nxb cells, the maximum spatial resolution achieved is

$$\frac{xmax - xmin}{nblockx \times nxb \times 2^{lrefine\_max-1}} \tag{A.2}$$

A.1.4 Boundary conditions

The user can chose several boundary conditions as: reflect, i. e. non-penetrating boundaries, zero-gradient with transverse velocity reflected; outflow, i. e.zero-gradient boundary conditions which allows shocks to leave the domain; user, which allows to chose user-defined boundary conditions.

A.1.5 Hydro module

The hydro module solves Euler's equations for mass, momentum and energy conservation for compressible gas dynamics in one, two, or three spatial dimensions

$$\frac{\partial \rho}{\partial t} + \nabla \cdot \rho \mathbf{v} = 0 \tag{A.3}$$

$$\frac{\partial \rho \mathbf{v}}{\partial t} + \nabla \cdot \rho \mathbf{v}\mathbf{v} + \nabla p = 0 \tag{A.4}$$

$$\frac{\partial \rho E}{\partial t} + \nabla \cdot (\rho E + p)\mathbf{v} = 0 \tag{A.5}$$

where

$$E = \epsilon + \frac{1}{2}|\mathbf{v}|^2 \tag{A.6}$$

is the total energy of the plasma and ϵ is the internal energy per unit mass, ρ is the fluid density, $\mathbf{v}$ is the fluid velocity. The pressure is obtained from the energy and density using the equation of state. For the case of an ideal gas equation of state, the pressure is given by

$$p = (\gamma - 1)\rho\epsilon \ , \tag{A.7}$$

where γ is the ratio of specific heats.

The piecewise-parabolic method (PPM)

The equations A.3 - A.5 are solved by using the Piecewise-Parabolic Method (PPM; Woodward & Colella 1984). It is a higher-order version of the method developed by Godunov (Godunov 1959). FLASH implements the Direct Eulerian version of PPM.

In order to solve the Euler's equations for mass, momentum and energy conservation for compressible gas dynamics by numeric method, the finite difference scheme on a discrete numerical grid is used. In particular the solution at time $t + \Delta t$ can be obtained once the solution at time t and the time-averaged values of the parameters (as the velocity) across the cell are known.

Time-advanced fluxes at cell boundaries are computed using the numerical solution to Riemann's shock tube problem[1] at each boundary.

Since the value of each variable in each cell is assumed to be constant, Godunov's method is limited to first-order accuracy in both space and time. PPM improves on Godunov's method by representing the flow variables with piecewise-parabolic functions.

A.1.6 Materials module

FLASH has the ability to track multiple fluids, each of which can have its own properties. The materials module handles these, as well as other things like EOS, composition, and conductivities.

Equation Of State (EOS)

In a simple 2-D numerical simulation the equation of state (EOS) can be used up to 10^9 times. This equation is of fundamental importance in order to solve the Euler's equations for mass, momentum and energy conservation for compressible gas dynamics (discussed in Sect. A.1.5) describing the system to be analyzed. In particular the sub-module *gamma* of the EOS module allows to solve the ideal gas equation of state (see Sect. A.1.5).

Thermal conduction

This module allows to take into account the thermal conduction effects on the dynamics of the system analyzed. In particular it is possible to modify the energy equation in order to account for the thermal conduction in the following way

$$\frac{\partial \rho E}{\partial t} + \nabla \cdot (\rho E + P)\mathbf{v} = \nabla \cdot (\sigma(X_i, \rho, T)\nabla T) \tag{A.8}$$

[1]The Riemann problem solves the interaction between two different zone of a fluid with different thermodynamic parameters and which are initially separated by a membrane which is removed.

where σ is the thermal conductivity. In more details, this module allows to use both the Spitzer regime Spitzer (1962), and the saturated regime (Cowie & McKee 1977).

Following Dalton & Balbus (1993), the FLASH code uses an interpolation expression for the thermal conductive flux of the form

$$q = \left(\frac{1}{q_{\rm spi}} + \frac{1}{q_{\rm sat}} \right)^{-1} \ , \tag{A.9}$$

which allows for a smooth transition between the classical and saturated conduction regimes. In the above expression, $q_{\rm spi}$ represents the classical conductive flux (Spitzer 1962)

$$q_{\rm spi} = -\kappa(T) \nabla T \ , \tag{A.10}$$

where $\kappa(T) = 9.2 \times 10^{-7} T^{5/2}$ erg s^{-1} K^{-1} cm^{-1} is the thermal conductivity. The saturated flux, $q_{\rm sat}$, is given by (Cowie & McKee 1977)

$$q_{\rm sat} = -sign(\nabla T) 5 \phi \rho c_{\rm s}^3 \ , \tag{A.11}$$

where $\phi \sim 0.3$ (Giuliani 1984; Borkowski et al. 1989, and references therein) and $c_{\rm s}$ is the isothermal sound speed.

A.1.7 Source module

This module consists of several sub-modules which handle the heating of the fluid, its ionization state, nuclear reactions, its cooling due to radiative losses. In this thesis the sub-module *cooling/radloss* has been used in order to explain the emission from protostellar jets.

Cooling/radloss

The *radloss* module accounts for the radiative losses from optically thin plasma effects. The function $P(T)$ is the optically thin radiative losses function per unit emission measure (Raymond & Smith 1977; Raymond 1978) and has been approximated using the piece-wise power law shown in Fig. A.6.

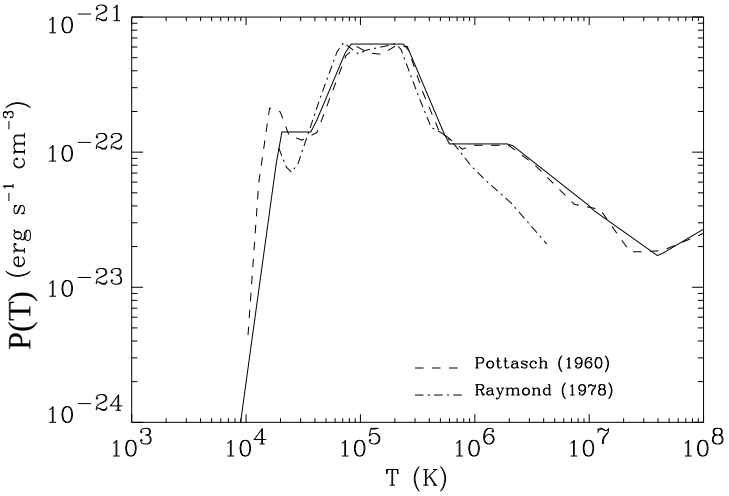

Figure A.6: $P(T)$ is the optically thin radiative losses function per unit emission measure.

Appendix B

The X-rays satellites: XMM-Newton and Chandra telescopes

B.1 XMM-Newton telescope

The ESA *X-ray Multi Mirror-Newton* telescope has been launched on December 10, 1999.

B.1.1 Characteristics

Main characteristics of the XMM-Newton telescope, explained in more details in the following sections, are:

- Simultaneous operations of six instruments (three CCDs detectors; two spectroscopes; an optical monitoring system)

  All the instruments on board of XMM-Newton can operate simultaneously and independently.

- High sensitivity

  XMM-Newton telescope has the largest effective area of a focusing telescope ever. The total mirror geometric effective area at 1.5 keV energy is ca. 1550 cm^2 for each telescope, i.e., 4650 cm^2 in total.

- Good angular resolution

  The *Point Spread Function* (PSF) of the mirrors has a FWHM (*Full Width Half Maximum*) of about $6''$ and a HEW, at which 50 % of the total energy are encircled, of ca. $15''$.

- Moderate and high spectral resolution

  The EPIC CCD cameras have moderate spectral resolution, with a resolving power, E/ΔE, of ca. 20-50 at 1 keV e a 6.7 keV respectively. The RGS spectrometers offer much higher spectral resolution, with a resolving power in the range of $E/\Delta E \approx 100 - 500$.

- Simultaneous optical/UV observations

  Observations with the co-aligned OM optical/UV telescope render possible the monitoring and identification of optical/UV counterparts of X-ray sources seen by the X-ray telescopes.

B.1.2 X-rays telescopes

XMM-Newton consists of three identical X-rays telescopes with a focal length of 7.5 m. Each telescope is composed by 58 grazing incidence mirrors, coaxial and co-focal, which consist of a paraboloid and an hyperboloid in the Wolter-1 configuration (Fig. B.1).

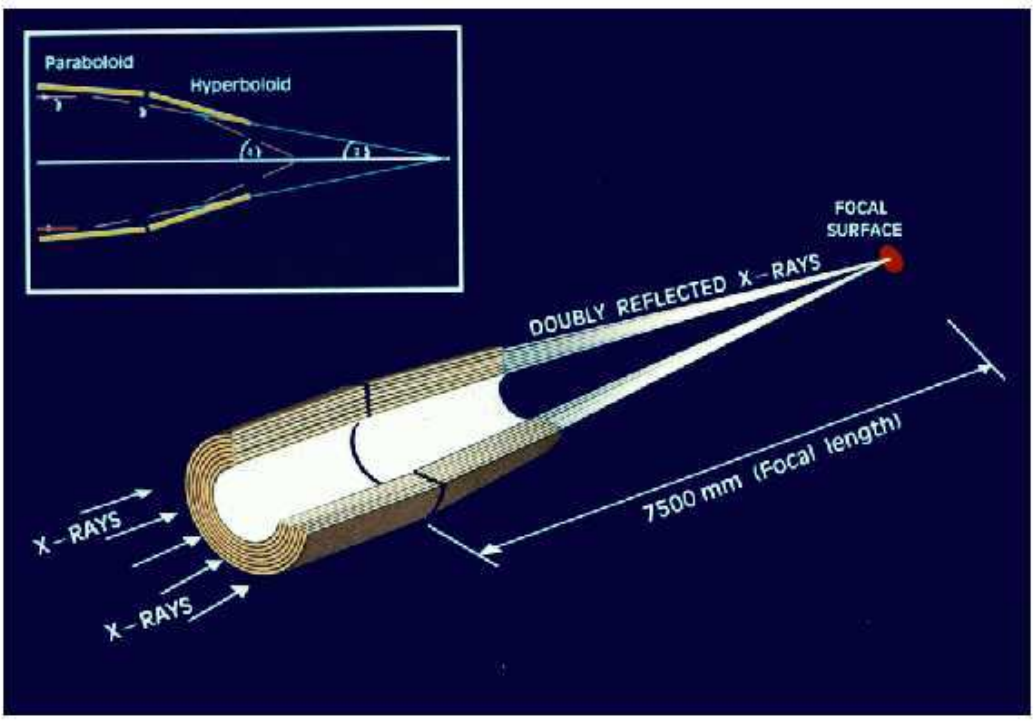

Figure B.1: The light path in XMM-Newton's open X-ray telescope with the pn camera in focus

The light path of one of the three telescopes is shown in Fig. B.1. Two of the three telescope have a dispersion grating along their light path as in Fig. B.2.

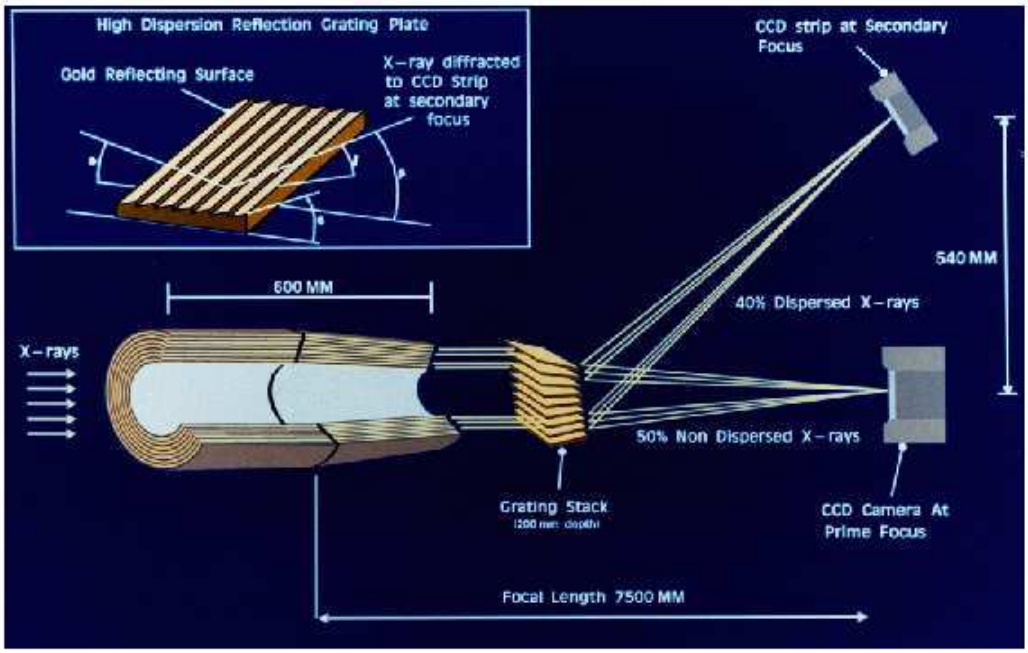

Figure B.2: The light path in the two XMM-Newton telescopes with grating assemblies (not to scale). Note that the actual fraction of the non-intercepted light that passes to the primary MOS focus is 44 %, while 40 % of the incident light is intercepted by grating plates of the RGA.

The geometric area of the XMM-Newton satellite is $1550\,cm^2$ for each telescope. The most important information for XMM-Newton users is the mirror effective area, folded through the response of the different focal instruments.

One can see that the XMM-Newton mirrors are most efficient in the energy range from 0.1 to 10 keV, with a maximum at about 1.5 keV and a pronounced edge near 2 keV (the Au M edge). The effective areas of the two MOS cameras are lower than that of the pn, because only part of the incoming radiation falls onto these detectors, which are partially obscured by the RGAs (Fig. B.2).

However the effective area of the mirrors is a function of off-axis angle within the mirrors' $30'$ FOV. With increasing off-axis angle, less of the photons entering the telescopes actually reach the focal plane. This effect is called "vignetting". The vignetting of the XMM-Newton telescopes, which is reflected by the decline of the X-ray telescope's effective area as a function of off-axis angle, is displayed for a few energies for the X-ray telescope 2 in Fig. B.3.

B.1.3 Detectors

Several detectors are on board the XMM-Newton telescope:

- RGS
- EPIC : MOS, PN, RMS

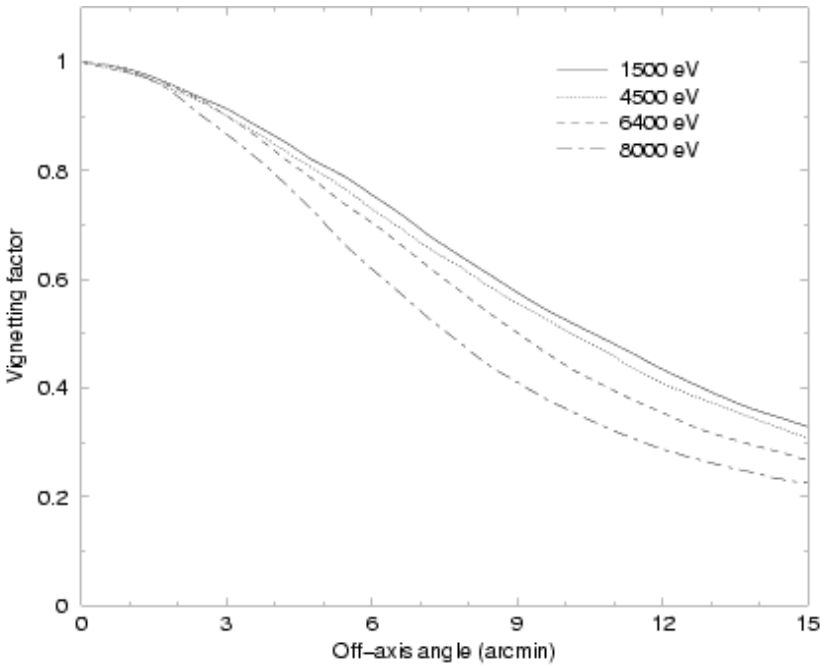

Figure B.3: Vignetting function as a function of off-axis angle

Table B.1: Main characteristics of the detectors on board on the XMM-Newton telescope.

INSTRUMENTS	RGS	MOS	pn	OM
Band	$0.35 - 2.5$ keV	$0.15 - 12$ keV	$0.15 - 15$ keV	$160 - 600$ nm
Effective area	$\sim$ 55 cm^2	$\sim$ 450 cm^2	$\sim$ 1400 cm^2	-
FOV	$5'$	$30'$	$30'$	$17'$
PSF	$--$	$5''/14''$	$6.6''/15''$	$\sim 1'$
Pixel dimension	81 μm	40 μm (1.1″)	150 μm (4.1″)	$1''$
Temporal resolution	16 ms	1.5 ms	0.03 ms	500 ms
Spectral resolution	0.04 Å	$\sim$ 70 eV	$\sim$ 80 eV	0.5/1.0 nm

- OM

Tab. B.1 shows the main characteristics of such instruments.

EPIC

The European Photon Imaging Camera (EPIC) is composed by three CCD detectors, which allow to obtain images and to perform non dispersive spectroscopy in the range 0.15 keV - 10 keV, and by a monitoring system of the the spurious radiation, the Radiation Monitor System (RMS), which turn off the instrument when

the protons and electrons flux is too high in order not to damage the instruments itself.

On the focal plane of two of the three telescopes, is located the Metal Oxide Semi-conductor (MOS) detector. On the focal plane of the third telescope a pn detector is located. The last pn camera allows to reach high temporal resolution, up to 0.03 ms.

The Field Of View (FOV) of the EPIC camera are of the order of $30'$ in the energy range 0.15 keV a 15 keV, with a moderate angular and spectral resolution ($E/\Delta E \approx 20 - 50$). The angular resolution depends on both the dimension of the pixels in the CCDs and the Point Spread Function (PSF) of the mirrors. The FWHM of the PSF is about $6''$, but the HEW is greater, being about $15''$.

Main differences between the EPIC pn and EPIC MOS cameras

The EPIC MOS cameras consist of 7 identical CCDs, which are not co-planar, but offset with respect to each other, following closely the slight curvature of the focal surface of the Wolter telescopes. They are located on the two telescopes where the RGS is, so they collect only 44 % of the total X-rays.

EPIC pn consists of 12 coplanar CCDs.

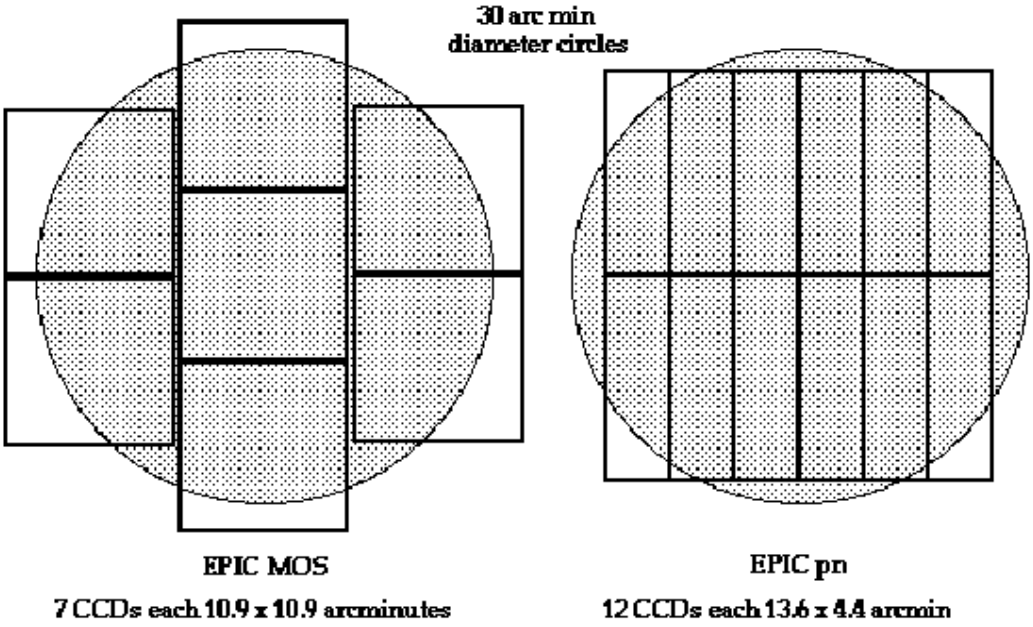

Figure B.4: Geometric configuration of the two EPIC cameras: MOS (on the left), pn (on the right). The circle refers to an area with a diameter of $30'$.

The two types of EPIC cameras differ not only in the geometric configuration, as shown in Fig. B.4. As an example, the EPIC pn camera allows high temporal resolution, up to integration time of about 30μs. Furthermore the MOS CCDs

are FI CCDs, while the pn CCDs are BI. The type of CCDs involved, FI or BI, lead to different efficiency of the two different cameras. Figs. B.5 and B.6 show the quantum efficiency (QE) of the MOS and pn cameras. From this figure is clear the reason why the MOS CCDs cannot detect high energy photons while the pn camera can detect photons with energy up to 15 keV.

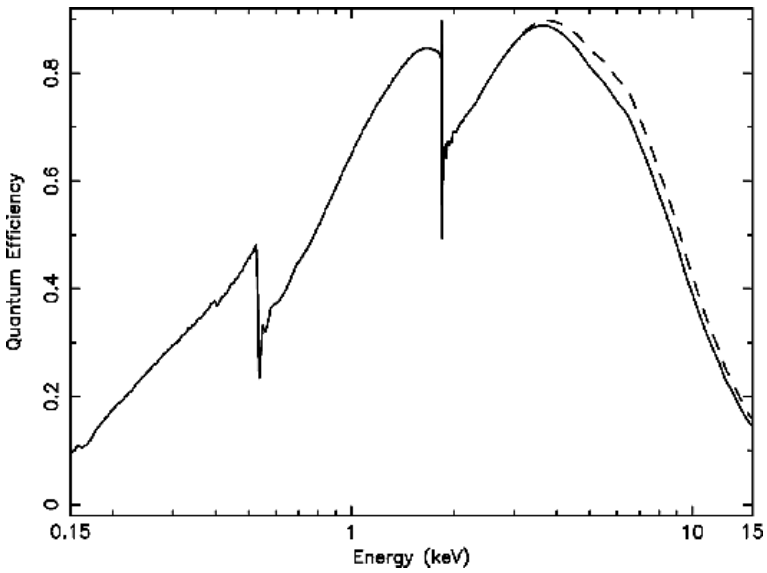

Figure B.5: Quantum efficiency of the EPIC MOS1 (solid line) and MOS2 (dashed line) CCD1 chip as a function of photon energy.

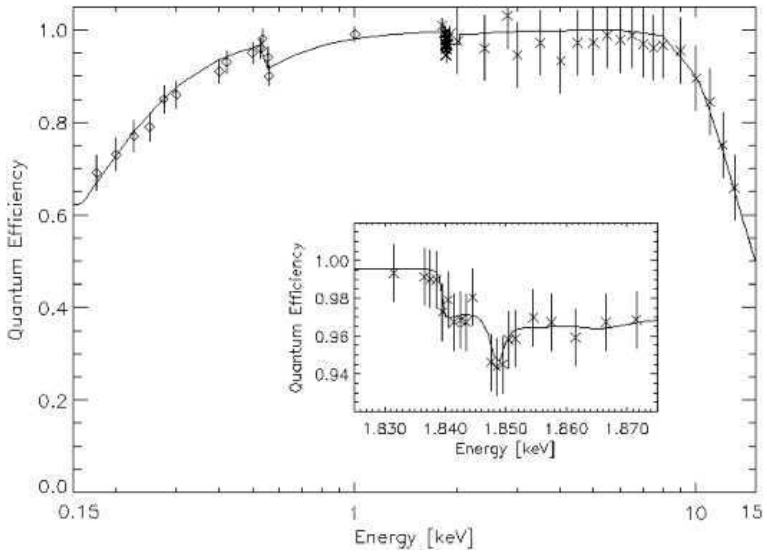

Figure B.6: Quantum efficiency of the EPIC pn CCD chips as a function of photon energy (Strüder et al. 2001, Fig. 5).

B.2 The Chandra telescope

The *Chandra X-Ray Observatory* has been launched by *NASA* on July 23, 1999. It was designed in order to reach better resolution, both spatial and spectral, with respect to all the previous X-ray telescopes. In fact the *High Resolution Mirror Assembly* (HRMA) allows to obtain images with an Half Power Diameter (HPD) of the point spread function (PSF) of about 0.5 arcsec. Furthermore the *Low Energy Transmission Grating* (LETG) and *High Energy Transmission Grating* (HETG) achieve resolving power >> 500 in most of their working range, which in total is 0.1 keV a 10 keV. The location of each instrument on board on Chandra telescope is shown in Fig. B.7.

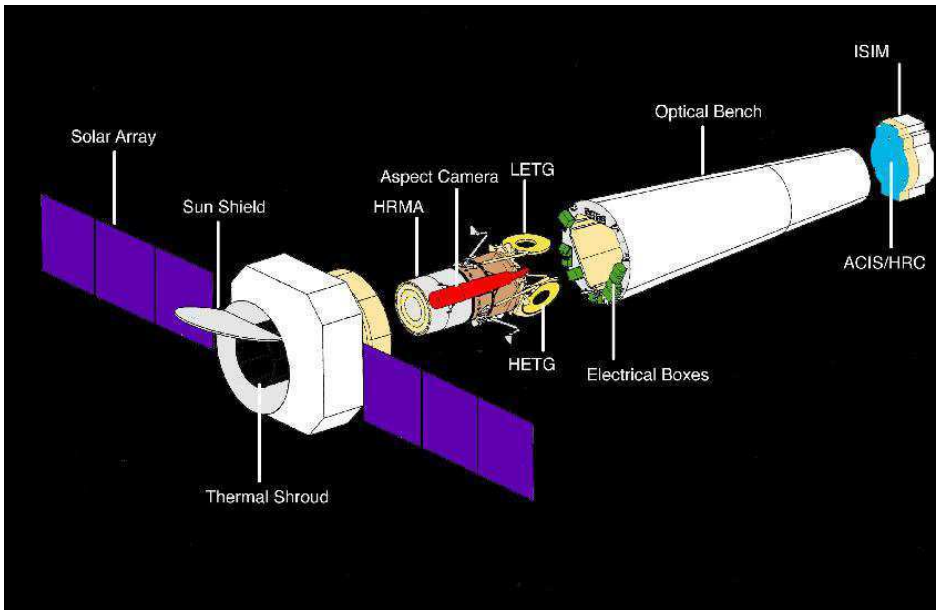

Figure B.7: Configuration of the instruments on board of Chandra telescope.

B.2.1 HRMA

The *High Resolution Mirror Assembly* consists of a set of four grazing-incidence mirrors for X-rays. Each mirror consist of a parabolic-hyperbolic surface in the Wolter-1 configuration. The diameter of the largest mirror is 1.2 m. The focal length is 10 m.

B.2.2 EPHIN

Located near the telescope, the *Electron, Proton, Helium INstrument* (EPHIN), avoids the focal plane instruments to be damaged by the radiation from the charged particles in the surroundings of the telescope.

B.2.3 Detectors

On the Chandra focal plane are located the two instruments AXAF CCD Imaging Spectrometer (ACIS) and the High Resolution Camera (HRC), which both consist of two components - ACIS-I ed -S, HRC-I ed -S. The first (i. e. the -I type) is used to collect the images, the second (i. e. the -S type) is used to read the spectra. Fig. B.8 shows the configuration of these two instruments, ACIS and HRC, on the focal plane.

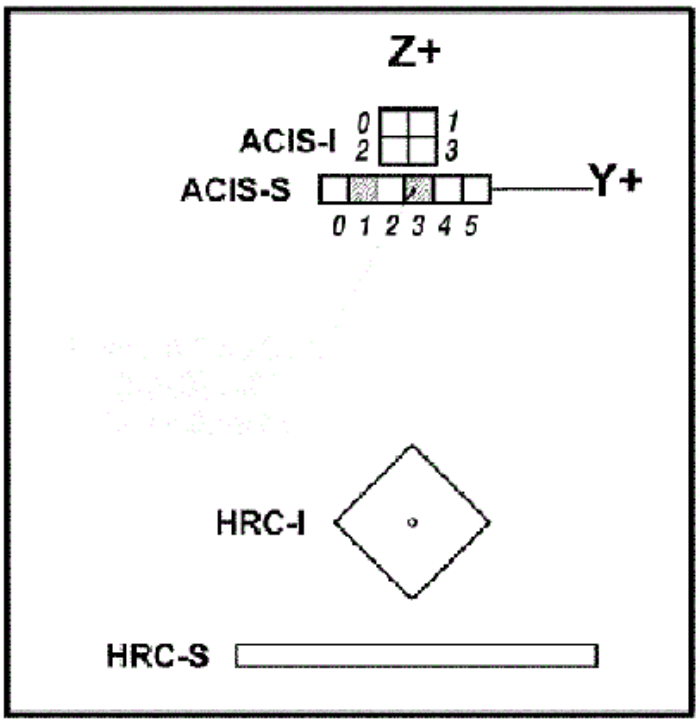

Figure B.8: Configuration of the two instruments ACIS and HRC on the focal plane. The two shadowed CCDs in ACIS-S are *back illuminated*

ACIS

The *Advanced CCD Imaging Spectrometer* (Fig. B.9) is used to collect high resolution images and for non-dispersive spectroscopy at medium resolution.

When this instrument is coupled with the *High Energy Transmission Grating* (HETG) or with the *Low Energy Trasmission Grating* (LETG) it is possible to achieve a better spectral resolution. The LETG and HETG spectrometers are grating arrays which can be flipped into the path of the X-rays just behind the mirrors, where they redirect (diffract) the X-rays according to their energy. The X-ray position is measured by HRC or ACIS, so that the exact energy can be determined. The science instruments have complementary capabilities to record

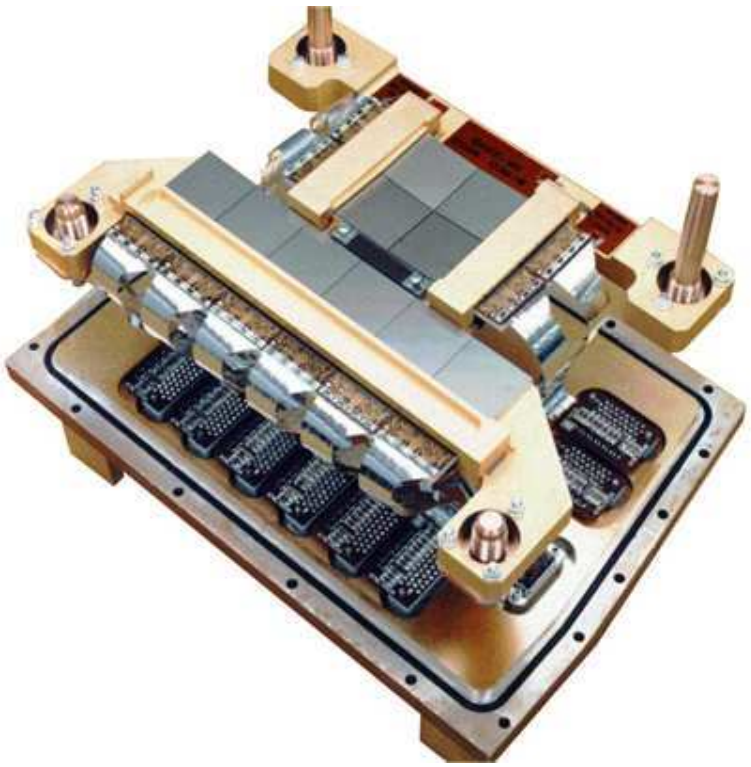

Figure B.9: An illustration of the ACIS detector. The ten CCDs are well visible on top of the instrument.

and analyze X-ray images of celestial objects and probe their physical conditions with unprecedented accuracy.

ACIS is composed by ten CCDs (each consisting of 1024×1024 pixels) of two different types: front-illuminated, (FI) or back-illuminated, (BI). The response of the BI CCDs achieves lower energy values than the FI CCDs, whose response is more efficient at high energies.

Four FI CCDs are arranged in a 2×2 matrix so as to form the ACIS-I, used to obtain images. Otherwise, ACIS-S consists of six CCDs, two BI CCDs and four FI CCDs, arranged in a single row, and allows to analyze high resolution spectrometry when it is coupled with the HETG.

HRC

The *High Resolution Camera* consists of two microchannel plate (MCP) detectors: HRC-I, normal to the optical axis, used for the images, and HRC-S which transfers the data to the LETG. The HRC field-of-view is the widest on board of Chandra ($\sim 30' \times 30'$) and its instrumental response reach energies lower than the ACIS sensibility (Tab. B.2 shows the main characteristics of the instruments on board of Chandra).

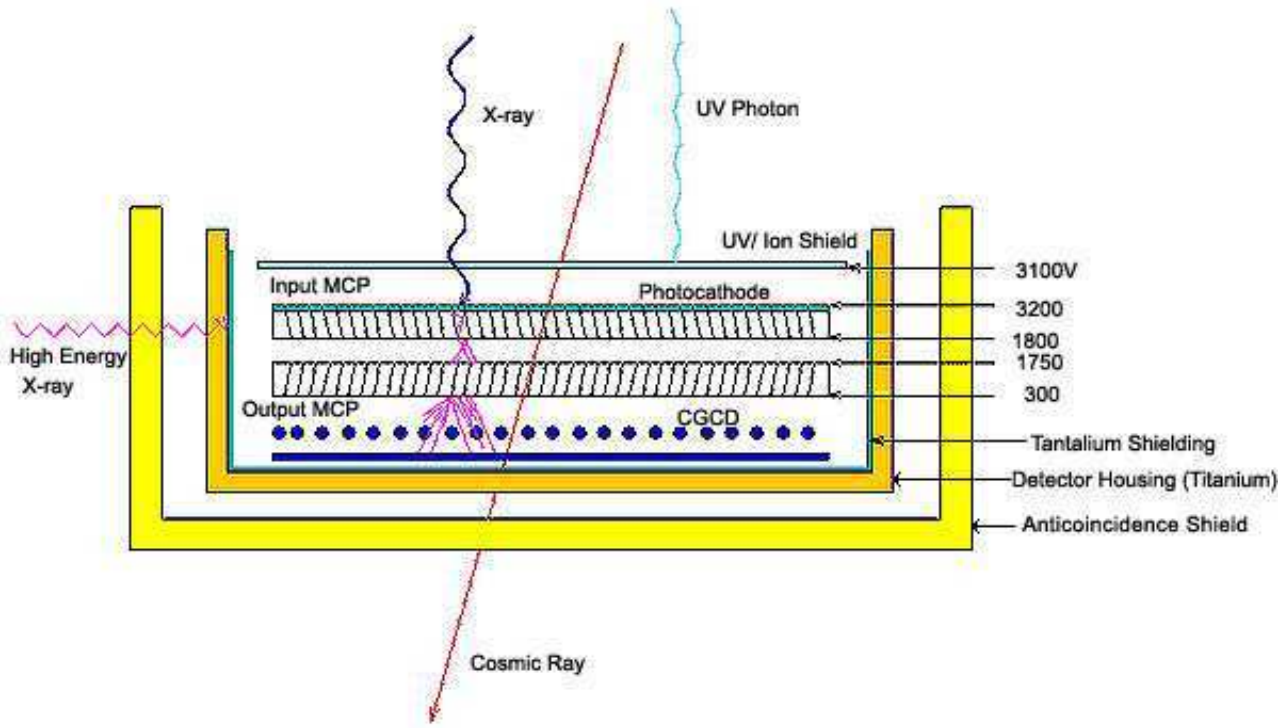

Figure B.10: Scheme of the HRC microchannels plate detector.

Table B.2: Main characteristics of the instruments on board of Chandra.

INSTRUMENTS	ACIS	HRC	HETG	LETG
Band	$0.4 - 6.0$ keV	$0.08 - 10.0$ keV	$0.4 - 10$ keV	$70 - 10000$ eV
Effective area	$40 - 110$ cm^2	$133 - 227$ cm^2	$7 - 200$ cm^2	$1 - 200$ cm^2
FOV		$30' \times 30'$		
PSF		$0.4''$	$0.01 - 0.02\mathring{A}$	$0.05\mathring{A}$
Pixel dimension	$24\,\mu$m			$6.4 - 24.0\,\mu$m
Temporal resolution	2.8 ms	$16\,\mu$ s		$16\,\mu$ s-3.24 s
Spectral resolution		~ 1	$0.4 - 77$ eV	1000

Fig. B.10 shows how the HRC works. X-rays go through a shield which prevents UV rays and low energy ions and electrons to reach the instrument. Most of the X-ray emission is absorbed by the walls of the first of the two consecutive MCP called input. Electrons obtained from the photoelectric effect are the accelerated by an electric field applied in this region. The interaction with the walls will produce an electron cascade. The second MPC (the output one) allows to achieve a greater gain. The electron cloud - of the order 2×10^7 electrons per photon - obtained from the output, is accelerated towards a position-sensitive

charge detector.

The HRC PSF is well modeled with a Gaussian with a FWHM of ~ 20 μ m (~ 0.4 arcsec).

B.2.4 Effective area

Fig. B.11 shows the comparison between the effective area as a function of energy for the ACIS and HRC.

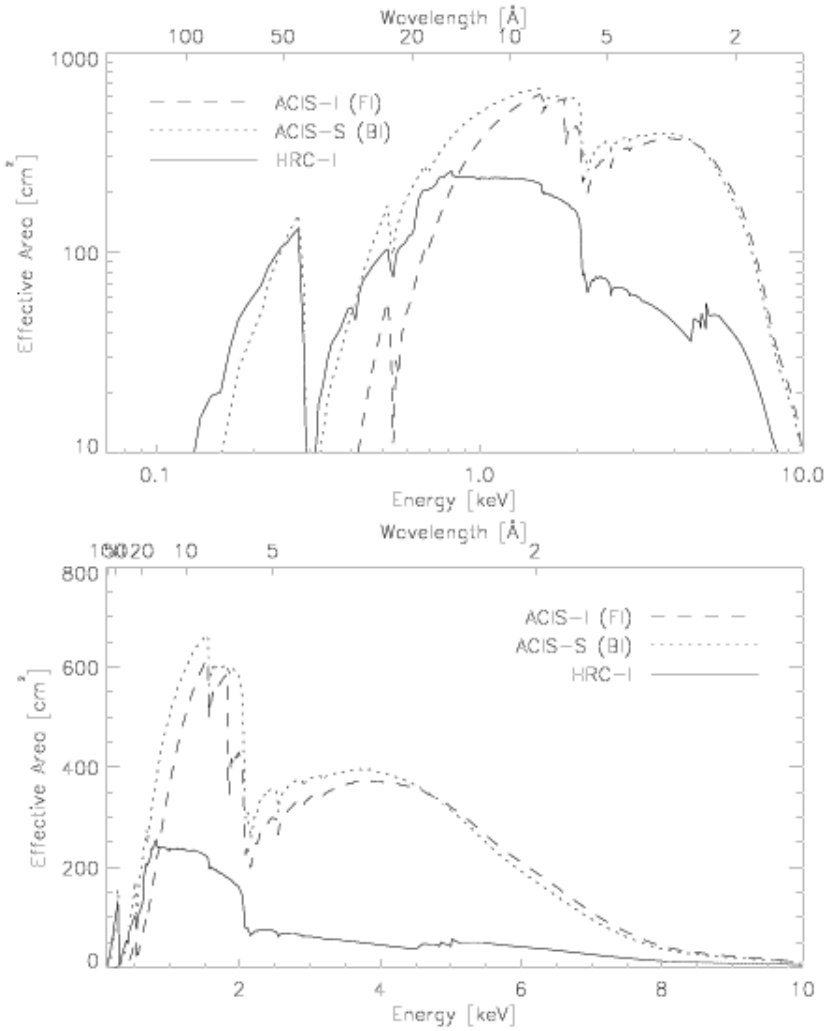

Figure B.11: A comparison between the effective area, for a point-like source on axis, as a function of the energy, for different instruments on Chandra telescope.

Appendix C

The *Hubble Space Telescope* (HST) satellite

The Hubble Space Telescope is a cooperative program of the European Space Agency (ESA) and the National Aeronautics and Space Administration (NASA) and it is operational in the 1990s. HST is a 2.4-meter reflecting telescope which was deployed in low-Earth orbit (600 kilometers) by the crew of the space shuttle Discovery (STS-31) on 25 April 1990.

Responsibility for conducting and coordinating the science operations of the Hubble Space Telescope rests with the Space Telescope Science Institute (STScI) on the Johns Hopkins University Homewood Campus in Baltimore, Maryland.

HST's current complement of science instruments include three cameras, two spectrographs, and fine guidance sensors (primarily used for astrometric observations). Because of HST's location above the Earth's atmosphere, these science instruments can produce high resolution images of astronomical objects. Ground-based telescopes can seldom provide resolution better than 1.0 arc-seconds, except momentarily under the very best observing conditions. HST's resolution is about 10 times better, or 0.1 arc-seconds.

The current HST instruments are:

- Observatory Calibration, Focal Plane, Telescope, Cross-Instrument Issues
- ACS Advanced Camera for Surveys
- FGS The Fine Guidance Sensors
- NICMOS Near Infrared Camera and Multi Object Spectrometer
- STIS Space Telescope Imaging Spectrograph
- WFPC2 The Wide Field Planetary Camera 2

I will discuss in more details the WFPC2 camera which has been used to derive the optical observations of the protostellar jet HH 154 discussed in this thesis.

C.1 The Wide Field Planetary Camera 2

The scientific objective of the WFPC2 is to provide photometrically and geometrically accurate images of astronomical objects over a relatively wide field-of-view (FOV), with high angular resolution across a broad range of wavelengths.

Wide Field and Planetary Camera 2 (WFPC2) is a two-dimensional imaging photometer located at the center of the Hubble Space Telescope (HST) focal plane. Its field-of-view is centered on the optical axis of the telescope and it therefore receives the highest quality images. It simultaneously images a 150" × 150" L-shaped region with a spatial sampling of 0.1" per pixel, and a smaller 34" × 34" square field with 0.046" per pixel. In fact it consists of 4 adjacent 800×800 pixels CCD. The WFPC2 CCDs are thick, front-side illuminated devices. Of these four CCDs, the three WF2-4 which comprise the Wide Field Camera (WFC) with the L-shaped field-of-view has a plate scale corresponding to 0.0996"/pix, while the fourth chip has a better resolution, corresponding to 0.0455"/pix and is referred to as the Planetary Camera (PC).

The four cameras are called PC1, WF2, WF3, and WF4, and their fields-of-view are illustrated in Figure C.1.

The WFPC2 contains 48 filters mounted in 12 wheels of the Selectable Optical Filter Assembly (SOFA). These include a set of broad band filters, as well as a set of wide U, B, V, and R filters. Narrow band filters include those for emission lines of Ne V (3426Å), CN (3900Å), [OIII] (4363Å and 5007Å), He II (4686Å), H_β (4861Å), He I (5876Å), [OI] (6300Å), H_α (6563Å), [NII] (6583Å), [SII] (6716Å and 6731Å), and [SIII] (9531Å).

The narrow point spread function is essential to all science programs being conducted with the WFPC2, because it allows one to both go deeper than ground based imagery, and to resolve smaller scale structure with higher reliability and dynamic range. Further, many of the scientific goals which originally justified the HST require that these high quality images be obtained across a wide field-of-view.

A unique capability of the WFPC2 is that it provides a sustained, high resolution, wide field imaging capability in the vacuum ultraviolet.

The field-of-view and angular resolution of the wide field and planetary camera is split up as in Tab. C.1.

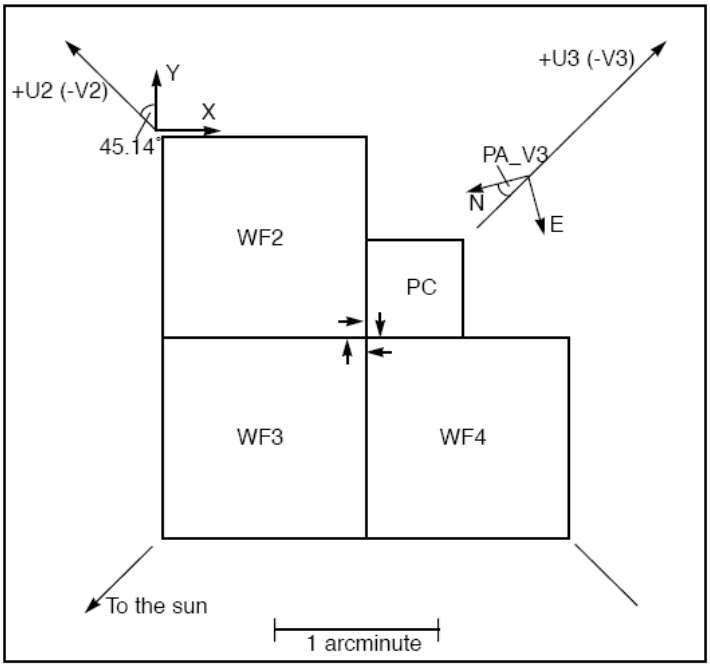

Figure C.1: WFPC2 Field-of-View Projected on the Sky. It consists of four larger cameras, WF2-4, arranged in an L-shape field-of-view, and of a smaller camera, PC, with an higher spatial resolution.

Table C.1: Summary of WFPC2 Camera Format.

Camera	Pixel and CCD Format	Field-of-View	Pixel Scale
Wield Field	$(800 \times 800) \times 3$ CCDs	$2.5' \times 2.5'$ (L-shaped)	$\approx 0.1''$
Planetary	$(800 \times 800) \times 3$ CCDs	$35'' \times 35''$	$\approx 0.046''$

C.1.1 Cosmic Rays

HST is subjected to cosmic rays and protons from the Earth's radiation belts. Cosmic ray events usually deposit significant quantities of charge in more than one pixel. This is due partly to the finite thickness of the CCD detectors, and partly to the less than perfect collection efficiency of each pixel. Fig. C.2 shows a histogram of the number of affected pixels for each cosmic ray event. For the purposes of the figure, a cosmic ray is defined as having a peak pixel value more than 10 DN (i. e. counts) above the background; and an affected pixel is an attached pixel with a value more than 2 DN above the background.

Faint images and low energy cosmic rays are often indistinguishable. Long science observations are therefore usually broken into at least two exposures (CR-SPLIT) to ensure that events can be identified.

One difficulty in this measurement is caused by hot pixels, for some of which the dark current has significant fluctuations from frame to frame; these can be

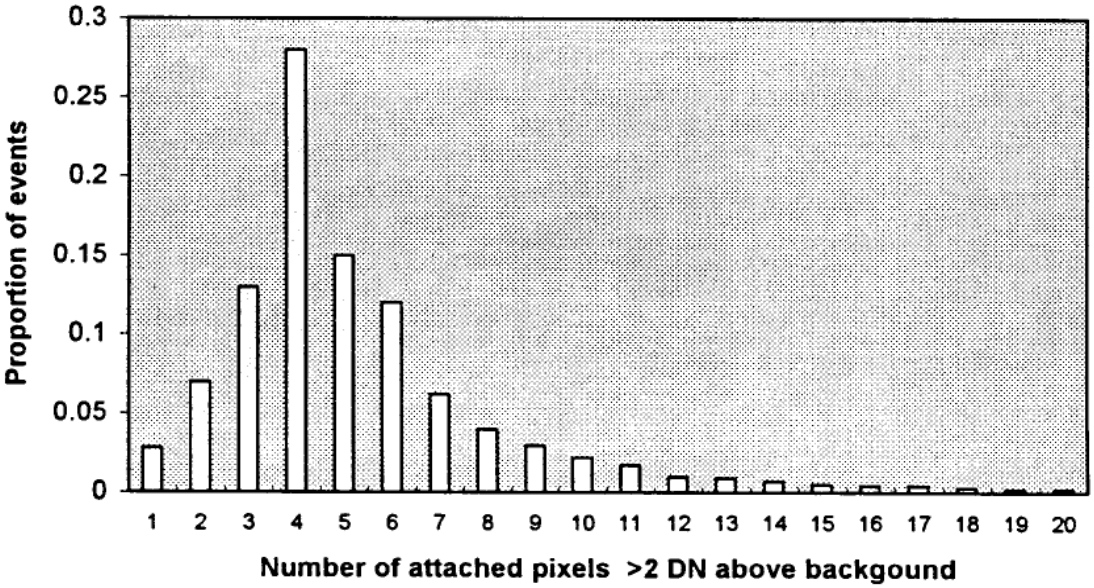

Figure C.2: Histogram of Cosmic Ray Event Sizes. A cosmic ray event is defined by having a peak pixel of at least 10 DN.

mistakenly identified as cosmic rays when the dark current is at a maximum. Single-pixel events constitute 10% of the total number of events identified, but at least half of them recur in the same position in several frames, thus identifying them as damaged (hot) pixels, rather than true cosmic rays. Also, unlike the majority of cosmic ray events, single-pixel events tend to have very small total signal; the majority have a total signal of less than 200 electrons, as expected from hot pixels, while the signal distribution of multiple-pixel events peaks around 1000 electrons. For this reason, single-pixel events have been classified as "bad pixels" rather than "cosmic rays". While we cannot exclude that some true single-pixel events do occur, they are very rare, probably less than 2% of the total. Cosmic ray events are frequent, occurring at an average rate of 1.8 events chip^{-1} s^{-1}.

The distribution of total signal is shown in Fig. C.3; it has a well-defined maximum at about 1000 electrons, and a cut-off at about 500 electrons. The latter is well above the detection threshold used for the above measurements (25 electrons in the central pixel of the cosmic ray), and is therefore undoubtedly real.

The histogram in Fig. C.3 shows the distribution of total energy of all cosmic ray events. One encouraging feature is the very small number of events below about 30 DN. This low energy drop is well above the energy level of excluded single-pixel events.

The number of pixels affected by cosmic ray events is an average of 6.7 pixels, for about 12 affected pixels chip^{-1} s^{-1}. For a 2000s exposure, this results in about 24,000 affected pixels, or 3.8% of all pixels. As cosmic rays are expected to be

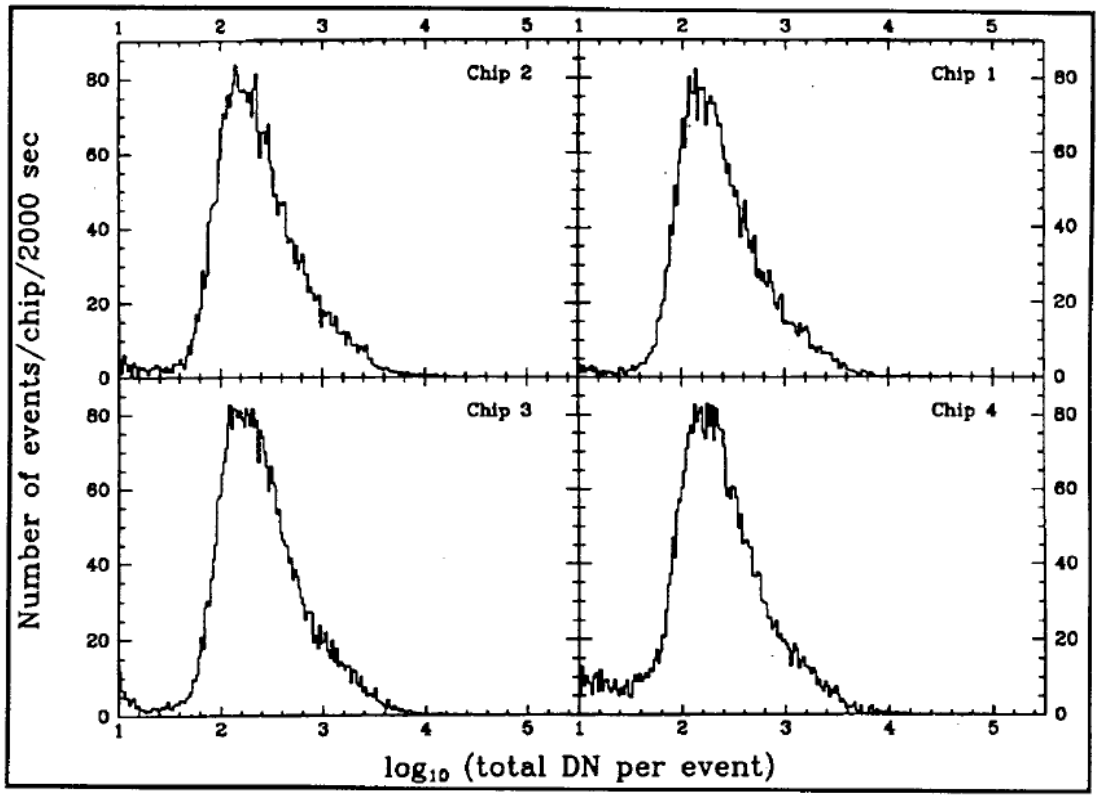

Figure C.3: Histogram of Cosmic Ray Event energies.

randomly placed, a pair of such exposures would have about 900 pixels affected in both exposures; cosmic ray correction is impossible for such pixels. For a pair of 1000s exposures, about 220 pixels will be affected in both frames. Cosmic ray activity varies as a function of time, geomagnetic latitude of the spacecraft, and other factors. The average numbers given here are subject to change in individual exposures.

Appendix D

Acronym and abbreviation list

ACIS	AXAF CCD Imaging Spectrometer
AXAF	Advanced X-ray Astrophysics Facility
CCD	Charge Coupled Device
CIAO	Chandra Interactive Analysis of Observations
CTT	Classical T Tauri
EM	Emission Measure
EPIC	European Photon Imaging Camera
FOV	Field Of View
FWHM	Full Width Half Maximum
HD	HydroDynamic
HH	Herbig-Haro
HST	Hubble Space Telescope
IRAF	Image Reduction and Analisys Facility
IRS	InfraRed Source
ISM	InterStellar Medium
IWS	Internal Working Surface
PC	Planetary Camera
PPM	Piecewise-Parabolic Method
PSF	Point Spread Function
STSDAS	Space Telescope Science Data Analisys System
UV	Ultra Violet
VLA	Very Large Array
WF	Wide Field
WFPC	Wide Field and Planetary Camera
WLTT	Weak Line T Tauri
WS	Working Surface

XMM	X-ray Multi-Mirror mission
XSPEC	X-ray SPECtral fitting package
YSO	Young Stellar Object

Acknowledgements

I gratefully acknowledge my supervisor, Prof. Giovanni Peres, and Dr. Salvatore Orlando who have guided me during all my PhD course, for their continuous support and their useful suggestions. I express special thanks to Dr. Fabio Favata, Dr. Malcolm Fridlund, Dr. Giusi Micela and Prof. Salvatore Sciortino for their contribution to the work presented in this thesis. I would like also to express my gratitude to Dr. Marco Miceli and all the researchers and technicians at the INAF - Osservatorio Astronomico di Palermo and at the ESA - ESTEC of Noordwijk.

Bibliography

Bally, J., Feigelson, E., & Reipurth, B. 2003, ApJ, 584, 843

Bally, J. & Reipurth, B. 2002, in Revista Mexicana de Astronomia y Astrofisica Conference Series, ed. W. J. Henney, W. Steffen, L. Binette, & A. Raga, 1–7

Bieging, J. H. & Cohen, M. 1985, ApJ, 289, L5

Bodo, G., Massaglia, S., Ferrari, A., & Trussoni, E. 1994, A&A, 283, 655

Bonito, R., Fridlund, M., Favata, F., Micela, G., & Peres, G. 2008, submitted

Bonito, R., Orlando, S., Peres, G., Favata, F., & Rosner, R. 2004, A&A, 424, L1

Bonito, R., Orlando, S., Peres, G., Favata, F., & Rosner, R. 2007, A&A, 462, 645

Borkowski, K. J., Shull, J. M., & McKee, C. F. 1989, ApJ, 336, 979

Cabrit, S. & Bertout, C. 1992, A&A, 261, 274

Chevalier, R. A. & Raymond, J. C. 1978, ApJ, 225, L27

Chini, R., Ward-Thompson, D., Kirk, J. M., et al. 2001, A&A, 369, 155

Colella, P. & Woodward, P. R. 1984, Journal of Computational Physics, 54, 174

Cowie, L. L. & McKee, C. F. 1977, ApJ, 211, 135

Cudworth, K. M. & Herbig, G. 1979, AJ, 84, 548

Curiel, S., Ho, P. T. P., Patel, N. A., et al. 2006, ApJ, 638, 878

Dalton, W. W. & Balbus, S. A. 1993, ApJ, 404, 625

Favata, F., Fridlund, C. V. M., Micela, G., Sciortino, S., & Kaas, A. A. 2002, A&A, 386, 204

Favata, Bonito, F., Micela, G., Fridlund, M., et al. 2006, A&A, 450, L17

Field, G. B. 1965, ApJ, 142, 531

Fridlund, C. V. M., Bergman, P., White, G. J., Pilbratt, G. L., & Tauber, J. A. 2002, A&A, 382, 573

Fridlund, C. V. M. & Liseau, R. 1994, A&A, 292, 631

Fridlund, C. V. M. & Liseau, R. 1998, ApJ, 499, L75

Fridlund, C. V. M., Liseau, R., Djupvik, A. A., et al. 2005, A&A, 436, 983

Fridlund, C. V. M., Sandqvist, A., Nordh, H. L., & Olofsson, G. 1989, A&A, 213, 310

Fryxell, B., Olson, K., Ricker, P., et al. 2000, ApJS, 131, 273

Güdel, M., Skinner, S. L., Briggs, K. R., et al. 2005, ApJ, 626, L53

Giuliani, J. L. 1984, ApJ, 277, 605

Grosso, N., Feigelson, E. D., Getman, K. V., et al. 2006, A&A, 448, L29

Haro, G. 1952, ApJ, 115, 572

Hartigan, P. 1989, ApJ, 339, 987

Hartigan, P., Bally, J., Reipurth, B., & Morse, J. 2000, PPIV

Hartigan, P., Morse, J. A., Tumlinson, J., Raymond, J., & Heathcote, S. 1999, ApJ, 512, 901

Herbig, G. H. 1950, ApJ, 111, 11

Holtzman, J. A., Burrows, C. J., Casertano, S., et al. 1995, PASP, 107, 1065

Kaastra, J. S. & Mewe, R. 2000, in Atomic Data Needs for X-ray Astronomy, p. 161

Kenyon, S. J., Dobrzycka, D., & Hartmann, L. 1994, AJ, 108, 1872

Landau, L. D. & Lifshitz, E. M. 1959, Fluid mechanics (Course of theoretical physics, Oxford: Pergamon Press, 1959)

Lery, T., Heyvaerts, J., Appl, S., & Norman, C. A. 1998, A&A, 337, 603

Liseau, R., Fridlund, C. V. M., & Larsson, B. 2005, ApJ, 619, 959

Looney, L. W., Mundy, L. G., & Welch, W. J. 1997, ApJ, 484, L157+

MacNeice, P., Olson, K. M., Mobarry, C., de Fainchtein, R., & Packer, C. 2000, Computer Physics Comm., 126, 330

McCaughrean, M., Zinnecker, H., Andersen, M., Meeus, G., & Lodieu, N. 2002, The Messenger, 109, 28

Mellema, G. & Frank, A. 1997, MNRAS, 292, 795

Mewe, R., Gronenschild, E. H. B. M., & van den Oord, G. H. J. 1985, A&AS, 62, 197

Moriarty-Schieven, G. H., Johnstone, D., Bally, J., & Jenness, T. 2006, ApJ, 645, 357

Moro-Martín, A., Cernicharo, J., Noriega-Crespo, A., & Martín-Pintado, J. 1999, ApJ, 520, L111

Morrison, R. & McCammon, D. 1983, ApJ, 270, 119

Neckel, T. & Staude, H. J. 1987, ApJ, 322, L27

Norman, M. L., Winkler, K.-H. A., Smarr, L., & Smith, M. D. 1982, A&A, 113, 285

Olson, K. M., MacNeice, P., Fryxell, B., et al. 1999, Bulletin of the American Astronomical Society, 31, 1430

Orlando, S. & Favata, F. 2007, Observations and Modeling of X-ray Emission from Jets of Infant Stars (.)

Orlando, S., Peres, G., Reale, F., et al. 2005, A&A, 444, 505

Podio, L., Bacciotti, F., Nisini, B., et al. 2006, A&A, 456, 189

Pravdo, S. H., Feigelson, E. D., Garmire, G., et al. 2001, Nature, 413, 708

Pravdo, S. H. & Tsuboi, Y. 2005, ApJ, 626, 272

Pravdo, S. H., Tsuboi, Y., & Maeda, Y. 2004, ApJ, 605, 259

Raga, A. C., Binette, L., Canto, J., & Calvet, N. 1990, ApJ, 364, 601

Raga, A. C., Böhm, K.-H., & Cantó, J. 1996, Revista Mexicana de Astronomia y Astrofisica, 32, 161

Raga, A. C., Noriega-Crespo, A., & Velázquez, P. F. 2002, ApJ, 576, L149

Ray, T. P., Muxlow, T. W. B., Axon, D. J., et al. 1997, Nature, 385, 415

Raymond, J. C. 1978, ApJ, 222, 1114

Raymond, J. C. & Smith, B. W. 1977, ApJS, 35, 419

Reipurth, B. & Bally, J. 2001, ARA&A, 39, 403

Rodriguez, L. F., Canto, J., Torrelles, J. M., & Ho, P. T. P. 1986, ApJ, 301, L25

Rodríguez, L. F., Curiel, S., Cantó, J., et al. 2003a, ApJ, 583, 330

Rodríguez, L. F., Curiel, S., Cantó, J., et al. 2003b, ApJ, 583, 330

Rodríguez, L. F., D'Alessio, P., Wilner, D. J., et al. 1998, Nature, 395, 355

Snell, R. L., Loren, R. B., & Plambeck, R. L. 1980, ApJ, 239, L17

Spitzer, L. 1962, Physics of Fully Ionized Gases (New York: Interscience, 1962)

Strüder, L., Briel, U., Dennerl, K., et al. 2001, A&A, 365, L18

Tsujimoto, M., Koyama, K., Kobayashi, N., et al. 2004, PASJ, 56, 341

Vrba, F. J., Strom, S. E., & Strom, K. M. 1976, AJ, 81, 958

Woodward, P. & Colella, P. 1984, Journal of Computational Physics, 54, 115

Yamashita, T., Suzuki, H., Kaifu, N., et al. 1989, ApJ, 347, 894

Zel'Dovich, Y. B. & Raizer, Y. P. 1967, Physics of shock waves and high-temperature hydrodynamic phenomena (New York: Academic Press, 1966/1967, edited by Hayes, W.D.; Probstein, Ronald F.)